PhD Thesis 2022

THERMORESPONSIVE NANOSYSTEMS BASED ON GOLD NANOPARTICLES

By

Joscha Kruse

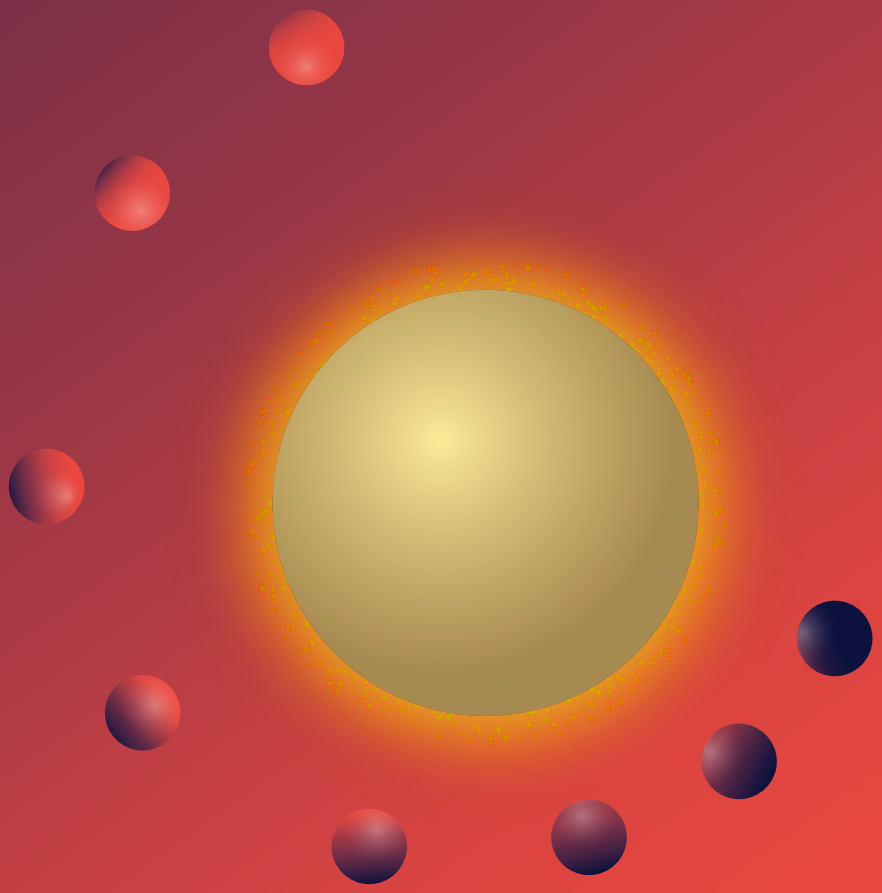

eman ta zabal zazu

Universidad del País Vasco

Euskal Herriko Unibertsitatea

PhD Thesis

Thermoresponsive Nanosystems based on Gold Nanoparticles

written by Joscha Kruse

Thesis Supervisor: Marek Grzelczak

Co-Supervisor: Andrey Chuvilin

June 6, 2022

Abstract

Nanoscience and -technology have attracted immense attention over the last two decades and tremendous progress has been made to synthesise and characterise new materials. For example, miniaturisation has been a key component to exponentiate the computing capacity of modern electronic devices, but deviation from Moore's Law is already taking place and we are reaching a limit caused by the size of atoms themselves.
To develop the field of nanotechnology, one must move further than static structures and take advantage of the possibility of reorganisation at the nanoscale, thus creating dynamic materials. This will have useful application for smart materials, that can autonomously adapt to changing environments, without the need of energy consumption. Furthermore, through actively manipulating nanoscale order different (macroscopic) properties (electrical, optical, mechanical). Additionally, miniaturisation limits can be overcome, because several functionalities can be retrieved within the same space by simply reorganising the building blocks. Through different stimuli, different nanocompartments could communicate with each other and fulfill different tasks, which will multiply the functionality and ultimately mimic life itself.

The field is still in its infancy, but nanoparticles - and in particular plasmonic nanoparticles - are an excellent class of material to develop such dynamic systems. Their outstanding and easily tuneable optical properties, as well as the infinite possibilities of surface modification allow to exploit their light matter interaction for many applications as drug delivery, (bio)sensors, soft robotics and many more. In literature, different stimuli are available to manipulate the reversible assembly of gold nanoparticles, but the chemical diversity of functional surfaces is still scarce. Furthermore, usually a poor picture of their dynamic properties of these materials is presented, because real-time analysis is rarely not considered.

Thus, this thesis aims to develop new thermoresponsive materials based on gold nanoparticles and to study their dynamic self-assembly using real-time analysis.
First, a methodology was developed mainly based on simple to use and non-invasive UV-Vis-NIR spectroscopy, to study thermoresponsive self-assembly of gold nanoparticles functionalized with Bis(p-sulfonatophenyl)phenylphosphine dipotassium salt (AuNPs@BSPP). AuNPs clustered at low temperatures, and could be reversibly redispersed by rising the temperature. Their thermoresponsive properties could be easily adjusted by adapting the ionic strength of their solution. Studying their reversible self-assembly revealed differences between assembly and disassembly pathway, which resulted in hysteresis during thermal cycling. The hysteresis could be

further qualitatively assessed into kinetic- and thermodynamic hysteresis. The former is caused by a lag of the sample response with respect to the stimulus and the latter is an intrinsic difference between assembly states at the same temperature and dependent on samples history but not on the rate of temperature change. Further hysteresis could be altered by increasing the size of gold nanoparticles or by introducing a cationic surfactant (cetyltrimethylammonium bromide, CTAB) as co-ligand of BSPP.

The fact that AuNPs@BSPP were thermoresponsive in the presence of surfactant, opened door to synthesized anisotropic thermoresponsive nanoparticles, such as gold nanorods (AuNRs). Thus, a two-step protocol was developed for robust surface functionalization of AuNRs with a mixture of BSPP and CTAB. The advantage of using BSPP molecules as surface ligands is their small size as compared to the conical thermoresponsive polymers, maximizing plasmon coupling, so that the optical properties of gold nanorods could be fully exploited. The extent of thermal hysteresis of this system was tuned by tailoring the composition of the mixture (concentration of reagents and ionic strength). Furthermore, the generality of the developed method was proven by functionalizing AuNRs of various aspect ratios and it was found that especially the chemical surface composition governs thermoresponsive properties. Last, mechanistic insights were provided that explain the interplay of both surface ligands.

Gold nanorods have the advantage over spherical particles, that their absorption cross sections are significantly larger, which makes them ideal candidate to exploit photo-thermal effect and introduce light as new stimulus to control their reversible clustering. A modular experimental setup was developed, that allowed to measure optical properties and temperature simultaneously under light irradiation. Through light to heat conversion, it was shown that AuNRs could be readily redispersed with light and furthermore, it was evidenced, that AuNRs@BSPP are possible candidates for nano-thermometry. Then, through rational designing the optical properties of AuNRs, the demonstration of self-oscillation concept was pursued. That is, AuNRs@BSPP underwent autonomously clustering/redispersion cycles under uninterrupted light illumination. The frequency of oscillation could be tuned with the light intensity or by aspect ratio of AuNRs and it could be demonstrated that thermodynamic hysteresis is a necessity for that type of oscillation to occur.

In the last chapter, thermal clustering of gold nanoparticles was controlled by yet another stimulus - exothermic chemical reaction. Coupling thermoresponsive colloidal system with a chemothermal chemical reaction is a non-trivial, and in fact

unaddressed, because a typical colloidal system is prone to rapid irreversible aggregation when faced with a complex chemical mixture. For that purpose copper catalyzed azide alkyne cycloaddition was used as an exothermic chemical reaction gold nanoparticles coated with DNA (AuDNA) were chosen as thermoresponsive system. It could be shown that AuDNA could be transiently dispersed, until the fuel was depleted. The extent of population and duration of the high energy state (dispersed AuDNA) could be controlled with the amount of fuel added and the functionality of thermoresponsive AuDNA and chemical fuel was ensured by controlling the order of reagent addition.

The present thesis offers a new class of thermoresponsive nanomaterials and new analytical tools to study their dynamic properties. In a broader context the developed methods can also be applied to other stimuli responsive optically active materials. Furthermore through the development of a functionalization protocol for gold nanorods, other anisotropic shapes can be assessed which further increases the diversity of optical properties. The demonstration of light-driven self-oscillation is a promising strategy to create heat engines that can do mechanical work at the nanoscale.

Resumen

En las dos últimas décadas, la nanociencia y la nanotecnología han atraído una inmensa atención debido a los enormes avances logrados en la síntesis y caracterización de nuevos materiales. La miniaturización, por ejemplo, ha sido un componente clave para aumentar exponencialmente la capacidad de cálculo de los dispositivos electrónicos modernos. No obstante, se está produciendo una desviación de la Ley de Moore llegando a un límite provocado por el propio tamaño de los átomos.
El desarrollo del campo de la nanotecnología exige avanzar más allá de las estructuras estáticas y aprovechar la capacidad de reorganización en la nanoescala, creando así materiales dinámicos. Esto tendrá una aplicación útil en materiales inteligentes, ya que podrán adaptarse de forma autónoma a entornos cambiantes, sin necesidad de consumir energía. Por un lado, a través de la manipulación activa del orden en la nanoescala se pueden obtener diferentes propiedades (eléctricas, ópticas, mecánicas) a escala macroscópica. Asimismo, los límites de la miniaturización son superables, ya que se pueden lograr varias funcionalidades dentro del mismo espacio simplemente mediante la reorganización de los bloques de construcción. Mediante diversos estímulos, diferentes nanocompartimentos podrían comunicarse entre sí y desempeñar distintas tareas, multiplicando la funcionalidad y, en última instancia, imitando la vida misma.

Pese a tratarse de un campo incipiente, las nanopartículas -y, en particular, las nanopartículas plasmónicas- constituyen una clase de materiales idóneos para el desarrollo de este tipo de sistemas dinámicos. Sus excelentes y fácilmente configurables propiedades ópticas, así como las infinitas posibilidades de modificación de su superficie, permiten explotar su interacción con la materia luminosa en múltiples aplicaciones como la liberación de fármacos, los (bio)sensores, y la robótica blanda entre otras. Existen en la literatura diferentes estímulos para manipular el ensamblaje reversible de las nanopartículas de oro, sin embargo, la diversidad química de las superficies funcionales es todavía escasa. Además, habitualmente se presenta una descripción pobre de las propiedades dinámicas de estos materiales, ya que rara vez se considera el análisis en tiempo real.

Por ello, esta tesis tiene como objetivo el desarrollo de nuevos materiales termoresponsivos basados en nanopartículas de oro y el correspondiente estudio de su autoensamblaje dinámico mediante el análisis en tiempo real. En primer lugar, se describe el desarrollo una metodología basada principalmente en la espectroscopia UV-Vis-NIR, sencilla y no invasiva, para estudiar el autoensamblaje termoresponsivo de las nanopartículas de oro funcionalizadas con Bis(p-sulfonatofenil) fenilfos-

fina dihidrato de sal dipotásica (AuNPs@BSPP). Las AuNPs se agrupan a bajas temperaturas y pueden redispersarse de forma reversible al aumentar la temperatura. Además, sus propiedades termoresponsivas se ajustan fácilmente adaptando la fuerza iónica de su solución. El estudio de su autoensamblaje reversible reveló diferencias entre la vía de ensamblaje y la de desensamblaje, dando lugar a la histéresis durante el ciclo térmico. La histéresis pudo evaluarse cualitativamente en histéresis cinética y termodinámica. La primera está causada por un retraso en la respuesta de la muestra con respecto al estímulo mientras que la segunda, es una diferencia intrínseca entre los estados de ensamblaje a la misma temperatura que depende de la historia de las muestras, pero no de la velocidad de cambio de temperatura. Además, se demostró que la histéresis puede alterarse aumentando el tamaño de las nanopartículas de oro o introduciendo un tensioactivo catiónico (bromuro de cetiltrimetilamonio, CTAB) como co-ligando del BSPP.

El hecho de que las AuNPs@BSPP fueran termoresponsivas en presencia de surfactantes, permitió el posterior desarrollo nanopartículas termoresponsivas anisotrópicas, como los nanorods de oro (AuNRs). Así, se estableció un protocolo de dos pasos para la funcionalización superficial robusta de AuNRs con una mezcla de BSPP y CTAB. El uso de moléculas BSPP como ligandos superficiales ofrece la ventaja de su pequeño tamaño en comparación con los polímeros termoresponsivos convencionales, maximizando el acoplamiento plasmónico. Como resultado, se pudieron aprovechar al máximo las propiedades ópticas de los nanorods de oro. El alcance de la histéresis térmica de este sistema se ajustó adaptando la composición de la mezcla (concentración de reactivos y fuerza iónica). Asimismo, se demostró la generalidad del método desarrollado mediante la funcionalización de AuNRs diversas relaciones de tamaño y se descubrió que, especialmente, la composición química de la superficie gobierna las propiedades termoresponsivas. Por último, se proporcionaron conocimientos mecanísticos que explican la interacción de ambos ligandos superficiales.

Los nanorods de oro presentan una ventaja respecto a las partículas esféricas, y es que sus secciones transversales de absorción son significativamente mayores, lo que los convierte en candidatos ideales para explotar el efecto fototérmico e introducir la luz como nuevo estímulo para controlar su agrupación reversible. Con este fin, se desarrolló un montaje experimental modular que permitió medir las propiedades ópticas y la temperatura simultáneamente bajo irradiación de luz. Mediante la conversión de luz en calor, se demostró que los AuNRs podían redispersarse fácilmente con la luz y, además, se reveló que los AuNRs@BSPP son posibles candidatos para la nano-termometría. Posteriormente, a través del diseño racional de las propiedades

ópticas de los AuNRs, se procedió a la demostración del concepto de auto-oscilación. Es decir, los AuNRs@BSPP experimentaron de forma autónoma ciclos de agrupación/redispersión bajo una iluminación de luz ininterrumpida. La frecuencia de oscilación se ajusto con la intensidad de la luz o por la relación de aspecto de los AuNRs y se demostró que la histéresis termodinámica es una condición indispensable para que se produzca este tipo de oscilaciones.

En el último capítulo, se seleccionó otro estímulo para controlar la agrupación térmica de las nanopartículas de oro: la reacción química exotérmica. El acoplamiento de un sistema coloidal termoresponsivo con una reacción química exotérmica no es trivial, y de hecho no se ha tratado previamente, debido a que un sistema coloidal típico es propenso a una rápida agregación irreversible cuando se enfrenta a una mezcla química compleja. Con este fin, se utilizó la reacción química exotérmica de cicloadición de azida catalizada por cobre y se seleccionaron nanopartículas de oro recubiertas de ADN (AuDNA) como sistema termoresponsivo. Se demostró que el AuDNA podía dispersarse transitoriamente, hasta que se agotara el combustible. El grado de población y la duración del estado de alta energía (AuDNA disperso) se controlaron con la cantidad de combustible añadido y la funcionalidad del AuDNA termoresponsivo y del combustible químico se garantizó controlando el orden de adición del reactivo.

Así, la presente tesis ofrece una nueva clase de nanomateriales termoresponsivos y novedosas herramientas analíticas para el estudio de sus propiedades dinámicas. En un contexto más amplio, los métodos desarrollados en esta tesis pueden emplearse en otros materiales ópticamente activos que responden a estímulos. Además, gracias al desarrollo de un protocolo de funcionalización de los nanorods de oro, se pueden evaluar otras formas anisotrópicas que aumentan aún más la diversidad de sus propiedades ópticas. La demostración de la auto-oscilación impulsada por la luz es una estrategia prometedora para la creación de motores térmicos que puedan realizar trabajo mecánico en la nanoescala.

Publications

Publications in preparation

- **Joscha Kruse**, Marek Grzelczak, *"Themoresponsive Gold Nanorods"*
- **Joscha Kruse**, Stefan Merkens, Andrey Chuvilin, Marek Grzelczak, *"Making sense of fourth dimension in the dynamic self-assembly of nanoparticles"*

Publications under review

- Stefan Merkens, Giuseppe de Salvo, **Joscha Kruse**, Evgenii Modin, Christopher Tollan, Marek Grzelczak, Andrey Chuvilin, *"Quantification of reagent mixing in liquid flow cells for Liquid Phase-TEM"*, Ultramicroscopy, 2022
- Stefano Antonio Mezzasalma, **Joscha Kruse**, Amaia Iturrospe Ibarra, Arantxa Arbe, Marek Grzelczak *"Thermal Hysteresis in Reversible Clustering of Gold Nanoparticles. Towards Nanocolloidal Heat Engines"*, Journal of Colloid And Interface Science, 2022
- **Joscha Kruse**, Maria Sanroman-Iglesias, Aimar Marauri, Ivan Rivillaa, Marek Grzelczak *"Coupling reversible clustering of gold nanoparticles with chemothermal reaction"*, 2022

Published articles

- **Joscha Kruse**, Stefan Merkens, Andrey Chuvilin, Marek Grzelczak, *"Kinetic and Thermodynamic Hysteresis in Clustering of Gold Nanoparticles: Implications for Nanotransducers and Information Storage in Dynamic Systems"*, ACS Applied Nano Materials 3 (9), 9520-9527, 2020
- M Ali Aboudzadeh, **Joscha Kruse**, Maria Sanromán Iglesias, Daniele Cangialosi, Angel Alegria, Marek Grzelczak, Fabienne Barroso-Bujans, *"Gold nanoparticles endowed with low-temperature colloidal stability by cyclic polyethylene glycol in ethanol"*, Soft Matter 17 (33), 7792-7801, 2021
- Ana Sánchez-Iglesias, **Joscha Kruse**, Andrey Chuvilin, Marek Grzelczak, *"Coupling plasmonic catalysis and nanocrystal growth through cyclic regeneration of NADH"*, Nanoscale 13 (36), 15188-15192, 2021
- Andrea Rogolino, Nathalie Claes, Judit Cizaurre, Aimar Marauri, Alba Jumbo-Nogales, Zuzanna Lawera, **Joscha Kruse**, María Sanromán-Iglesias, Ibai Zarketa, Unai Calvo, Elisa Jimenez-Izal, Yury P Rakovich, Sara Bals, Jon

M Matxain, Marek Grzelczak, *"Metal–Polymer Heterojunction in Colloidal-Phase Plasmonic Catalysis"*, The journal of physical chemistry letters 13 (10), 2264-2272, 2022

Glossary

AA ascorbic acid.

AuDNA DNA coated gold nanoparticles.

AuNPs gold nanospheres.

AuNRs gold nanorods.

BSPP bis(p-sulfonatophenyl)phenylphosphine dihydrate dipotassium salt.

CTAB cethyl trimethyl ammonium bromide.

CTAC cethyl trimethyl ammonium chloride.

CuAAC Copper-catalysed azide-alkyne cycloadditions.

DLS Dynamic light scattering.

DLVO Derjaguin, Landau, Verwey, and Overbeek.

FFT fast-fourier transformation.

HEG hexa(ethylene glycol).

HQ hydroquinone.

LSPR Localized surface plasmon resonance.

MUDOL (1-mercaptoundec-11-yl)hexa(ethylene glycol).

PEG polyethylene glycol.

TEM Transmission electron microscopy.

VdW Van der Waals.

Contents

CHAPTER 1

Introduction

1.1 Objectives

Back in 1959, Richard Feynman delivered a seminal lecture titled "There is plenty of room at the bottom" where he conceptualized the enormous technological possibilities by controlling the properties of matter at nanoscale precision. Today, over half a century later his ideas remain relevant. Nanoscience and nanotechnology indeed impacted our wellbeing through new electronic devices with nanoscale compartments[1, 2], nanoscale drug delivery systems[3], bio-sensors[4] (e.g., antigenic test for CoVID-SARS-2) or novel therapeutic methods for cancer treatment[5], to just name few. Yet, nanoscience and nanotechnology provided no revolutionary breakthrough as compared to electricity or internet. This provocative statement has been raised by Grzybowski and Huck[6], who indicated the need for further development of nanoscience in the following passage:

> *"we argue that the time is ripe to look beyond individual nano-objects and their static assemblies, and instead focus on systems comprising different types of nanoparts interacting and/or communicating with one another to perform desired functions [..]. In thinking how this approach could be implemented to design useful nanosystems, our choice of applications and our nanoengineering should be inspired by living matter."*

Indeed, two billion years of evolution on earth resulted in sophisticated nano-machines operating under non-equilibrium conditions, that is, a constant energy flux from solar radiation. These nano-machines as a whole exhibit properties that apparently are exclusive to living matter, but in reality are common to any physical system if placed in right context, under energy flux[7]. Without any doubt, with the progress of experimental and analytic techniques the physics behind biology gain better understanding. And such an understanding facilitates the growth of research community devoted to study experimental chemical dynamic systems. In this line, material

scientists, who are specialized in the synthesis of nanoparticles and (supramolecular)chemistry, have now in hands a promising toolbox to develop dynamic materials with the control on spatiotemporal organization down to the nanoscale and thus extracting new functions.

The above-mentioned paper served, to some extent, as a motivation for the execution of the present thesis that seeks to design, optimize and study stimuli responsive nanosystem based on optically-active nanoparticles. Temperature was selected as a stimulus because it is a universal parameter that can be easily applied and modulated experimentally, and has direct connection to the thermodynamic analysis of given system. Yet, surprisingly temperature remains a poorly exploited stimulus in nanoparticles clustering. It was also hypothesized that the implementation of real-time analytics (spectroscopy and temperature) can resolve temporally how nanosystem under study responds to given stimulus. In fact, it will be shown that temporal and multiparameter monitoring can help in revealing intriguing signatures such as *hysteresis* in the temperature-driven clustering of isotropic (Chapter 2) and anisotropic (Chapter 3) nanoparticles or even *self-oscillations* when nanosystem by transducing light energy into heat can sustain its own colloidal (in)stability (Chapter 4). Also, focus was put on the *coupling of thermoresponsive dynamic nanosystem with chemical process generating heat* with the aim to demonstrate that temperature is a stimulus that can be modulated chemically (Chapter 5).

1.2 Why gold nanoparticles?

For the purpose of the present thesis, gold nanoparticles were selected as a central material. Gold nanoparticles have several advantages: they are chemically stable, relatively easy to synthesize and surface functionalize, they exhibit tunable optical properties sensitive to their shape, size and colloidal stability, and their aggregation dynamics are relatively slow (as compared to molecular systems) allowing for facile implementation of spectroscopy-based real-time analytics.

Gold is a metal that is characterized by a large number of free electrons, that are not associated with individual atomic cores. These electrons are also referred to as electron gas, since they can move freely through the material. Under electromagnetic radiation[8] the electron gas experiences collective oscillation giving rise to so-called *plasmon.*

Different types of plasmons exist such as the bulk, surface and localized surface plasmons[10]. As the name suggests, bulk plasmons occur in bulk materials and extend in all three dimensions. They appear at plasma frequency and their energy is defined as:

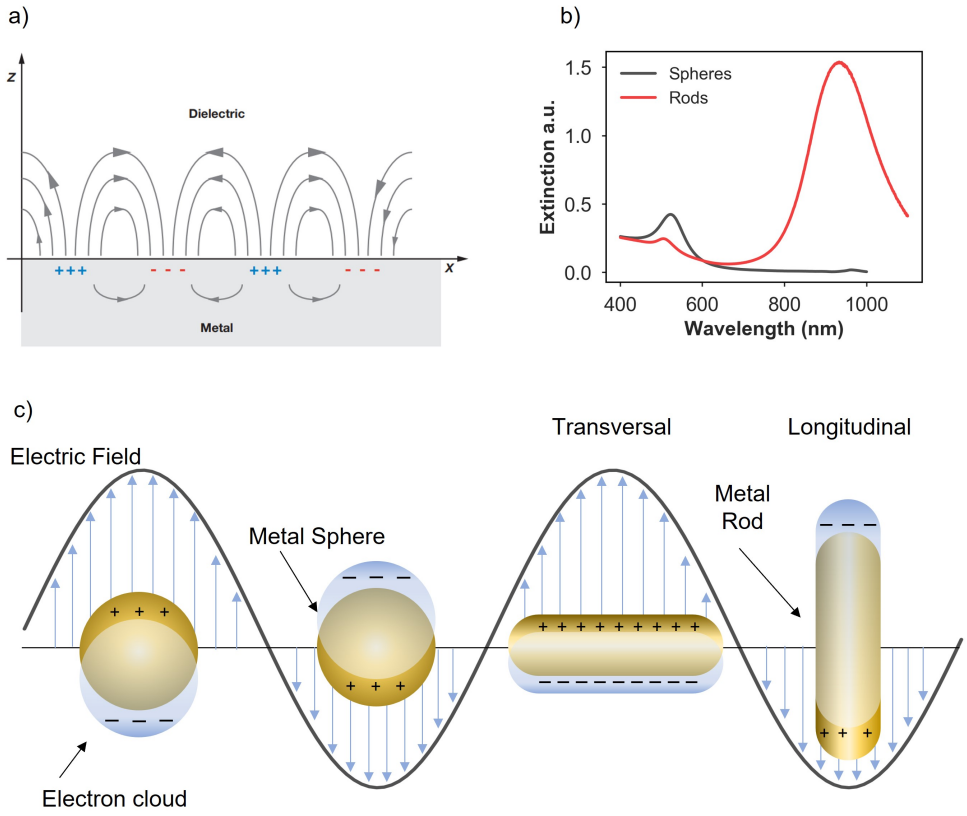

Figure 1.2.1: Surface Plasmons. a) Surface plasmon at the interface of a metal and an dielectric. Reprinted with permission from [9]. b) UV-Vis-NIR spectra of gold nano-spheres and -rods showing shape-optical properties relationships. c) Schematic representation of localized surface plasmons in spheres and rods induced by an electric field.

$$E_p = \hbar\sqrt{\frac{ne^2}{m\varepsilon_0}} \tag{1.1}$$

where ε_0 is the permittivity in vacuum, n is the electron density, e the electron charge and m the electron mass.

Surface plasmons are oscillatory waves that propagate at the interface of a metal and an dielectric. The incident electromagnetic waves induces a dipole through localized charge accumulation that further propagates over the surface.

$$\omega_{SPR} = \frac{\omega_P}{\sqrt{1+\varepsilon_u}} \tag{1.2}$$

For the material with the size smaller that the wavelength of incoming light, the surface plasmon becomes localized (Figure 1.2.1), resulting in a collective displacement of the electron gas within a nanocrystal. Through the charge separation, the positively-charged metal cores exhibit a restoring force, leading to an oscillatory movement of the electrons as depicted in Figure 1.2.1 c). When quasi-static regime is assumed and if the nanoparticles are significantly smaller than the excitation

wavelength ($r << \lambda$) the resonance frequency can be described as the following[11]:

$$\omega_{LSPR} = \sqrt{\frac{e^2}{m_e 4\pi\varepsilon_0 r_s^3}} \tag{1.3}$$

with ε_0 as the permittivity of vacuum, m_e the mass of an electron, e electron charge, and r_s the Wigner-Seitz radius which is defined as the radius of a sphere whose volume is equal to the volume per conduction electron in the bulk ($R = r_s N^{\frac{1}{3}}$). Localized surface plasmon resonance (LSPR) has two important characteristics, which are greatly enhanced electric fields near the nanoparticle surface and the large optical extinction as they are capable of capturing the surrounding light, behaving thus as nano-antenna.

For noble metals LSPR lay in the visible range resulting in a vibrant color, which can be explained by using Mie approximation to calculate the extinction cross section.

$$\sigma_{ext} \sim \frac{\varepsilon_2}{(\varepsilon_1 + 2\varepsilon_m)^2 + \varepsilon_2^2} \tag{1.4}$$

where ε_1 is the real part of the dielectric function of the metal, ε_2 is the imaginary part of the dielectric function and ε_m is the dielectric constant of the surrounding medium[11]. The real part ε_1 can be interpreted as a measure of the polarizibility at a given wavelength and ε_2 as the probability of photon absorption[12].

From Equation 1.4 follows, that extinction cross section σ_{ext} is the largest, when the denominator approaches 0. Thus, to excite plasmon resonance, ε_2 should be small and $\varepsilon_1 \sim -2\varepsilon_m$. These conditions are fulfilled for Ag, Au and Cu in the visible spectral range.

As stated in equation Equation 1.4, LSPR depends on the dielectric function of the metal and the dielectric environment. For gold nanospheres (AuNPs), LSPR is around 520 nm but its exact maximum depends also on particle size. For increasing AuNPs size the restoring force is weaker due to charge separation over larger distances which leads to an easier polarizability of the electron cloud. Therefore, LSPR red-shifts with increasing nanoparticle size. This can be applied for AuNPs up to 50 nm, because scattering is low. Damping and retardation effects with increasing particles diameter as well as the formation of multipole oscillation play an important role above that threshold.

The shape of nanoparticles has much stronger effect on the optical properties[13]. If the symmetry of gold nanoparticles is broken, as for anisotropic gold nanorods (AuNRs), two plasmon bands emerge, namely transversal and longitudinal which are the results of two limiting scenario of electron gas oscillation (Figure 1.2.1 b, c). In practice, a colloidal solution containing gold nanorods possesses both plasmon band since nanoparticles are randomly distributed and the incoming light is not

polarized. The position of the longitudinal plasmon band is sensitive to the aspect ratio, that is, the ratio of the length to the width of the nanoparticles. The larger is the aspect ratio, the more shifted is the plasmon band.

1.3 Plasmon in coupled nanoparticles

One of the most visual property of gold nanoparticles is the sensitivity of their optical properties to the inter-particle distance. When particles are in close contact to each other (< 10 nm), their induced electric field influence each other, so that all free electrons of the AuNPs cluster can oscillate collectively. This leads to change of optical properties and for AuNPs, this effect can be observed with the naked eye by a color change from red to blue. Over the last two decades, a number of computational methods have been developed to understand such behavior. As an example, Figure 1.3.1 a shows calculated extinction spectra of AuNPs with diameter of 20 nm and varying the surface-to-surface distance from 4 nm to 0 nm. Dispersed AuNPs show a single plasmon band (530 nm) that split in two bands with decreasing the distance between nanoparticles. Although the calculated spectrum in Figure 1.3.1 a) resemble the spectrum characteristic to nanorods (the presence of transverse and longitudinal bands), the origin of two bands is quite different. The band of higher energy is attributed to quadrupole plasmon excitation while the band of lower energy addressed to the red-shifted dipole plasmon resonance [14, 15]. Interestingly, since the plasmon coupling is highly sensitive to distance, it can be used to calculate the distance between particles with the relative shift of extinction wavelength:

$$\frac{\Delta_\lambda}{\lambda_0} \approx 0.18 \exp \frac{-(\frac{s}{D})}{0.23} \tag{1.5}$$

where $\frac{\Delta_\lambda}{\lambda_0}$ is the relative plasmon shift, s is the surface-to-surface distance, and D is the particle diameter[16]. This equation indicates that interaction between plasmons is maximized for large diameters at low distances. The effect of diameter at a fixed distance is demonstrated in Figure 1.3.1 b), where AuNPs diameter is decreased from 40 to 5 nm with a gap of 0.5 nm. First, one maximum that was observed for small diameters splits up into two with increasing diameter and the intensity especially of the second maximum largely increases and red-shifts.

Note that for calculation of these spectra linear cluster with fixed angle of 180 ° were assumed. For real world samples, one must consider the angle dependency, which influences the polarizibility of neighboring particles. Also, the aggregate size influences the extent of coupling, where at larger aggregate sizes the extinction and red-shift of second peak increase. As of note, the understanding of the optical properties for different mutual arrangements of the nanoparticles opens up a sub-discipline in plas-

monics: the so called plasmonic polymer, where nanoparticle monomers can form oligomers or polymers with new optical properties.

The plasmon coupling can be explained intuitively through plasmon hybridization model[17–19] that has its roots in Molecular Orbital theory (Figure 1.3.2 a). For example, for dimers of spherical nanoparticles two bright plasmonic modes, σ and π^*, emerge at the energy lower and higher than that of individual nanoparticles. The presence of dark modes (marked with a red "X") is also possible but they do not couple with electromagnetic waves. The hybridization model explains the red-shift of AuNPs cluster observed in their extinction spectra. Due to the lower energy of the coupled plasmon mode, the maximum of extinction spectra is shifted towards longer wavelengths (Figure 1.3.2 c). Although blue-shift is theoretically possible due to the σ^* mode, its contribution to extinction is negligible.

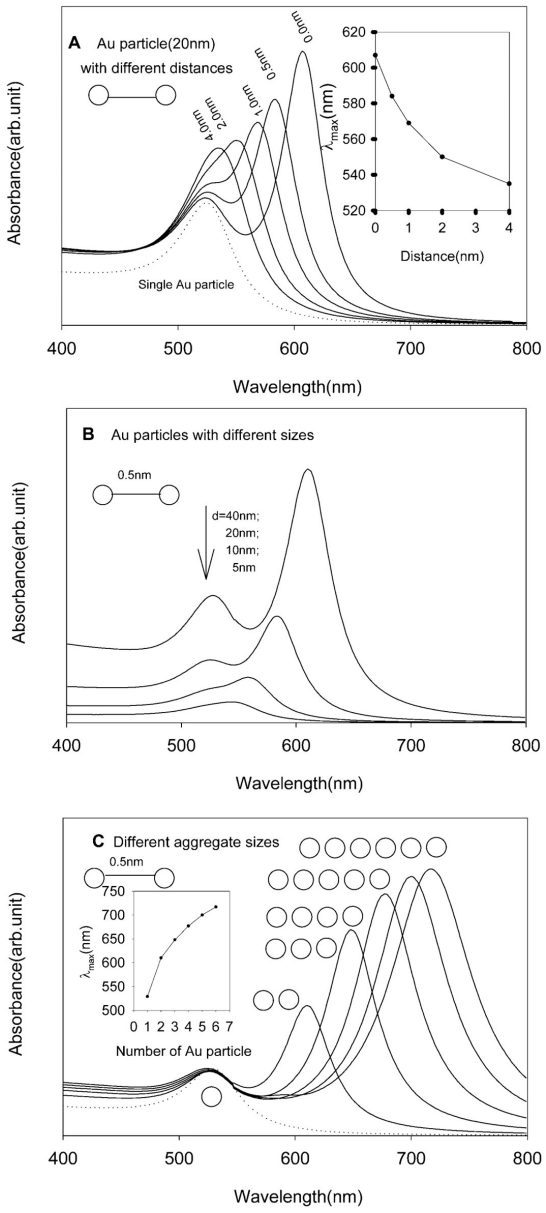

Figure 1.3.1: The coupling of localized surface plasmon resonance depends on their distance a), size b) and the aggregate size c). Adapted from reference [15].

The plasmon hybridization for gold nanorods is even more interesting. Figure 1.3.2 b show 8 different modes of plasmon coupling. The most frequent cases are tip-to-tip and side-to-side configurations where the energetic levels lay largely above or below the energy level of individual (dispersed) AuNRs (Figure 1.3.2 b). Importantly, the plasmon hybridization model for gold nanorods has been described in details by measuring optical properties of individual dimers using Dark Field Microscopy.[20] In solution, where the number of particles can reach up to 10^8 monomers, the clustering process can results in the formation of many possible configurations, leading to broadening and damping of plasmon band. However, the tendency of shift of plasmon band during the clustering can serve as a qualitative indicator for the directionality of the inter-particle interactions. As

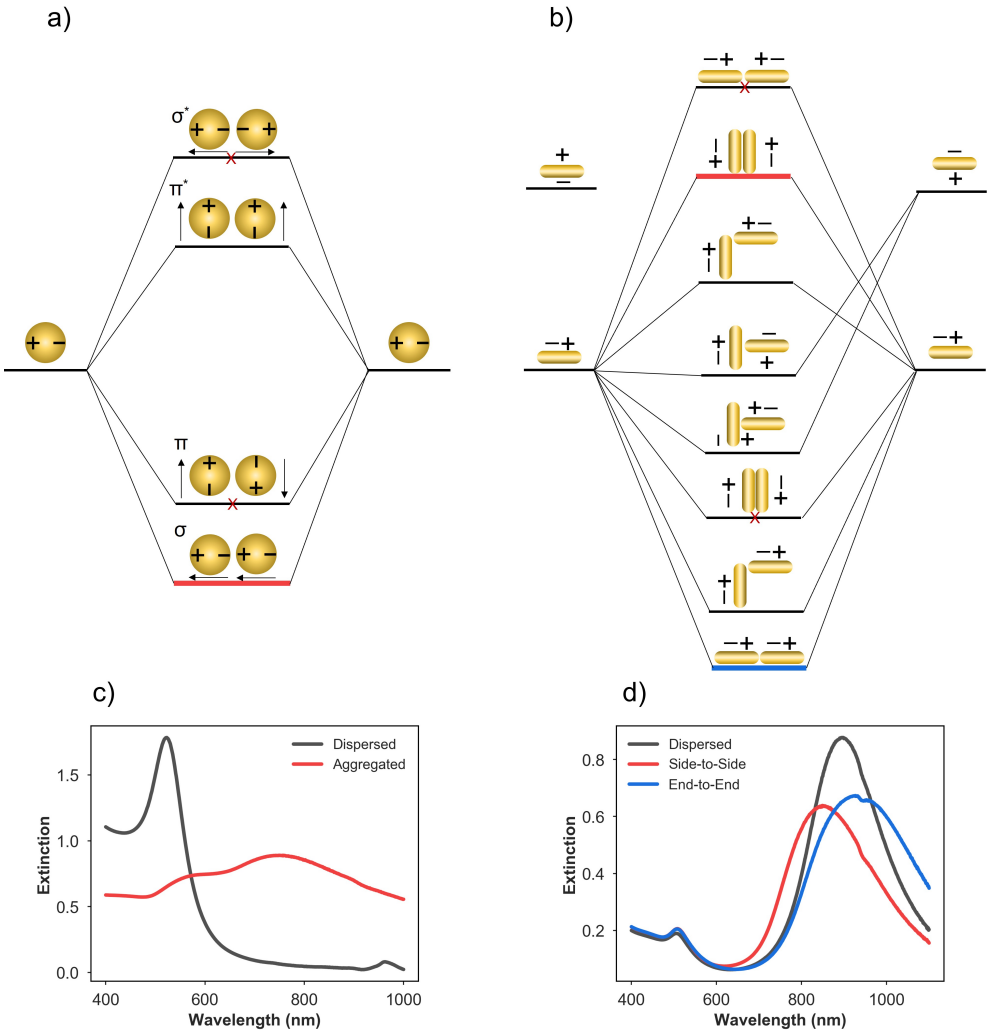

Figure 1.3.2: Hybridization scheme of plasmon coupling for AuNPs a) and AuNRs b). Dark plasmon modes are depicted with a red "X". Transversal coupling modes are omitted, since they are analogical to longitudinal coupling modes. Figures inspired from references [17, 20, 21].

a real-world example, consider black spectrum in Figure 1.3.2 d) that can either red- or blue-shift, suggesting that there is higher probability of finding particles in tip-to-tip or side-to-side configuration.

1.4 Thermoplasmonics - converting light energy into heat

Owing to a large absorption cross section and (usually) non-radiative relaxation of excited electrons, plasmonic nanomaterials are known to have a strong photothermal effect. The decay of localized surface plasmon resonance results in the conversion of light energy into heat through joule effect, that is, oscillating electron gas loses energy on the expense of immobile ions in the crystal lattice. If we consider a single

laser pulse interacting with a nanoparticle, the heat released to the environment can be divided into three steps that operate at different time scales. First, the energy of the light pulse is absorbed by the free electrons of given nanoparticle and the electrons equilibrate to a Fermi-Dirac distribution over a timescale of 100 ps, while the ions of the lattice remain at ambient temperature[22]. The produced hot carriers (electrons and holes) relaxe through electron-phonon interaction, which takes approximately 1.7 ps. This timescale is independent of the nanoparticle size, given that electrons are delocalized (d $\gtrsim$ 5 nm)[23]. At this point the nanoparticle has a uniform elevated temperature, while the environment remains at ambient temperature. Heat exchange with the environment takes about 1 ps to 1 ns, depending on the nanoparticles size and thermal conductivity of the surrounding medium[24].

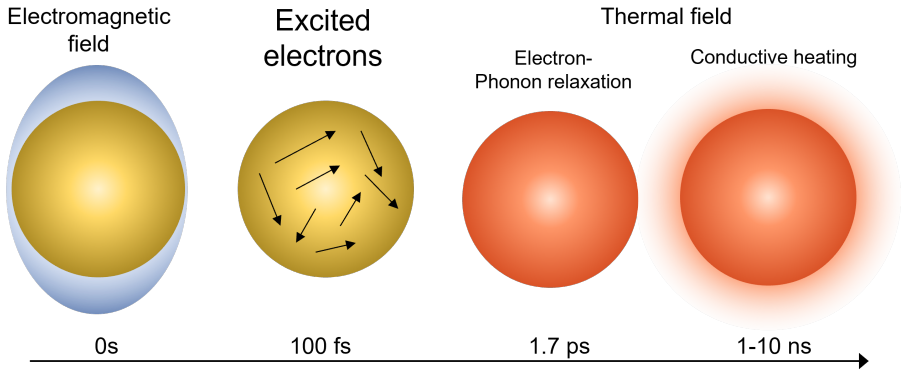

Figure 1.4.1: Schematic representation of the heat production close to particles surface through the decay of localized plasmon surface resonance. Figure inspired from reference [25].

For a gold nanoparticle in a medium (water) under illumination, the temperature increase of the nanoparticle is given by:

$$\delta T = \frac{\sigma_{abs} I}{4\pi\kappa_s \beta r} \tag{1.6}$$

where σ_{abs} is absorption cross section, I is the light irradiance (power per unit area), κ_s the thermal conductivity, r the radius of nanoparticle, and $\beta >$ 1a correction factor taking into account the shape of the nanoparticle ($\beta = 1$ for a sphere). The dielectric medium (e.g., water, air, vacuum) plays also an important role because of their difference in heat capacity and thermal conductivity.

The heat generated within plasmonic nanoparticles can be exchanged with the environment via conduction, convection or thermal radiation, being the former the important way of heat transport. The lag time for plasmonic heating through conduction is relatively short. To give an example, in water it takes $\sim$ 20 ns to reach similar temperature 100 nm away from the heated particle.

An important parameter ruling the way the heat propagate out of the nanoparticles

surface is the timescale of irradiation. Under continues wave irradiation, the local temperature close to the nanoparticle decays as 1/r (with r being distance from nanoparticles), while for femtosecond pulsed laser the temperature decays as $1/r^3$ (Figure 1.4.2). The way the heat propagate out of nanoparticle surface is relevant especially if one need to take advantage of collective heating by many particles.

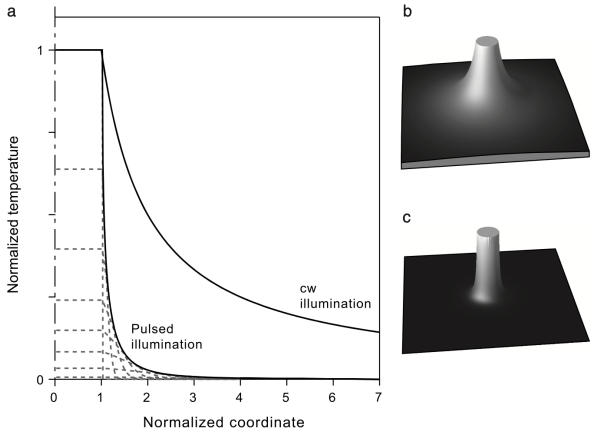

Figure 1.4.2: (a) The temperature profiles at different times around a sphere (20 nm) heated by a pulse (fs) and continuous wave illumination. (b-c) Three-dimensional plot of the steady state temperature profile under continuous wave (b) and pulsed (c) illumination. Figure adapted from reference [26].

It has been shown, that when the distance between nanoparticles decreases the collective thermal effects can become dominant leading to an overall increase and homogenization of temperature distribution[27–29]. From the optics perspective, the collective heating can sound counter intuitive since nanoparticles separated by a few diameters are usually optically decoupled. But from thermodynamics point of view it does matters, especially for larger number of nanoparticles. The resulting temperature increase comes from two contributions: heat generation by individual nanoparticle and the heat generated by the other N-1 nanoparticles under illumination in the sample. Therefore, if considering N identical spherical nanoparticles of radius r (labeled from 1 to N) and located at positions, a, one can estimate the temperature increase experienced by each nanoparticle:

$$\delta T_j = \frac{\sigma_{abs,j} I}{4\pi\kappa_s r} + \sum_{k=1}^{N} \frac{\sigma_{abs} I}{4\pi\kappa_s |a_j - a_k|} \tag{1.7}$$

If the number of particles is large in the system, the temperature can increase considerably. In practice, however, the estimation of collective temperature in a colloidal solution of nanoparticles by using Figure 1.4.3 can be a tedious task.

To simplify it, Baffou has proposed a dimensionless coefficient, ζ_m, to estimate the balance of the local and collective heat contributions:

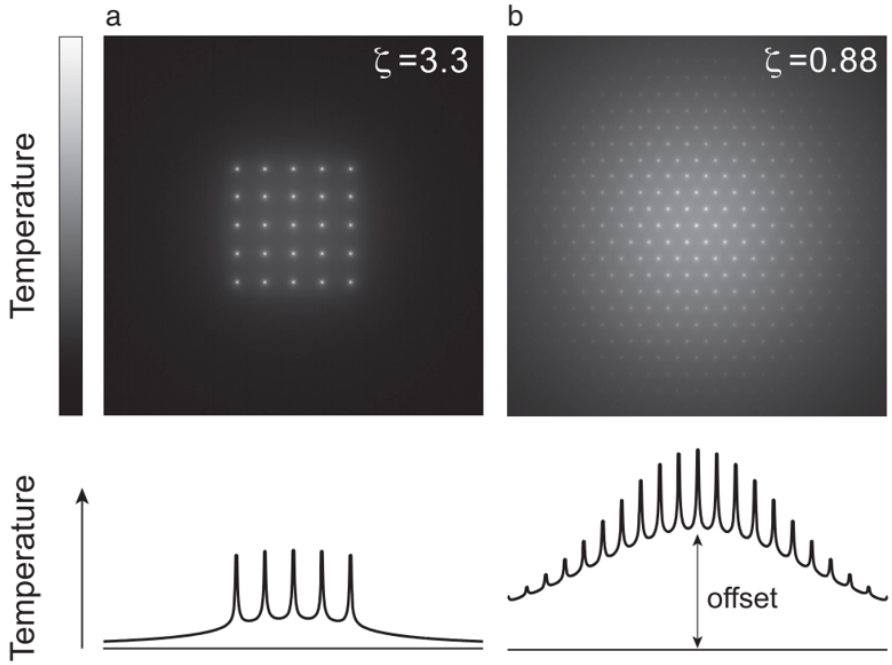

Figure 1.4.3: Temperature profiles of AuNPs under irradiation for a) large inter-particle distances leading to thermal hot spots and b) short inter-particle distances leading to larger temperature increase and homogenization. The offset indicates how the collective heating can dominate temperature profile of the sample. Adapted from reference [30].

$$\zeta_m = \frac{p}{rN^{\frac{(m-1)}{m}}} \tag{1.8}$$

where p is the average inter-particle distance, r the nanoparticle radius, N the number of nanoparticles and m the dimensionality of the observed system (m = 3 for nanoparticles in solution). If $\zeta_m >> 1$, nanoparticle do not influence each other and they can be considered as local thermal hot spots(Figure 1.4.3 a). If $\zeta_m \geq 1$, the overall temperature increases (Figure 1.4.3 b) and for $\zeta_m << 1$ a smooth temperature distribution is observed and thermal hot spots are not present anymore. Importantly, thermal coupling (collective heating) operates at the dimensions much larger than plasmon coupling. For example, collective heating can be observed for spherical nanoparticles of 5 nm in diameter and with µm distances[31].

1.5 Chemical synthesis of gold nanoparticles

As mentioned above, in the present thesis the temperature-driven reversible clustering of nanoparticles will be studied using gold nanoparticles. Two different shapes were selected for this purpose, namely spherical and rod-like. Although the synthesis of these nanoparticles is not central to the aim of this work, it is convenient to discuss briefly the main chemical mechanisms behind the growth of these nanoparticles.

Wet chemical synthesis of gold nanoparticles is usually classified according to two mechanisms: nucleation/growth, and autocatalytic reduction, so-called seeded-growth (Figure 1.5.1 b).

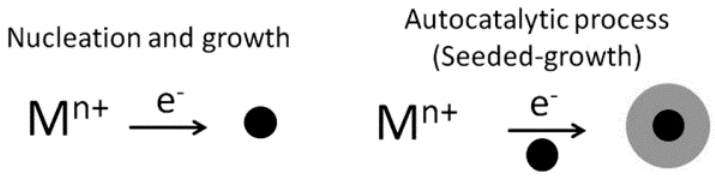

Figure 1.5.1: Two main mechanisms for the synthesis of gold nanoparticles. In the nucleation and growth mechanism, strong reducing agent reduces metal ions followed by growth into nanoparticles. In the seeded-growth process, autocatalytic reduction of metal ions takes place exclusively on the the surface of preformed seeds to produce particles of the desired shape and size. Reproduced from [32]

In the first approach, strong reducing agent reduces metal salt to produce dispersed nanoparticles that host organic molecules on their surface, preventing aggregation. The size of nanoparticles can be controlled by tuning the molar ratio between the stabilizing/reducing agent and the metal precursor. At nucleation stage, available precursor ions undergo fast reduction. To obtain monodispersed nanoparticles, one need to increase the nucleation rate so that after the first nucleation burst no additional nuclei are formed. The growth stage starts after reaching a saturation point at which individual precursors only deposit on existing particles. This approach permits the synthesis of large amounts of particles without loss of quality because with increasing the concentration of the metal precursor the saturation point is achieved faster. The fast kinetics of the process however leads to the particles with isotropic shapes.

In the seeded-growth model, the nucleation and growth stages are separated in time. The seeds are usually obtained through the nucleation and growth process and later are used in the autocatalytic overgrowth to obtain desired nanoparticles The autocatalytic nature of the process allows to control the number of final nanoparticles that depends on the amount of added seeds. Also one can predict the size of the final nanoparticles (spherical) through the following equation[33]:

$$D_f = D_n(\frac{Au_n + Au_g}{Au_n})^{1/3} \tag{1.9}$$

where D_f is the final diameter, D_n is the diameter of the seed, Au_n the amount of metallic gold in the seed particles and Au_g is the amount of gold precursor in the growth medium. The reason why seeded-growth method gained much attention is slow reduction kinetic that allows for inhibition of given crystal facets during growth and thus symmetry breaking. Thus the anisotropic gold nanoparticles (cubes, decahedra, octahedra, dodecahedra, triangles, rods, bipyramids, wires), and

with the most interesting optical properties, are usually synthesized through the seeded growth methods.

1.5.1 Synthesis of spherical gold nanoparticles

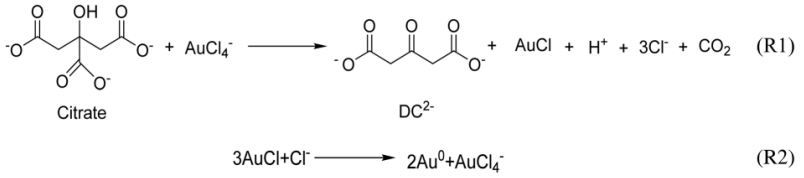

Figure 1.5.2: Accepted mechanism for Turkevich synthesis AuNPs stabilized with citrate.

The most common approach for synthesis of spherical nanoparticles developed in the 1950s by Turkevich et al.[34] using sodium citrate, which acts a mild reducing agent and stabilizing surface ligand. The popularity of this synthetic route is due facile replacement of the native weakly bound citrate molecules on the surface of AuNPs with a functional ligand. Over the decades, to improve the the original synthesis protocol some variations were proposed such as the order of reagent addition[35] or the use of buffered system to control the pH during nucleation[36] The accepted reaction mechanism consists of two consecutive reaction steps[37]. In the first redox reaction Au(III) ions are reduced to Au(I), while citrate is oxidized to acetone dicarboxylate. The Au(I) ions accumulate in polymolecular acetone dicarboxylate complexes, yielding high local Au(I) concentration. This allows in a consecutive step for disproportionation of Au(I) into Au(III) and metallic Au(0), ultimately leading to nucleation and growth of AuNPs. In order to obtain monodisperse AuNPs one must control the nucleation and growth step. This can be achieved by increasing the reactivity of Au precursors, by adjusting pH or through increasing the concentration of acetonedicarboxylate species by preboiling Na-Citrate for 15 minutes.[35, 36, 38, 39]

The classical Turkevich method usually yields AuNPs of 13 nm in diameter. To obtain larger nanoparticles a seeded-growth approach can be implemented as proposed by Bastus et al. [40]. In this scenario AuNPs are synthesized and grown in consecutive citrate and Au(III)precursors addition steps. Still, this method requires to avoid secondary nucleation during the growth steps, which is achieved through lowering temperature or concentration of metal precursor.

1.5.2 Synthesis of gold nanorods

A flagship example of anisotropic nanoparticles are without any about gold nanorods that can be obtained by seeded-growth method through well-established synthesis

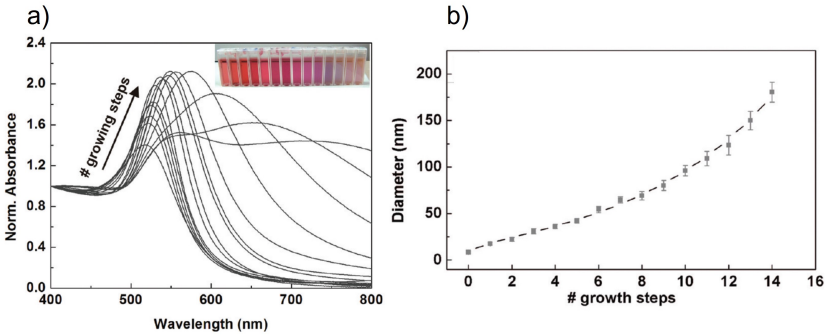

Figure 1.5.3: Seeded Growth of AuNPs. With every growth step LSPR red-shifts and diameter of gold nanoparticles increases. Figure adapted from reference [40].

routes.

The most common approach to produce single crystalline AuNRs is using cethyl trimethyl ammonium bromide (CTAB) assisted seed mediated growth in the presence of silver nitrate, which was first demonstrated by Jana et al.[41] and further developed by Nikoobakht et al. in the early 2000s[42]. The nucleation and growth of AuNR is separated in time and space and fine control over the aspect ratio and thus the optical properties is achieved over adjusting the reagent concentrations during the growth step such as silver ions or concentration of gold seeds. In typical synthesis, small gold seeds are synthesized with the aid of a strong reducing agent (e.g., $NaBH_4$), which results in gold nanoparticles with diameters around 2 nm.[42] Due to the small size of seeds, no surface plasmon is observed, thus their absorption spectra is characterized by a maximum in UV-range, which originates from inter-band transitions (Figure 1.5.4 a - black) [43].

Since the seeds act as catalyst, a mild reducing agent (e.g., ascorbic acid) is used during the growth, avoiding secondary nucleation. Time-resolved UV-Vis-NIR measurements of AuNRs growth in Figure 1.5.4 b) show, that aspect ratio is defined at an early growth stage and extinction increases over time. The inset depicts the temporal evolution of Au(0) in the solution and shows a sigmoidal curve, typical for autocatalytic growth.[44] While the exact mechanism is still debated it is generally agreed on, that silver ions and CTAB are key components to obtain AuNRs[45, 46]. Thus, during the early stage of the growth, the seeds gain the size ($\sim$ 6 nm) allowing the emergence of facets of unequal surface energies. The presence of silver ions and Br^- renders insoluble silver bromide that exhibit good affinity toward gold facets of higher surface energy, thus blocking it for further overgrowth[45, 47] Such a facet-dependent gold reduction rate causes symmetry breaking at the early stage of gold nanorods formation. Such a mechanism also explains why the aspect ratio of AuNRs can be tuned by the amount of Au^+ ions during growth step (Figure 1.5.4 c). The role of the CTAB is also important. At high concentration CTAB can form

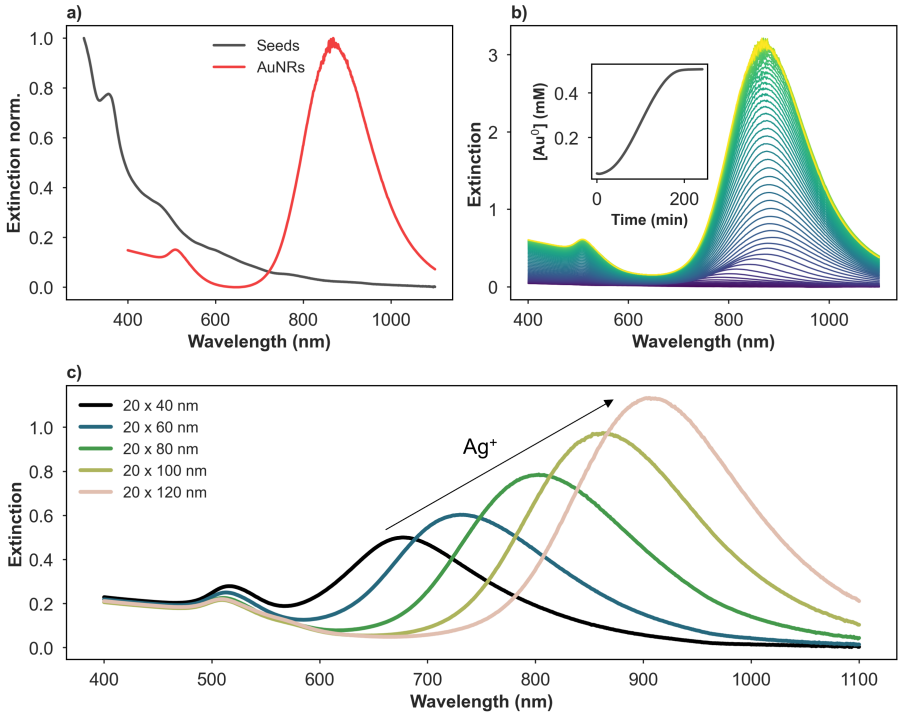

Figure 1.5.4: Synthesis of gold nanorods. a) UV-Vis-NIR spectra of gold seeds and as-prepared gold nanorods. b) Time-resolved optical characterization of gold nanorods growth solution, showing that at the early stage anisotropic nanoparticles emerge. c) The effect of silver ions on the dimensions of the final gold nanorods.

micelles and bilayers playing role of a capping agent[48]. Additionally CTA^+ can form a complex with Au(III) ions increasing its redox potential and thus further decreasing reduction rate.

To close, the need for use of surfactant molecules during the growth of gold nanorods often holds back their use in catalysis or nanomedicine where surface chemistry determine their utility. Thus one need to implement and optimize a meticulous process of ligand exchange to render desired properties. It is also the case in the forthcoming chapters where thermoresponsive properties of gold nanorods will determined by controlling their surface chemistry.

1.6 Stimuli-responsive nanosystems studied by real-time analytics: an overview

Since the present thesis deals with design and synthesis of thermoresponsive nanosystems studied via the use of real-time analytics it is convenient to contrast such a system with the existing works and available in literature.

Generally, under self-assembly one can understood the process in which a disordered building blocks (molecules, nanoparticles) organize into structure caused by local

interactions among the building blocks themselves[49]. Although the process of self-assembly can be found on all length scales from cosmos formation[50] down to arrangement of molecular structures [51] or proteins[52], it is a relevant aspect of nanoscience and nanotechnology because it offers tools for bottom up fabrication of macroscopic materials using nanoscale building blocks.

Th process of self-assembly is classified as static and dynamic. The static self-assembly is an irreversible process driven by entropy to produce superstructures residing at local or global equilibrium. A canonical example is the formation of superlattices of nanoparticles through solvent evaporation.[53–56] Dynamic self-assembly is reversible process where under the action of stimulus the building blocks form metastable structures. Once the stimulus is canceled, the system recovers its initial state. Theoretical description of dynamic self-assembly is a non-trivial task since such a system can traverse across different local minima upon the action of stimulus, where directionality of applied stimulus (forwards versus backwards) and rate of its application can impact structure and energetics of the assemblies. Again, the only feasible way to resolve such directionality is through real-time analytics that allows for tracking the change of the system in situ and, thus, to determine all possible states the system can occupy.

Over the last decades a broad variety of stimuli for dynamic self-assembly have been proposed. Typically one can classify the stimuli as internal (chemical) and external (physical).[57, 58] The chemical stimulus can be type of solvents, acid/base signals, metal ions, gases, biomacromolecules, and redox signals. The physical stimuli can be temperature, magnetic and electric fields, light or pressure. While physical stimuli are non-invasive and rather facile to regulate (e.g., light intensity or temperature), the chemical stimuli alter the chemical composition of the nanosystem and can be regulated through their concentration. Since chemical stimuli are difficult to cancel - once a chemical compound is added to the system it is difficult to remove it - their use in self-assembly is mostly motivated by the development of (bio)sensors. Physical stimuli are studied mostly in the context of development of switchable active materials with the aim to be implemented in devices (e.g., optoelectronics). Therefore the need for development of stimulus responsive nanosystems is rather obvious in the context of technological development, having a potential to impact many areas of our lives.

To obtain a truly stimuli responsive materials one needs to assure that the stimulus couples with given nanosystem. There are two strategies for such coupling. From one side, the stimulus can alter the properties of the metal core which in turn can induce structural changes in surface ligands or environment and thus leading to assembly. Such type of coupling is less studied and is mostly reserved to physical stimulus, for example, magnetic field can change magnetisation of magnetic nanoparticles,

facilitating clusters formation. From the other side, the coupling can be achieved by the action of the stimulus on surface ligands grafted on the surface. Such type of coupling is more common and can be applied to both physical and chemical stimuli. The following discussion limits to the literature examples on dynamic self-assembly studied by real-time analytics. The discussion is structured by the type of stimulus used.

1.6.1 Temperature

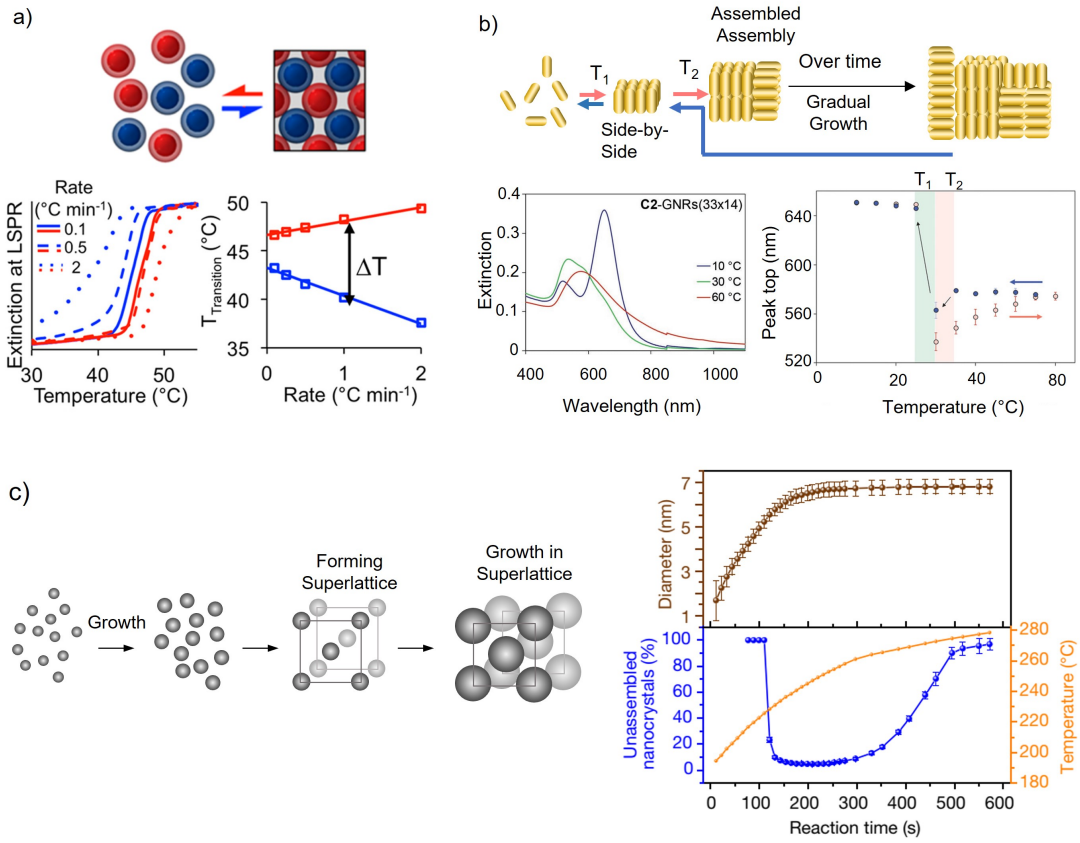

Figure 1.6.1: Temperature-driven self-assembly of nanoparticles. a) DNA-coated gold nanoparticles aggregate at lower temperature (blue points) and redispersed at higher temperatures (red point). The rate of applied temperature affect the temperature at which aggregation and redispersion occurs that is due to lag in system response to applied stimulus. Figure adapted from reference [59]. b) HEG-stabilized gold nanorods aggregate with increasing temperature. At moderated temperature (30 °C) nanorods form side-by-side assemblies while at elevated temperature (60 °C) nanorods form hierarchical structure. Figure adapted from reference [60]. c) Temperature-induced self-assembly of Pd nanoparticles into highly crystalline superlattices that commences just after the nanocrystal are formed. Superlattice formation was explained by change of inter-particle potential, caused by increasing the size of nanoparticles. Nanoparticles assembled into an fcc-lattice and kept growing after lattice formation. Figure adapted from [61].

Temperature is a physical stimulus affecting uniquely the molecular shell of nanopar-

ticles. O'Brien et al. have used real-time UV-Vis analysis to investigate the temperature dependent self-assembly of gold nanoparticles coated with DNA[62](Figure 1.6.1 a). It is know that at low temperature DNA molecules hybridize to from double stranded DNA while upon heating melting occurs producing single stranded DNA. Thus anchoring two different types of DNA to separate batches of gold nanoparticles is a convenient way to study temperature-driven reversible clustering of nanoparticles. The authors tracked in situ the change of extinction at the LSPR between 30 and 60 °C for different temperature rates and observed the appearance of thermal hysteresis that was explained by the so-called critical undercooling, a thermodynamic barrier which needs to be overcome for the onset of aggregation. The authors found that the aggregation temperature T_f was affected by temperature scan rate, while the melting temperature T_m show little variation even at higher temperature rates.[59] Interestingly, the number of coordination sites (valency), trough which nanoparticles, can interact also affected the extent of hysteretic response. That is, by controlling particle shape (plate, spheres) and the DNA sequence, authors could increase valency from 2 , 8 and 12, leading to different packing of nanoparticles in the superlattice. The packing determined how the system responses to the temperature change. With increasing valency the critical undercooling was favored leading to the drop of T_f, hence widening the hysteresis. This work is an example showing that only through real-time analysis of the self-assembly process new features and thus new knowledge of the system response can be extracted.

Iida et al. have combined hexa(ethylene glycol) (HEG) and gold nanorods to produce thermoresponsive system. Upon temperature increase to 30 °C, the LSPR blue-shifted indicating side-to-side arrangement of small, precursor clusters (Figure 1.6.1 b). Further temperature increased to 40 °C the precursor clusters formed hierarchical superstructures through tip-to-tip assembly, leading to an increased extinction at longer wavelength. Upon cooling the process was reverted, first to form side-to-side precursors, and finally redispersion. The mechanism of clustering was explained by reversible dehydration of HEG ligand at elevate temperatures, where the dehydration temperatures were sensitive to the particle curvature, that is, lower at the flat lateral parts and higher at the curved tips.[60] It is worth noting, that this two-step assembly was not observed for spherical particles with the same ligand,[63] a difference that may not have been observed without implementing real-time UV-Vis measurements.

In another example, Wu et al. have found the formation Pd nanocrystals in 1-octadecene and their simultaneous self-assembly to superlattice at high temperature.[61] Normally, self-assembly of nanoparticles into superlattices requires slow solvent evaporation at room temperatures. In the work by Wu et al., a quite opposite scenario was detected thanks to the use SAXS in real time. At elevated

temperatures (230 °C), spherical Pd nanocrystals first formed, and after reaching a critical diameter of 5 nm, they rapidly assembled into a superlattice with continuous nanocrystals growing within superlattice. Through calculating interaction potential, the authors have identified an interplay of repulsion (ligand) and attraction (core-core attraction) as driving forces of assemblies formation, leading to a thermodynamically driven crystallisation mechanism. The generality of this phenomena was confirmed by changing core materials: iron oxide. Through their findings obtained from in-situ measurements, they were able to design nanocrystals to demonstrate temperature-dependent reversible assembly/disassembly by tuning the ligand grafting density and surface ligand composition (Figure 1.6.1).

1.6.2 Light

Light is a physical stimulus that can be applied remotely, at high frequency between between ON and OFF states, and at desired energy and intensity.

A classical example of reversible clustering of metal nanoparticles with light is based on structural change of surface ligands (photoswitch), such as azobenzene or spyropirans derivatives, which undergo cis to trans isomerization under UV light irradiation followed by it recovery to stable isomer under visible light or thermal relaxation. When photoswitch is immobilised on the particles surface and UV light is applied, the change of isomerization alter wetting properties of the particles surface altering inter-particles forces, hence aggregation. That is, initially stable particles in non-polar solvent (cis isomer) become more hydrophilic when switched to trans isomer under UV irradiation, leading to particles aggregation.[64]. The relatively slow kinetics of particles aggregation/disaggregation make the in-situ UV-Vis study less interesting. Nevertheless, Kundu et al. [65], by studying nitrospiropyran-based photoswitch, have found that this ligands undergo fast back isomerization (seconds) after canceling UV stimulus, that is, nearly three order of magnitude faster than azobenzene. Thus, the use of UV-Vis in real time was implemented to study disassembly kinetics (or lifetime of aggregates) for different molar content of nitrospiropyran on the nanoparticles (2.6 nm in diameter). When molar content of nitrospiropyran was increased from 60 to 90%, the lifetime increased by half from 9 to 72 seconds. Such tendency was explained by the attractive interaction between nitrospiropyran molecules on nanoparticles surface, that slowed down the kinetics of back isomerisation (Figure 1.6.2).

Another way to control clustering of nanoparticles by light is taking the advantage of photo-thermal effect where metallic core produces local heat that in turn changes the structure of thermoresponsive surface ligand, leading to aggregation. Poly-N-isopropylacrylamide (p-NIPAM) is a typical thermoresponsive polymer that undergo

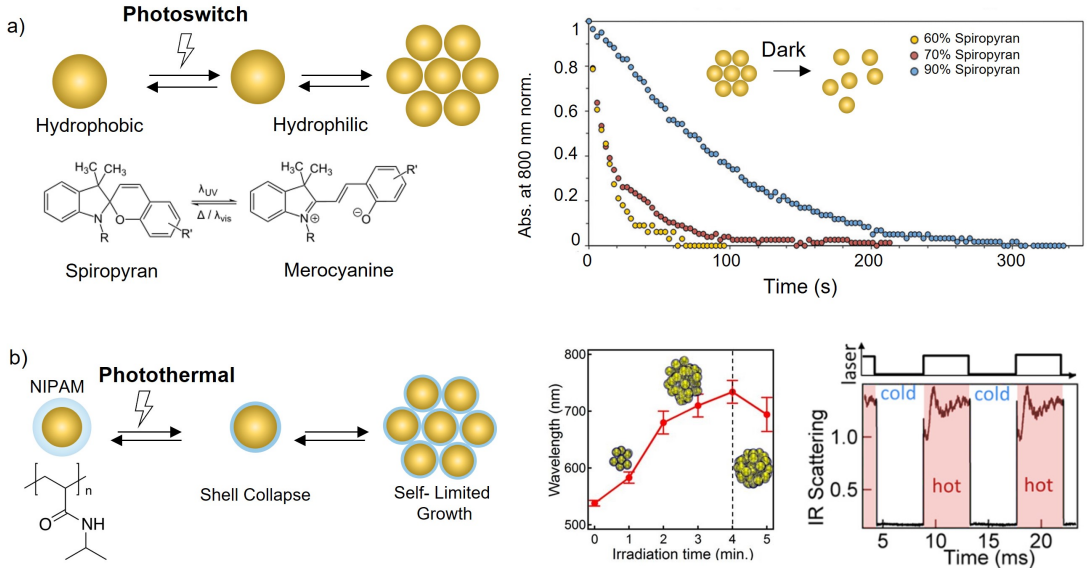

Figure 1.6.2: Real-time spectroscopy measurements for light induced dynamic self-assembly of nanoparticles. a) Light-induced self-assembly of gold nanoparticles using a photoswitch. Gold nanoparticles aggregated under UV-light irradiation and disassembled in the dark. The kinetics of disassembly could be adjusted by the concentration of photoswitch on the nanoparticle surface. Adapted from reference [65]. b) Light-induced self-assembly of gold nanospheres coated with p-NIPAM exploiting photothermal effect. AuNPs aggregated under light exposure and a self-limited growth was observed due to collective coulomb repulsion of individual particles inside a cluster. They demonstrated a strong and fast restoring force upon cooling. Adapted from reference [62].

phase transition at 36 °C. At low temperature, the polymer form multiple hydrogen bonding with water molecules, allowing its hydration and thus expansion. At such conditions nanoparticles remain stable. Once the temperature is bring above transition temperature, the hydrogen bonds break, water molecules are expel from polymer structures and polymer collapses, facilitating aggregation of nanoparticles. The process is reversible. Ding et al. [62] have used real-time UV-Vis optical characterisation to show very fast response of aggregation process under light irradiation (Figure 1.6.2). By analysing UV-Vis spectra, they found a self-limiting growth of aggregates over time during laser excitation. They could confirm this observation by calculating interaction potentials, showing that for a growing cluster size, repulsive forces increase due to collective coulomb repulsion of the charged nanoparticles. By using IR scattering, μs response was observed between assembled and disassembled states. Although the actual process was probably faster, the measurement technique had insufficient time resolution. Nevertheless, they showed, that large forces (nN) can be released in short times (sub-μs), which is an important key feature for fast nanoscale actuators.

1.6.3 pH

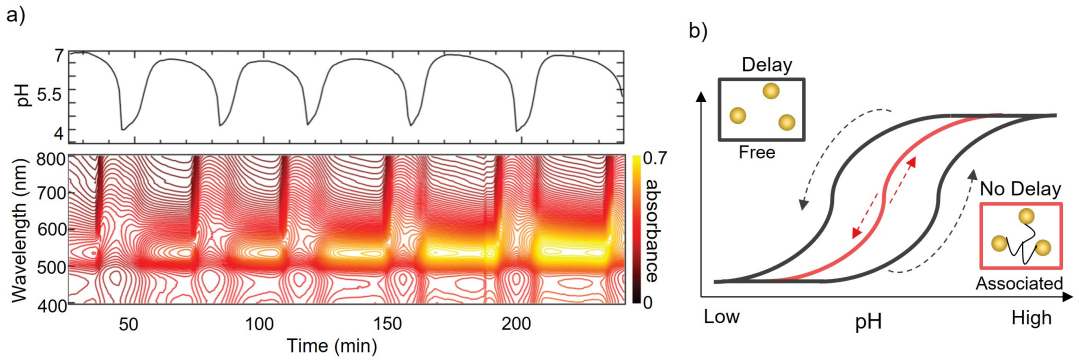

Figure 1.6.3: pH-induced reversible clustering of nanoparticles. a) Reversible clustering of gold nanoparticles (lower panel) follow temporal change of pH oscillator (upper panel). b) Schematic description of different (dis)assembly pathway of pH-responsive gold nanoparticles in presence of pH oscillator. Depending if AuNPs are free in solution or pre-associated (for example through a polymer network) they showed a delayed response to changing pH instead of following them perfectly, which results in hysteresis. Adapted from references [66, 67]

The concentration of proton is one of the most versatile chemical stimulus. To study dynamic self-assembly of nanoparticles pH oscillators were implemented. A pH oscillator is a set of coupled chemical reactions of different kinetics parameters leading to the sequential concentration change of each component which in practice is reflected in the oscillatory change of pH. Often, the change of pH is accompanied by the change of color of the solution giving rise to the so-called chemical clock. Since a solution containing dispersed or aggregated gold nanoparticles exhibit two limiting colors detectable by naked eye, coupling of pH oscillator to the reversible clustering resulted a convenient way to exploit the systems chemistry. To study pH oscillator one need to assure time-resolve spectral and pH analysis of the solution to be able to determine whether both process (chemical and colloidal) are coupled. Nabika et al.[66] have nicely shown that gold nanoparticles functionalized with 12-mercaptododecanoic acid can be coupled to standard pH oscillator ($BrO^{3-}/SO_3^{2-}/HSO^{3-}$) that operates within the limiting pH values raining from 4 to 7 and of a period of few minutes timescale (Figure 1.6.3 a). The authors observed a large hysteresis in each pH-cycle that was attributed to the delay ions diffusion to the center of the clusters to induce redispersion, resulting in bistability of colloidal state at a given pH-value (Figure 1.6.3 b - black lines).

A different scenario was presented for pH-responsive AuNPs functionalized with NIPAM containing -COOH endgroups.[67] In this case, AuNPs followed fast pH changes without any delay. They addressed this to pre-associated AuNPs, that are connected via crosslinked chains of NIPAM (Figure 1.6.3 b - red inset). In

their dispersed state, they have short inter-particle distances (18 nm), which keeps diffusion distance low and allows for a rapid response. They further tested this hypothesis by increasing the pH oscillator frequency with increasing temperature and injection rate and AuNPs were still able to follow pH-changes.

1.6.4 Magnetic field

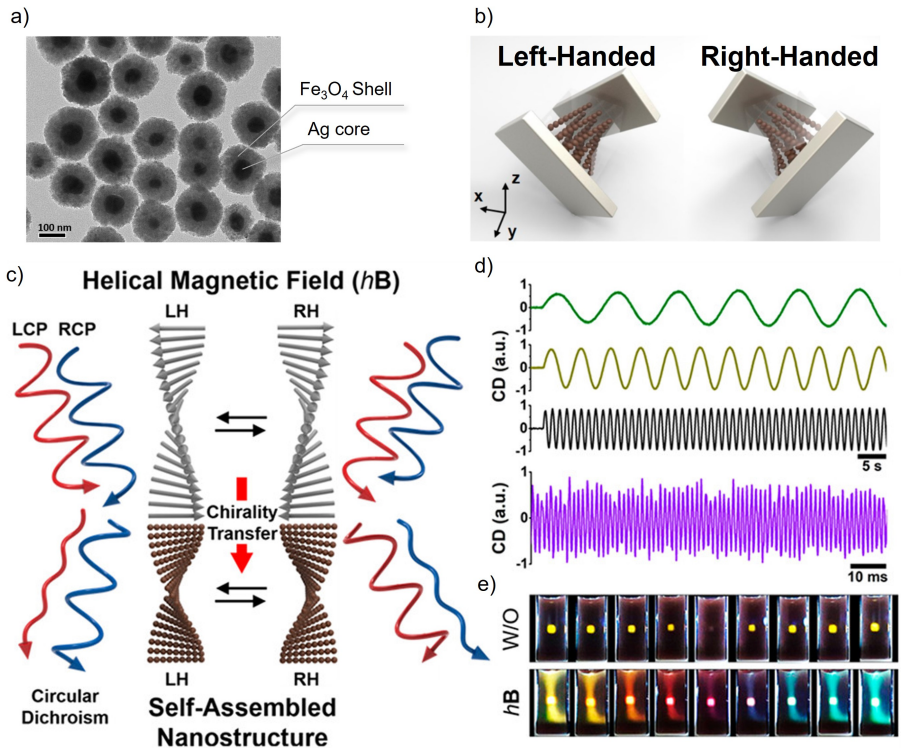

Figure 1.6.4: Self-assembly under magnetic field. a) TEM image of iron-coated silver nanoparticles. b) Assembled structure of helical nanochains under helical magnetic field at right and left handed rotations (c) Scheme of helical field-induced chiroptical properties where rotating magnetic field induces chirality into self-assembled nanostructures. d) effect of revolutions per minutes of rotating field on the frequency change of circular dichroism. e) change of transmitted color for different polarization angles. Adapted from reference [68].

The convenience of using magnetic field to self-assembly and modulate is based on immediate response of the system to the applied stimulus and does not require the use of templates to produce precise self-assembly. Jeong et al.[68] have built a helical superstructures that displayed switchable chiroptical properties (Figure 1.6.4). They used hybrid nanoparticles comprising both plasmonic (silver) and magnetic (magnetite) components. While under external magnetic field nanoparticles formed chain-like assemblies, under helical magnetic field a chiral helical assemblies formed. Such chiral structures gave rise to circular dichroism, which handedness was dynamically switched by the helical magnetic field at the millisecond level. Thus, the larger the rotation of the magnet, the larger was the frequency of changing handedness.

The interaction of the chiral structures with light was used to built a display which transmitted light of different wavelengths depending on the angle of light polarization. Overall, these results showed that magnetoplasmonic nanomaterials bring the potential for practical applications in optical devices.

1.6.5 Electric Field

Electric field is another convenient physical stimulus to modulate the interactions between charged nanoparticles and thus to tailor their collective optical properties. Montelongo et al.[69] have proposed reversible electrotunable liquid mirror based on voltage-controlled reversible assembly of gold nanoparticles at the interface of two immiscible solutions. They used gold nanoparticles of 16 nm in diameter and functionalized with 12-Mercaptododecanoic acid. Upon the applied voltage, the nanoparticles self-assembled at an interface of two immiscible liquids, leading to progressive increase the reflectance (Figure 1.6.5 a). The authors have found that the assembly time of nanoparticles on the liquid-liquid interface was inversely proportional to the square of the nanoparticles concentration, being in accordance with the diffusion-driven assembly process. The disassembly time was independent of the concentration of nanoparticles. Although, in general, the dynamics of assembly was rather slow (10 minutes), which was determined by diffusion of nanoparticles over long distances, the dynamics could be sped up by orders of magnitude via miniaturization of their electrochemical cell. Thus, the authors were able to construct a device for nanoplasmonic platform to switched between highly reflective mirror-like and transmissive window.

Charged colloids are known to diffuse towards their counter charged electrodes under an applied voltage bias in a process known as electrophoresis. Yu et al. [70] have studied the electric field-induced assembly of dodecanethiol functionalized silver nanoparticles of 7.1 nm (Figure 1.6.5 b). In a home-made liquid cell equipped with electrodes and in-situ SAXS measurements, the authors observed that nanoparticles drift to the anode under an electric field, because the adsorption of Br^- at the surface, rendering a negative surface charge. The SAXS analysis helped to establish relationship between applied voltage, flux of nanoparticles, nucleation density and superlattice constant. Interestingly, they observed a size focusing effect from cathode to anode. That is, the bigger nanoparticles tended to accumulate on the anode with lower polydispersity than in the bulk solution. This facilitates back-diffusion of smaller NPs, while larger NPs drift towards the anode with less disturbance. Therefore, the superlattice was of high cristallinity and Bragg reflections of higher order were clearly visible.

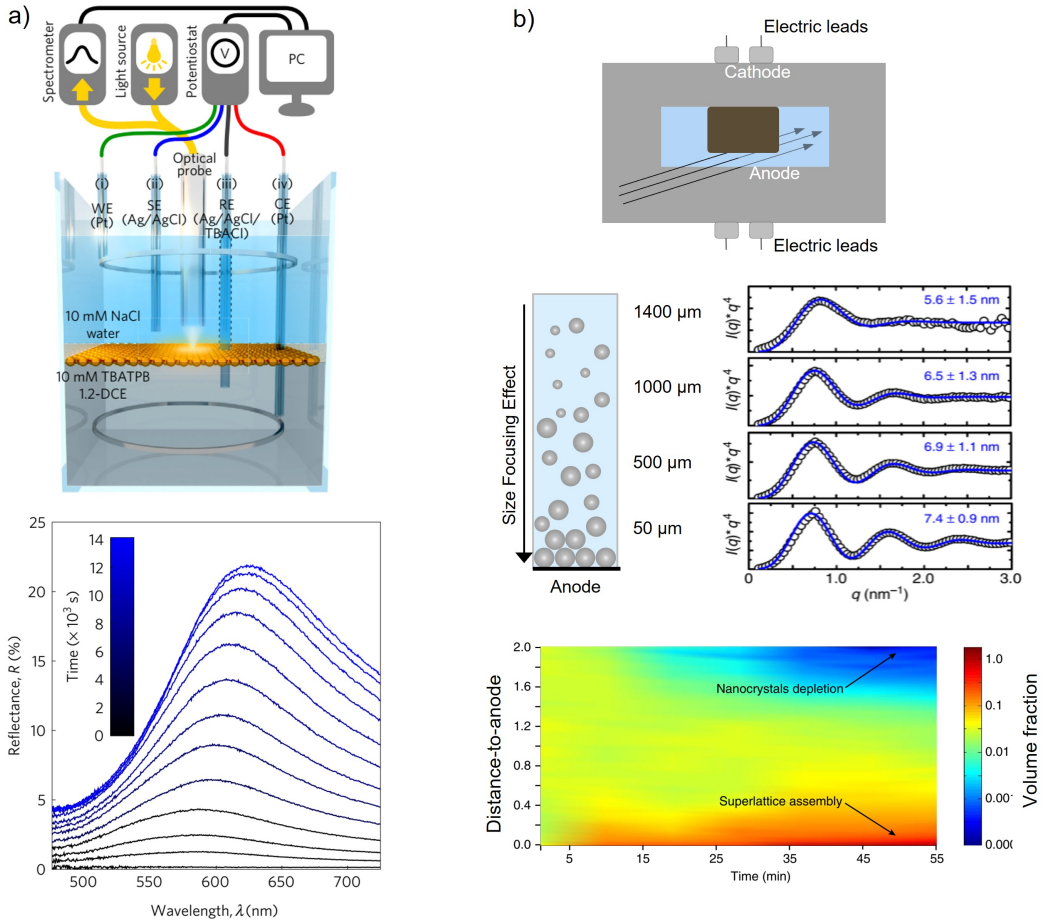

Figure 1.6.5: Self-assembly of nanoparticles modulated by electric field a) Interfacial self-assembly driven by an electric field to produce switchable surface of reflective and transitive properties. Adapted from reference [69]. b) Electric field-induced self-assembly of silver nanoparticles by SAXS measurements showing the formation of ordered lattices through size-focusing effect. Adapted from reference [70].

1.6.6 Pressure

Pressure is gaining an attention as a physical stimulus in the reversible clustering of gold nanoparticles. Schroer et al. have studied the pressure-induced supercrystal formation of spherical (6 nm)[71] and rod-like (75 x 21 nm)[72] nanoparticles stabilized with polyethylene glycol in aqueous solution with a high-ionic strength (Figure 1.6.6). The clustering process was explained by pressure-induced removal of water from polymer brush on the particles surface (dehydration), leading to its collapse and progressive clustering of nanoparticles. While spherical particles required 3000 bar to form fcc-superlattice, gold nanorods required 2050 bar to obtain two-dimensional hexagonal superlattices. By studying the assembly process with ms resolution, they found that the crystal quality for spherical gold nanoparticles improved and the kinetics of crystal formation accelerated with the magnitude of the applied pressure jump. While assembly process showed exponential kinetics,

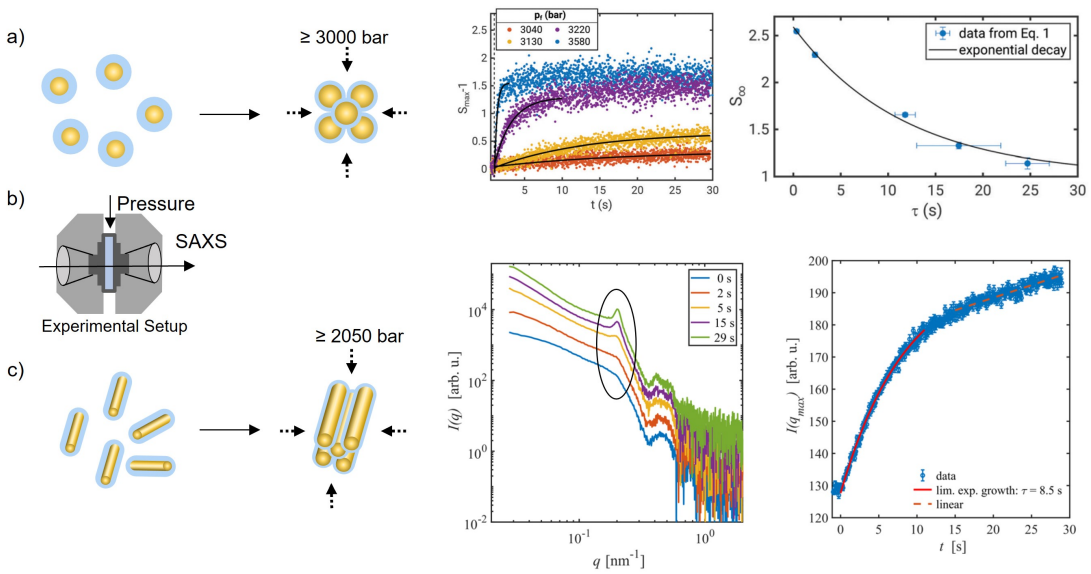

Figure 1.6.6: Pressure-induced self-assembly of gold nanoparticles and -rods coated with polyethylene glycol measured in-situ by SAXS. a) Gold nanoparticles assembled into fcc lattice above 3000 bar. The higher the pressure, the better the crystal quality and the faster the assembly kinetics. Adapted from reference [71]. b) Experimental setup for in-situ SAXS measurements. c) Gold nanorods assembled into a two-dimensional hexagonal lattice above 2000 bar. Time-resolved studies revealed a exponential growth of the superlattice during a period of 15 seconds, which then slows down to linear growth. Adapted from reference [72].

disassembly showed linear kinetics and where about 1 magnitude slower. For gold nanorods, a decrease of superlattice was found by increasing the pressure up to 4000 bar, indicating additional dehydration of the polymer shell. Time resolved studies showed rapid superlattice formation with initial exponential kinetics. Generally, assembly kinetics were in a similar range for both types of particles.

The above-disscussed works clearly show the importance of implementation of real-time analytics in dynamic self-assembly of nanoparticles. It offers a unique tool in understanding not only the mechanisms of self-assembly, but also provide a totally new means in detecting unexpected signatures that can emerge upon forward or backward application of the stimulus. It is also clear that all intermediate states of dynamic assemblies remain inaccessible to a conventional ex-situ analysis which is capable of describing the equilibrium state of the assemblies. Finally, the fast dynamics of reversible self-assembly and proper coupling with the stimulus can pave the way towards new optoelectronic devices.

CHAPTER 2

Controlling hysteresis in reversible clustering of nanoparticles

2.1 Introduction

Hysteresis is defined as the dependency of the state of a system on it's history and it is ubiquitous in the living and non-living world. It is manifested through loops of input and resulting output. Apart from being a core feature in solid-state devices (*e.g.,* memory storage), hysteresis sustains the functioning of many biological processes (*e.g.,* cell division) through the resilience against noise.[73–77] The studies of hysteresis require the use of suitable model systems. Without any doubt, one of such systems are gold nanoparticles (AuNPs) that exhibit chemical robustness under harsh conditions and optical properties sensitive to the change of their colloidal phase.[6, 58, 63, 78–81]

Previously, Grzybowski and co-workers have studied hysteresis in the reversible clustering of gold nanoparticles stabilized with ionizable ligands using pH as a stimulus.[82] These authors suggested that the hysteresis emerges from the change of magnitude of electrostatic repulsion that overcomes the energy barrier during the cyclic transitions between aggregated and dispersed states. The redispersion of nanoparticles required an extra change of pH to bring the nanoparticles out from the energy minimum. Importantly, the nanoparticles remained stable for several months once in aggregated state, indicating a local equilibrium adapted by the system over an entire range of applied stimulus.

Mirkin and co-workers, on the other hand, have observed hysteresis between the melting and freezing transitions of DNA-coated gold nanoparticles.[59] The emergence of hysteresis was explained through critical undercooling, a temperature drop below melting temperature of DNA strands to reach thermodynamic barrier of nu-

cleation. In this type of systems, the change of state is independent of the rate of applied stimulus, and the emerging hysteresis is classified as *rate-independent*.
An entirely different scenario represents *rate-dependent hysteresis* that originates from a lag of the system response to a stimulus. The faster is the velocity of the applied stimulus, the wider becomes the hysteresis;[77] it is a kinetic effect. Rate-dependent hysteresis has been observed in pH-driven clustering of AuNPs stabilized with carboxylated alkanethiols,[66, 83–85] poly-L-lysine,[86] and thermoresponsive polymers demonstrating an upper[87] or lower[88] critical solution temperature.
Despite a vast body of works devoted to dynamic self-assembly,[89–94] the hysteresis, when observed, receives mainly a qualitative description, needless to mention the lack of experimental control over its rate-dependent or rate-independent components. A reason for this is an insufficient time-resolution of data acquisition (*e.g.,* spectroscopy) that could otherwise aid information and understanding of intermediate states in such systems. The knowledge of the type of hysteresis is central to predicting how the system responds to a stimulus.
Rate-dependent hysteresis helps to describe the nonlinear relationship between the input stimulus and the output state, as in piezoelectric actuators.[95] Rate-independent hysteresis, on the other hand, is a principle of memory storage, homeostatic materials [96], autonomous chemical reactions [97] and erasable inks. [98] Therefore, determining the signatures of the system response to a stimulus is a must in the development of functional nanosystems for (bio)sensors, actuators or catalysis.
In this chapter, it has been asked what is the origin of thermal hysteretic behavior during reversible clustering of nanoparticles and what are the experimental parameters that define the prevalence of either rate-dependent or rate-independent components.

2.2 Results and discussion

2.2.1 System Design

Figure 2.2.1 shows the conceptual design of the system comprising AuNPs of 13.2 ± 1.0 nm in diameter stabilized with bis(p-sulfonatophenyl)phenylphosphine dihydrate dipotassium salt (BSPP) [99]. The nanoparticles were embedded in agarose gel. Upon a temperature drop from 45 to 5 °C, the initial red colour of the sample progressively turned to blue-grey (Figure 2.2.2 a) and recovered by heating up to 45 °C.
UV-Vis-NIR spectra and temperature values of the samples were recorded simultaneously every 10 seconds (1000 spectra per run), observing that the localized surface plasmon band became featureless at 5 °C and recovered upon heating (Fig-

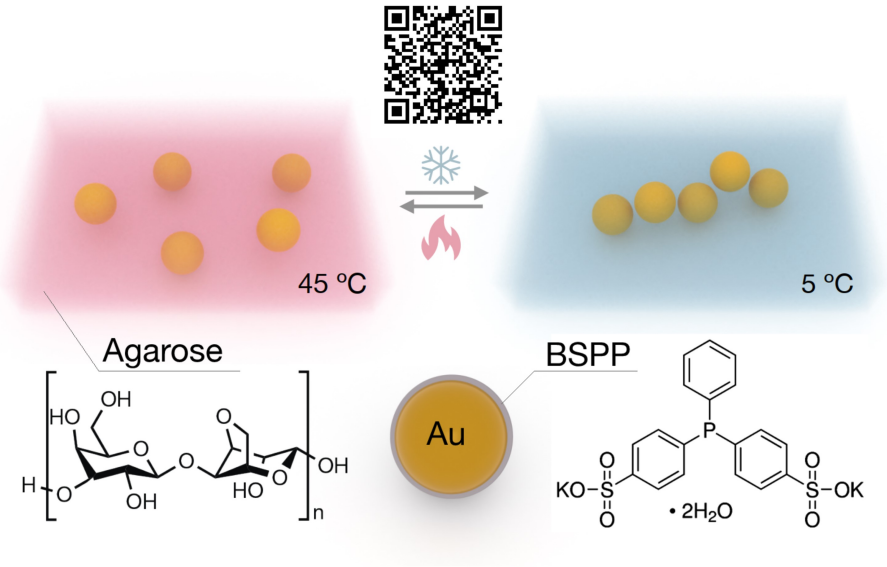

Figure 2.2.1: Working principle of reversible clustering of BSPP-stabilized gold nanoparticles within agarose matrix. The difference in disassembly and clustering temperatures originates the emergence of hysteresis. The QR code in the inset provides a link to the video showing how the particles undergo reversible clustering.

ure 2.2.2 b). By excluding time component and presenting a degree of assembly ($R = Abs_{650nm}/Abs_{525nm}$) versus temperature, R follows different pathways depending on whether the sample is being cooled or heated, presenting hysteresis (Figure 2.2.2 c,d). Transmission electron microscopy (TEM) analysis showed the formation of globular aggregates upon temperature drop (Figure 2.2.2 d-inset).

DLS measurements confirmed the presence of hysteresis (Figure 2.2.2 e,f, and 2.6.1). The hydrodynamic diameter varied between 30 and ∼800 nm during heating and cooling, respectively (Figure 2.2.2 e). Note that prolonged storage of the sample at 5°C caused gradual sedimentation of the nanoparticles. To prevent the sedimentation at low temperature the cyclic clustering experiments from this point on were performed in agarose matrix with pore sizes of ∼600 nm in diameter (Figure 2.2.3). The pore size was determined by measuring UV-Vis-NIR spectra and calculating the wavelength exponent.[100] Extinction at 750 nm is representative for the formation of an agarose network. By following this wavelength, the wavelength exponent was calculated over time which is obtained from a linear regression of a double logarithmic plot of the turbidity $\tau(\lambda) = 2.3A(\lambda)/L$, where L is cuvette width in cm, versus wavelength, λ, from 700 nm to 800 nm. The pore size of 600 nm was estimated from the wavelength exponent plots from reference[101].

Since high concentration of agarose (1 w%) hinders aggregation optimal agarose concentration was found at 0.25 wt%. With higher agarose concentrations, both assembly and disassembly were hindered (Figure 2.2.3 d) increasing with concentration. At 0.25 w%, AuNPs had maximal mobility, while ensuring sufficient mechanical

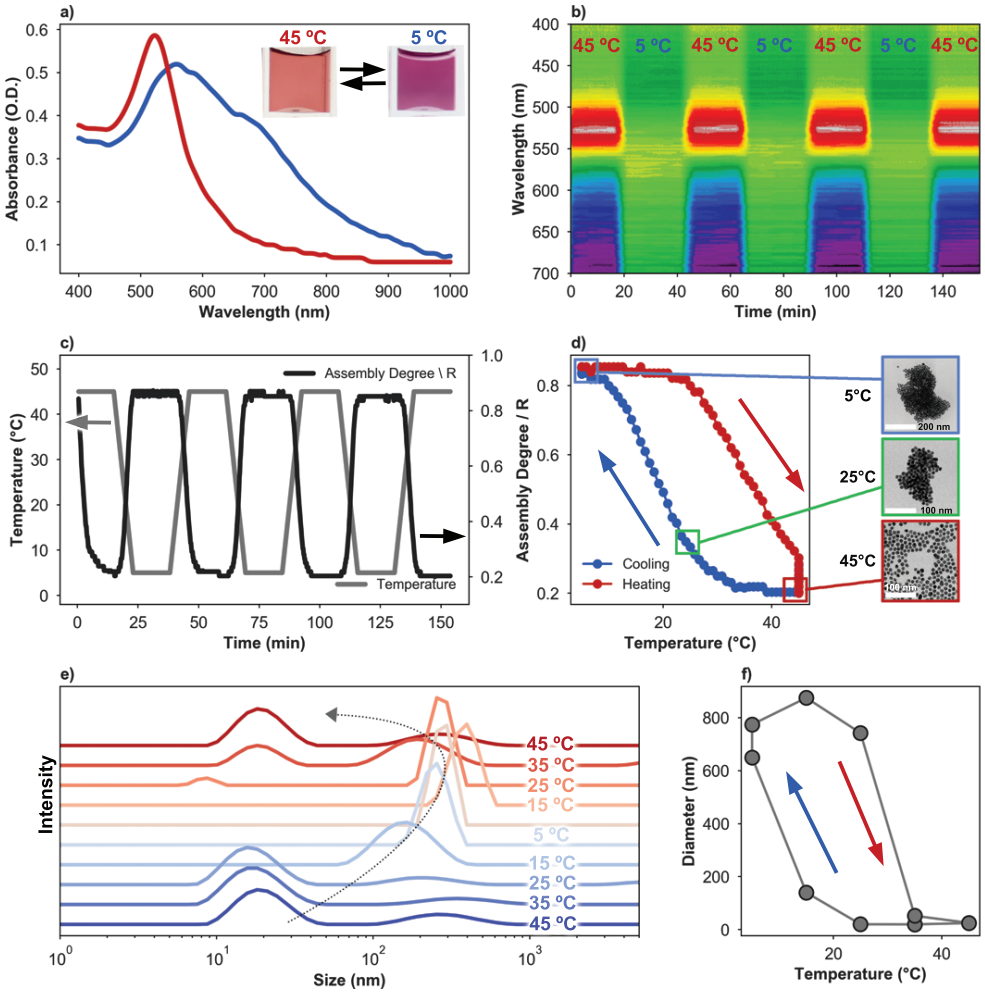

Figure 2.2.2: Temperature-driven reversible clustering of gold nanoparticles. a) UV-Vis-NIR spectra of redispersed (red, 45°C) and aggregated (blue, 5°C) nanoparticles. b) Four cycles of nanoparticles clustering at low and high temperatures. c) Time-dependent variation of temperature and assembly degree, *R*. d) Hysteresis of cyclic aggregation obtained by removal of time component in plot c. Insets: TEM images of clustered nanoparticles e, f) Change of hydrodynamic diameter of nanoparticles in colloidal phase at different temperatures confirming hysteresis.

strength of the hydrogel and still impeding precipitation of aggregates.

To assess to what extent a temperature gradient influences the hysteresis, the nanoparticles were aggregated cyclically in cuvettes of different path lengths. Figure 2.2.4 shows visual representation of possible temperature gradient in the experimental setup. The optical path of UV-Vis recording is oriented vertically, and the source of heat/cold is supplied from the bottom of the cuvette. Upon heating, the disassembly starts from the bottom (red area) while on the upper part of the cuvette larger aggregates remain (blue area). In such a scenario, there is a size distribution of clusters across the optical path - vertical axis (Figure 2.2.4 a). As a result, one could expect that temperature gradient imposes broadening of optical response across the beam light and hence the origin of the hysteresis. The effect of

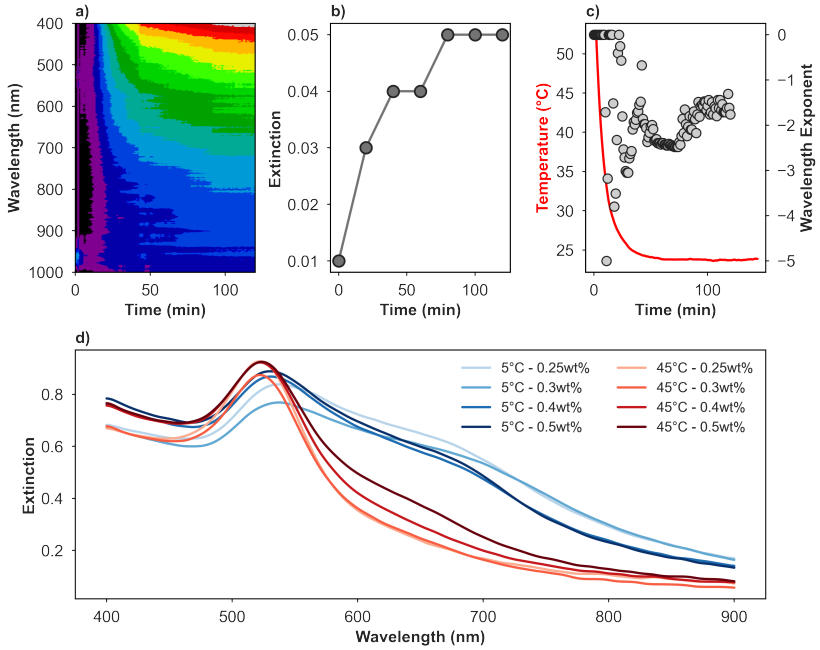

Figure 2.2.3: Agarose pore size determination and effect of agarose concentration. a) Surface plot of extinction between 400 nm and 1000 nm. b) Represntative extinction at 750 nm, indicating the formation of agarose network. c) Wavelength exponent and temperature over time, immediately after gel preparation. d) Influence of agarose on extent of clustering. With increasing agarose concentration, the responsiveness of temperature decreases because of immobilization of AuNPs in agarose matrix.

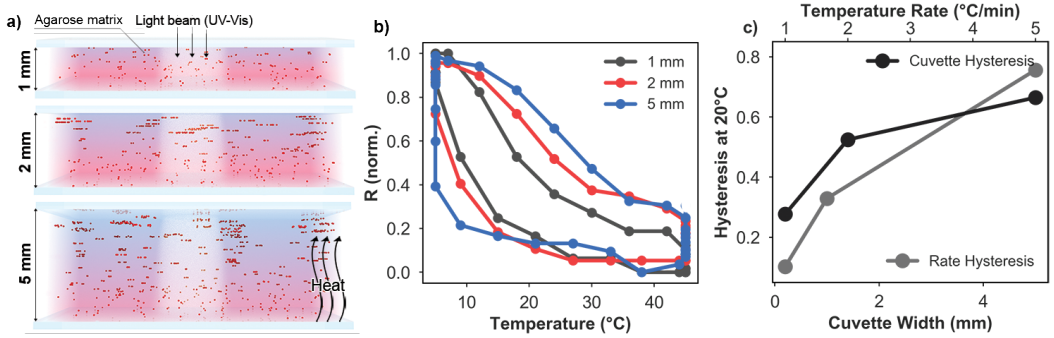

Figure 2.2.4: The effect of temperature gradient on hysteresis. a) Visual representation of the possible temperature gradient for cuvette of different path lengths. b) Hysteresis of reversible clustering for cuvette thickness of 1, 2 and 5 mm. c) The change of hysteresis at 25 °C versus the velocity of temperature scan rate (upper horizontal axis) and cuvette thickness (bottom horizontal axis).

temperature gradient on the magnitude of hysteresis was evaluated, by performing reversible clustering with cuvettes of different path lengths: 1, 2 and 5 mm. The hysteresis increased with increasing the thickness of the cuvette (Figure 2.2.4). For the cuvette of the lowest path length (1 mm), the hysteresis remains visible. Note that although the hysteresis can be further decreased by slowing the temperature ramp down to 0.2 °C/min in 1 mm thick cuvette, it cannot vanish entirely.

2.2.2 Centering hysteresis within temperature window

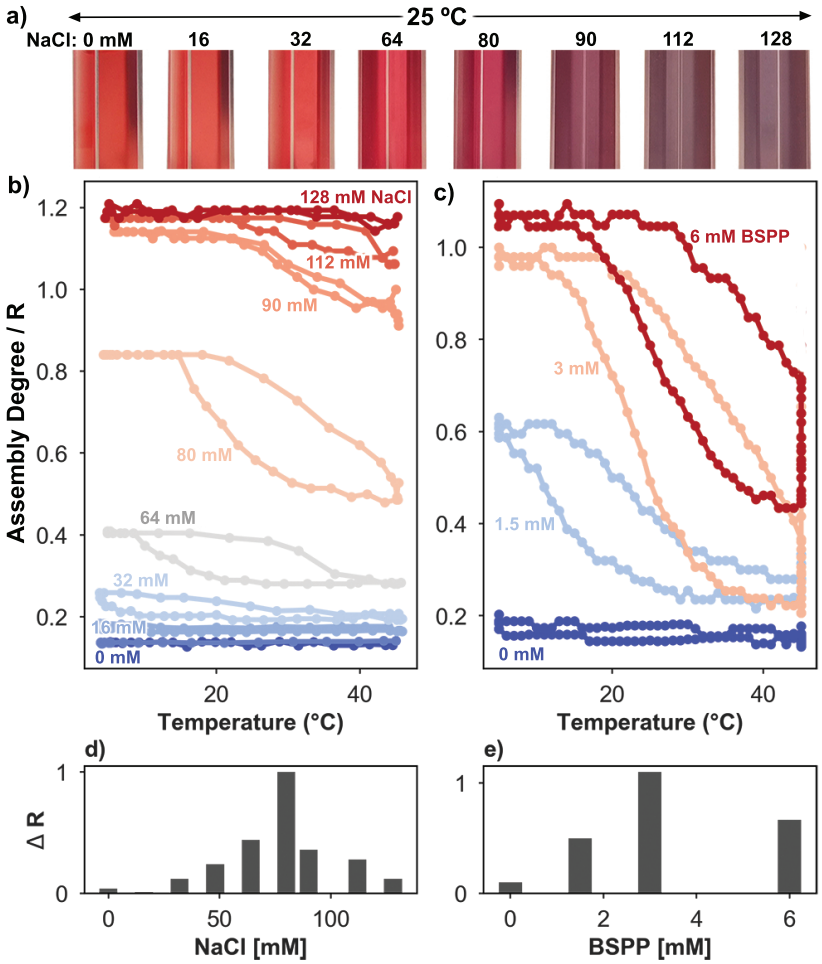

Figure 2.2.5: The effect of NaCl and BSPP concentration on the centre and saturation of hysteresis. a) Digital images of solutions containing gold nanoparticles in agarose matrix with increasing concentration of NaCl at 25 °C. b,c) With increasing the concentration of a) NaCl and b) BSPP the centre of hysteresis shifts to higher temperature at 1 °C/min. d, e) The change of responsiveness of the system ($\Delta R = R_{max} - R_{min}$) to the concentration of NaCl d) and BSPP e).

The concentration of both salts NaCl and BSPP regulates the centre of the hysteresis in the temperature window of 5 - 45 °C. Note that BSPP is also a surface ligand here that binds to gold surface via phosphine group and ensures negative surface charge. With increasing NaCl concentration from 0 to 128 mM at room temperature, the red color of the samples turned blue (Figure 2.2.5 a). Cyclic cooling/heating each of these samples revealed that the change of assembly degree, R, is the highest for intermediate salt concentrations (64, 80 and 90 mM) and negligible for limiting concentrations (16, 120 mM) (Figure 2.2.5 b, d). Consecutively, the centre of the hysteresis moved towards high temperature as salt concentration increased. A threshold concentration of BSPP (1.5 mM) was needed to observe reversible aggregation, suggesting that BSPP molecules increase the ionic strength

of the solution and favour cooperativity between free BSPP and attached to the surface of the nanoparticles (Figure 2.2.5 c). Similar scenario has been observed for free polymer molecules in temperature-driven aggregation of nanoparticles stabilized with poly(N-isopropylacrylamide).[79, 102] Here, the change of assembly degree received the highest values at BSPP concentration of 3 mM. As for NaCl, the increase of BSPP concentration moved the centre of hysteresis towards higher temperature. BSPP, however, alters the hysteresis at a larger extent. It was speculated, that the surface charge of AuNPs is screened twice as much by BSPP as compared to NaCl, that is due to the presence of two potassium cations per one molecule of BSPP. Replacing BSPP with an alternative ligand - triphenylphosphine-3,3',3"-trisulfonic acid trisodium salt - had similar effect on the hysteresis (Figure 2.6.3).

To confirm the effect of temperature and salt concentrations on reversible aggregation, interaction potential between nanoparticles were calculated by using Derjaguin, Landau, Verwey, and Overbeek (DLVO) theory[103] (Figures 2.2.6 and 2.2.7). DLVO comprises attractive, temperature-independent van der Waals potential and repulsive, temperature-dependent electrostatic potential: $V_{tot} = V_{vdW} + V_{elec}$. For nanoparticles of similar size the van der Waals and electrostatic potentials can be expressed as follow:

$$V_{vdW} = -\frac{AR}{12D} \tag{2.1}$$

$$V_{elec} = \frac{1}{2} RZe^{-\kappa D} \tag{2.2}$$

where A is the Hamaker constant for the Au/water/Au system (2×10^{-19} J), R is nanoparticle radius, D interparticle distance, Z interaction constant and κ Debye length. The Debye length receives the following form:

$$\kappa = \left(\sum_i \frac{z_i^2 e^2 n_{i\infty}^2}{k_B T} \right)^{1/2} \tag{2.3}$$

where z, e and n are ion valency of electrolite, elementary charge and concentration of electrolite. Note that in our system we have two type of electrolites: NaCl (1:1) and BSPP (1:2). The interaction constant, Z in equation 2.2 defines the repulsion of the electric double layer and can be calculated as follows:

$$Z = 64\pi\epsilon_0\epsilon \left(\frac{k_B T}{e} \right)^2 \tanh^2 \left(\frac{ze\psi_0}{4k_B T} \right) \tag{2.4}$$

In the equation (2.4), ϵ_0 and ϵ are the vacuum permittivity and relative permittivity for water, respectively, while ψ_0 is surface potential (mV) of nanoparticle which can be obtained from the surface charge density[104] (σ) (C/m^2) that in turns is given

by ζ-potential (mV):

$$\sigma = \frac{\epsilon_0 \epsilon k_B T}{ze} \kappa \left[2 \sinh \left(\frac{\zeta ze}{2 k_B T} \right) + \frac{4}{\kappa R} \tanh \left(\frac{\zeta ze}{4 k_B T} \right) \right] \tag{2.5}$$

$$\psi_0 = \frac{2 k_B T}{ze} \sinh^{-1} \left(\frac{\sigma}{\sqrt{8 k_B T \epsilon_0 \epsilon n_\infty}} \right) \tag{2.6}$$

Therefore, the ψ_0 in equation (2.4) can be estimated by measuring ζ-potential. The change of ζ-potential as a function of temperature was monitored experimentally, showing progressive decrease of ζ-potential with increasing temperature from 5 to 45 °C (Figure 2.2.6).

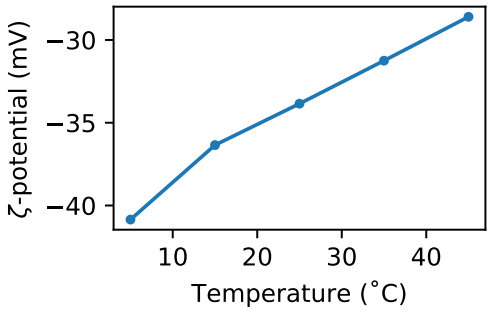

Figure 2.2.6: Experimental data showing the decrease the values of ζ-potential (approaching neutrality) with increasing temperature. Note that the change of ζ-potential is fully reversible. The value presented in the plot were used to calculate σ in eq. (2.5).

By taking into the account all experimental variables (nanoparticle radius, temperature, BSPP and NaCl concentrations as well as ζ-potential) interaction energy ($k_B T$) of nanoparticles was calculated as a function of inter-particle distance for varying temperature and ζ-potential at different NaCl concentrations and at constant BSPP concentration and nanoparticle radius (Figure 2.2.7). The calculations show that with the increase of NaCl concentration from 16 to 128 mM, the electrostatic repulsions drops progressively, making dominant Van der Waals (VdW) attractions. That is, at higher salt concentration (112 and 128 mM), the interaction energy is purely attractive where nanoparticles remain aggregated regardless of the temperature. Interestingly, at [NaCl] = 64 and 80 mM (optimum salt concentration for maximum ΔD - the difference between aggregated and redispersed states) the energetic barrier of electrostatic repulsion oscillates in the range of $\pm 5 K_B T$ above and below $0 K_B T$ with increasing and decreasing temperature, respectively. These numbers confirm that reversible clustering is the results of temperature-dependent changes of electrostatic repulsions. Note, however, although non-DLVO interactions were excluded from this model(short-range steric repulsion), as shown by Liu *et*

al.[99], the effect of temperature on the magnitude of electrostatic interaction energy is very much similar to the values reported by these authors. Therefore, the numerical results confirm the experimental data.

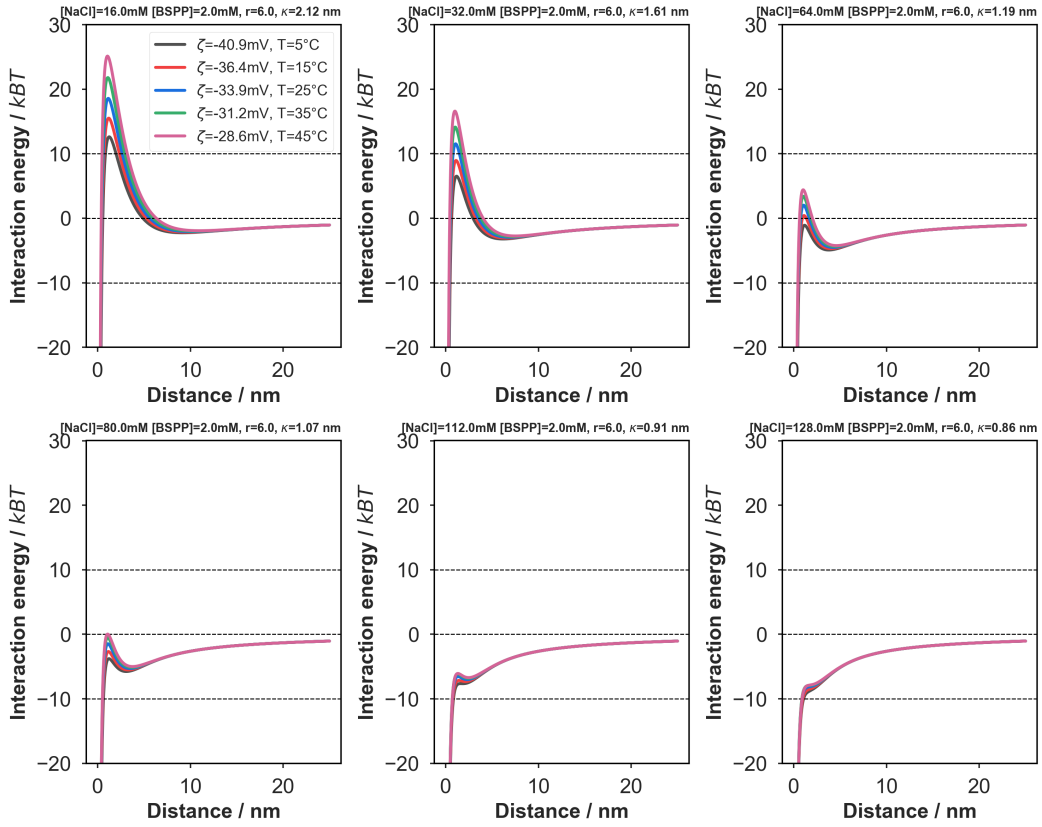

Figure 2.2.7: Calculated interaction energy between gold nanoparticles of radius 6 nm at temperature range between 5 and 45 °C for different NaCl concentrations. The electrostatic energy barrier decreases with decreasing temperature. The change of magnitude in the electrostatic energy barrier decreases with increasing salt concentration. At higher salt concentrations, nanoparticles remains aggregated regardless the applied temperature. κ in titles of each subplot stands for Debye length.

Next, the effect of particles concentration was investigated, observing that with increasing their concentration, the assembly degree increases since more particles are available to form clusters. As a result, the magnitude of hysteresis became larger (Figure 2.2.8). The centre of hysteresis, however, remained fixed at 20 °C regardless of the particle concentration, so did the onset temperature in the cooling direction, at which the aggregation begins. Overall, in contrast to the concentration of particles, it is the concentration of NaCl and BSPP that influences the width and the centre of hysteresis within the temperature range, confirming the central role of electrostatic screening in reversible clustering.

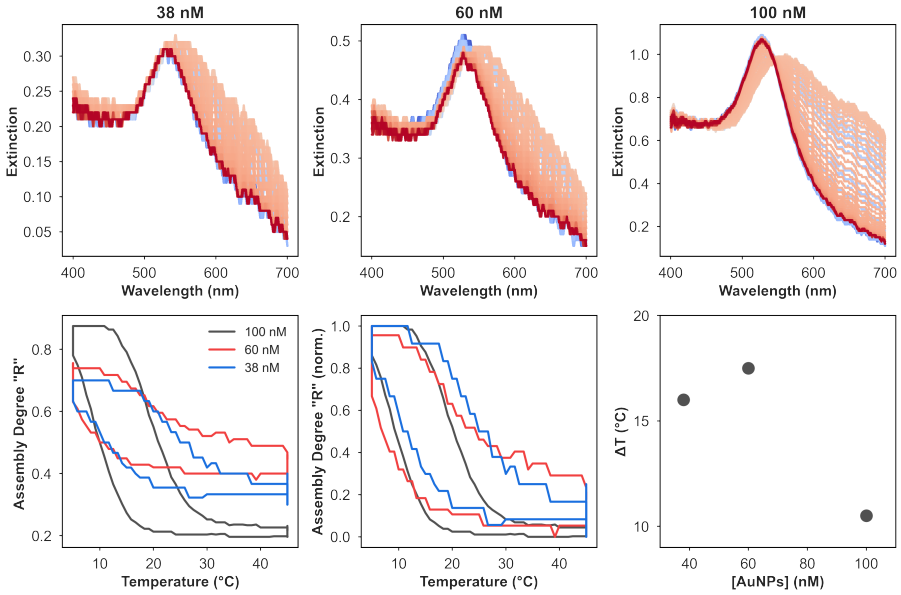

Figure 2.2.8: The effect of AuNPs concentration on hysteresis. The upper panel shows raw UV-VIS spectra for a cooling and heating cycles AuNPs@BSPP with increasing concentration from left to right. The higher is the AuNPs concentration, the higher is the extent of aggregation. The lower panel shows the analysis of the spectra: left: extinction at 650 nm showing that the magnitude of the hysteresis is higher for higher amount of nanoparticles; middle: assembly degree, and left: normalized assembly degree. The normalized data show that the coercivity of the hysteresis and onset temperature are similar for all samples, suggesting that effect of particles concentration has a minor effect on the observed hysteresis.

2.2.3 Disentangling rate-independent and rate-dependent hysteresis

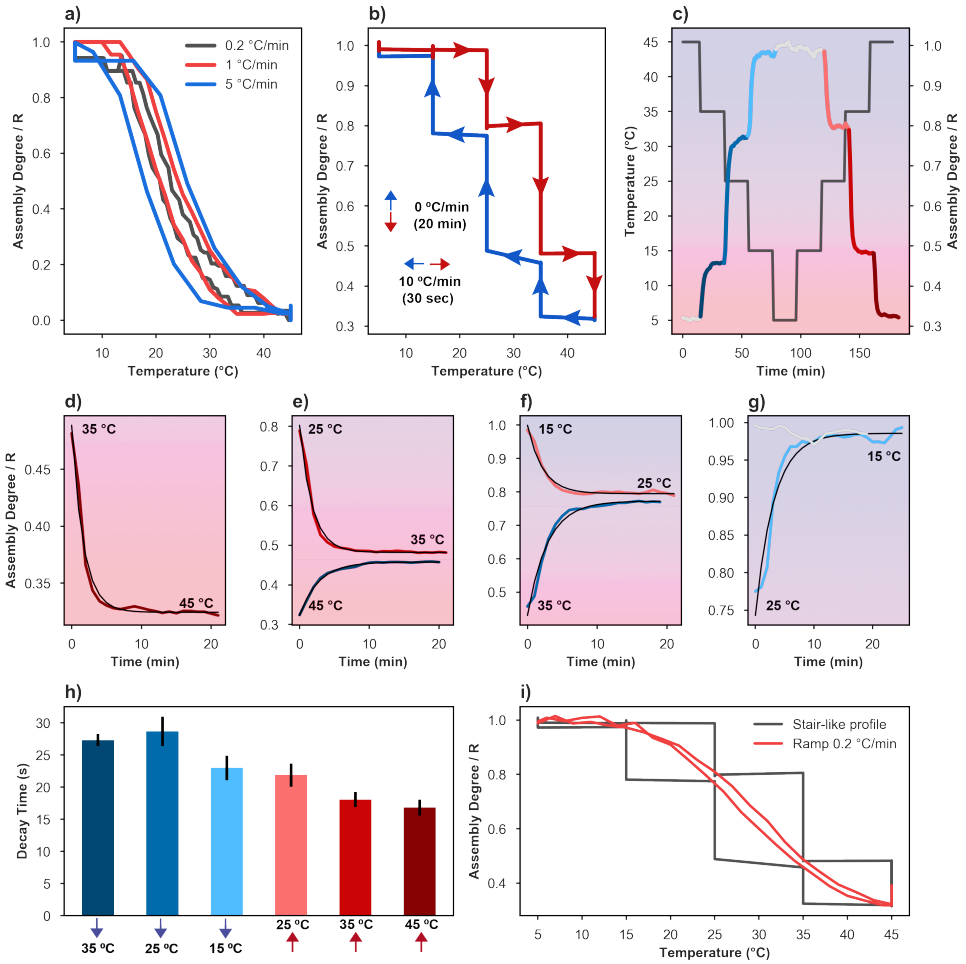

Figure 2.2.9: Rate-dependent and rate-independent component of hysteresis. a) The increase of hysteresis width for increasing the velocities of temperature scan, indicating rate-dependent hysteresis. b) The stair-like hysteresis allowing the relaxation (vertical lines) from dispersed and aggregated states. c) Time-dependent profile of relaxation dynamics for all assembly/disassembly processes from b. In grey, temperature profile. (d-g) Relaxation dynamics (taken from c) to given targeted temperatures. The gaps after relaxation to 35 and 25 °C indicate rate-independent hysteresis. h, i) Decay time constants obtained from (d-g). The disassembly is faster than clustering. All relaxation curves were fitted by $y = a\exp(-x/b) + c$. i) Assembly degree at continuous hysteresis (0.2 °C/min) coincide with assembly degree after relaxation in stair-like hysteresis, confirming rate-independent hysteresis.

To confirm rate-dependent hysteresis, cyclic clustering of the samples were performed by cooling and heating for three velocities of temperature scan (0.2, 1 and 5 °C/min), observing progressive broadening of the hysteresis (Figure 2.2.9 a). At the slowest scan rate, however, the hysteresis remained open (Figure 2.2.9 a). To confirm whether it is an artefact or a sign of thermodynamic hysteresis, we performed a

stair-like hysteresis where fast scans at 20 °C/min (horizontal arrows in Figure 2.2.9 b) were interrupted with a long relaxation period (20 min, vertical arrows in Figure 2.2.9 b) at 15, 25, and 35 °C, allowing the system to relax at a given temperature during heating or cooling process. As a result, the assembly degree after relaxation at 25 and 35 °C coincided with assembly degree of the uninterrupted scan at 0.2 °C/min (Figure 2.2.9 i). The hysteresis thus contains rate-independent component.

A high temporal resolution of optical data acquisition allowed to perform a qualitative analysis of the relaxation dynamics to targeted temperatures in stair-like hysteresis (Figure 2.2.9 b). At the cooling or heating step, a fast change of temperature caused an abrupt variation of the assembly degree followed by its slow relaxation (Figure 2.2.9 c). Pairwise comparison of relaxation profiles to a given temperature revealed the presence of a gap between assembly degrees of cooling and heating (Figure 2.2.9 e-f). Fitting the relaxations at targeted temperatures (45, 35, 25, and 15 °C) revealed that on average, the aggregation takes ∼10 seconds more than redispersion (Figure 2.2.9 h). This difference is an indirect signature of the origin of hysteresis. The clustering that is induced by cooling is a slow process in which the initially free nanoparticles diffuse to encounter each other to form clusters. In terms of the energy landscape, the particles are progressively "trapped" in the energy well. The lack of energy barrier allows the AuNPs to start clustering at the very beginning of the temperature drop. On the contrary, an extra thermal energy is required to induce disassembly making the electrostatic repulsion to overcome vdW attraction.[82] Once this extra energy is supplied, an abrupt redispersion commences, pushing the particles out from the energy well. Here, the extra energy is ensured at each stage of stair-like hysteresis, resulting in faster relaxation profile of heating than cooling. Such reasoning indicates that the assembly temperature is higher than the clustering temperature, hence leading to the emergence of hysteresis. These results corroborate with the previous report by O'Brien et al.[59] on the effect of undercooling as a origin of hysteresis in temperature-driven clustering of DNA-coated gold nanoparticles.

Both rate-dependent and rate-independent components are sensitive to the nanoparticle size. Increasing the diameter from 13, 19 to 39 nm, the hysteresis broadened for fast and slow velocities of temperature change (Figure 2.2.10 a,b). The size effect is more pronounced at a fast scan (5 °C/min), suggesting that the size influences the rate-dependent component. Note that the adjustment of salt concentration was needed to keep the hysteresis centred within the temperature window for different particle diameters. It was found that the increase in the diameter by 1 nm required the decrease of salt concentration by a factor of 0.89 (Figure 2.6.2).

To determine the change of rate-independent hysteresis with increasing diameter of nanoparticles the temperature difference (ΔT) were plotted at the middle height of

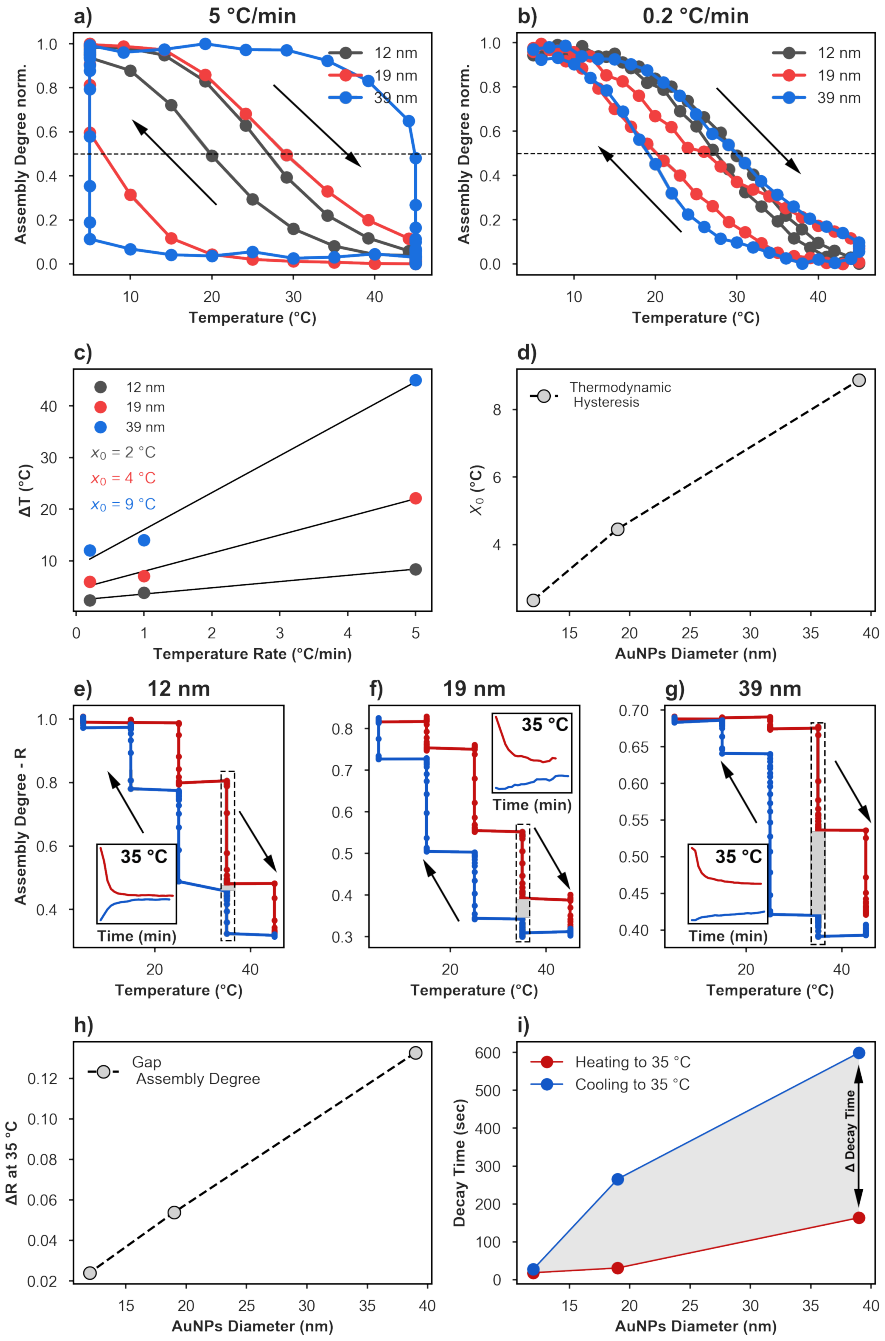

Figure 2.2.10: Effect of AuNPs size on rate-dependent and rate independent hysteresis. a-b) Hysteresis loop for 13, 19 and 39 nm AuNPs at a) 5 °C/min and b) 0.2 °C/min, where arrows indicate the direction of temperature scan. c) Temperature difference ΔT at middle height of hysteresis ($R = 0.5$, dashed line in a and b) versus velocity of temperature scan. The values of x_0 corresponds to the intercepts obtained by linear fit versus rate. d) The values of intercepts from c (ΔT at 0 °C/min) versus nanoparticle diameter. e-f) Stair-like hysteresis for different particle diameter with highlighted gaps at 35 °C - gray area in dotted rectangle. Insets: relaxation profiles at 35 °C after heating (red) and cooling (blue). h) Magnitude of gaps, $\Delta R = R_{heating} - R_{cooling}$, at 35 °C for different AuNPs sizes, extracted from plots e,f,g. i) Decay times versus AuNPs diameter for cooling and heating at 35 °C.

hysteresis (dashed line in Figure 2.2.10 a,b) versus the velocity of the temperature scan, as shown in Figure 2.2.10 c). The intercept, x_0, of linear fit corresponds to the temperature difference at infinitely small velocity of temperature scan, being thus the width of thermodynamic hysteresis. Figure 2.2.10 d) confirms that the width increases proportionally with the increase of nanoparticles diameter.

Likewise, the stair-like hysteresis for each nanoparticle size showed that the gaps - the difference of assembly degree ΔR - increase with diameter of nanoparticles (Figures 2.2.10 e - g, 2.6.4, 2.6.5). It is especially visible for the relaxation at 35 °C - a grey area in dotted rectangles in Figure 2.2.10 c-e). The ΔR follows a nearly linear trend with increasing nanoparticles diameter, indicating that the rate-independent component becomes prominent with increasing the size of nanoparticles (Figure 2.2.10 h). The analysis of relaxation profiles at 35 °C shows that the decay times at cooling are higher than decay times at heating as the diameter of nanoparticles increases (Figure 2.2.10 i). These data indicate that the larger the particles are, the larger the difference between clustering and assembly temperatures, leading to more pronounced rate-independent component of the hysteresis.

2.2.4 Surface potential broadens hysteresis

Neutralization of surface potential has greater impact on the hysteresis. It is well known, that native surfactants comprising quaternary ammonium ions (CTA^+) and halides counterions (*e.g.,* Cl^-) form a stable bilayer on the surface of metallic nanoparticles.[105, 106] Although the surfactant bilayers ensure excellent colloidal stability to the nanoparticles, they hinder the ligand exchange even of thiol-terminated molecules.[107–109] In the experiments discussed above, citrate was deliberately selected as good leaving ligands to ensure their efficient replacement with phosphine-bearing BSPP and upon ligand exchange the negative value of ζ-potential is conserved (Figure 2.2.11 a). This is quite the opposite scenario when replacing a cationic surfactant, such as cetyltrimethylammonium chloride (CTAC), with BSPP, where the sign of ζ-potential is reverted from positive to negative. Since the affinity of BSPP to the gold surface is lower than that of thiolated ligands, it is reasonable to assume that BSPP is unable to replace completely the native CTAC molecules, however, they are capable of reversing the sign of ζ-potential (Figure 2.2.11 a). Thus, the presence of residual surfactant molecules mixes surface charge, resulting in a less negative ζ-potential (-18 mV) as compared with -41 mV of Au@BSPP in which citrate is the starting ligand.

Cyclic clustering of BSPP-stabilized nanoparticles (9 nm) was performed using citrate and CTAC as the starting ligands, hereafter named as $AuNP^-$ and $AuNP^\pm$, respectively. Figure 2.2.11 b) shows that $AuNP^\pm$ feature much broader hysteresis

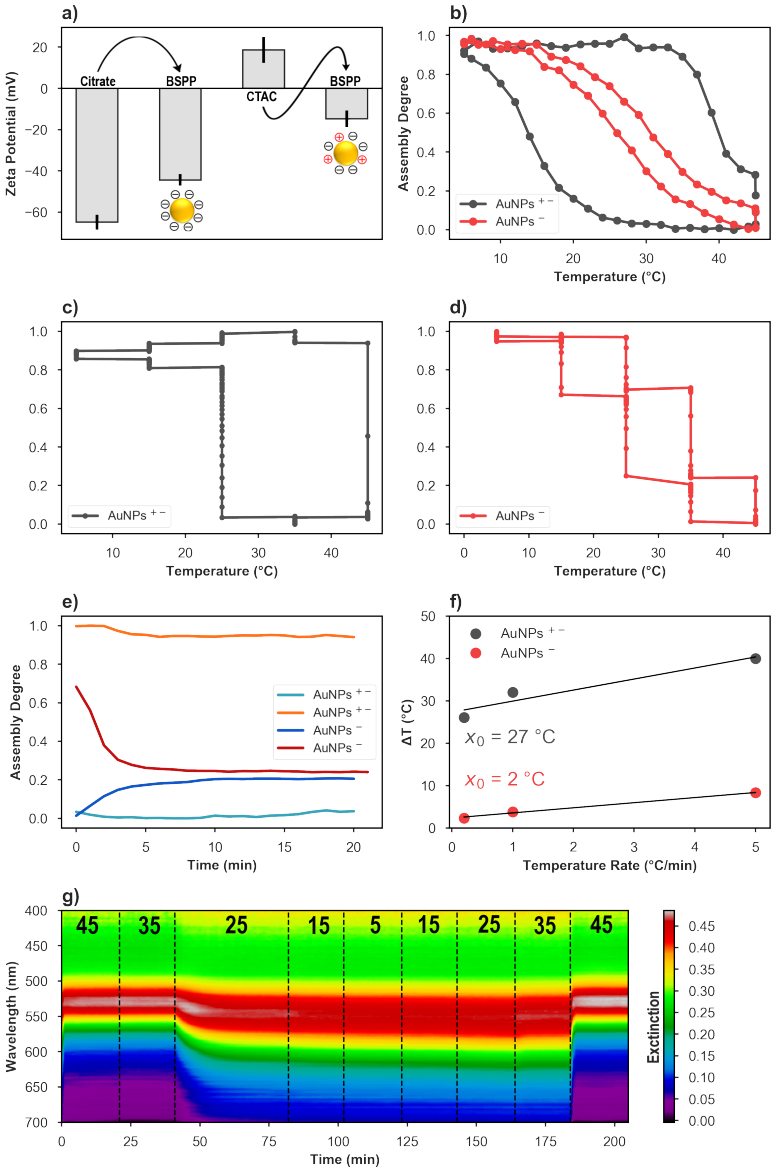

Figure 2.2.11: Influence of surface potential of AuNPs on rate-independent hysteresis.a) The difference in surface ζ-potential of nanoparticles before and after ligand exchange using citrate or cethyl trimethyl ammonium chloride (CTAC) as starting stabilizers. b) Hysteresis loops for AuNPs with mixed charges (AuNP$^{\pm}$) and AuNPs with negative charges (AuNP^{-}) at 0.2 °C/min. c,d) Stair-like hysteresis for AuNP$^{\pm}$ (c) and for AuNP^{-} (d). e) Change of assembly degree upon relaxation to target temperature of 35 °C for both types of AuNPs, showing invariance of assembly degree in AuNP$^{\pm}$ and fast decay for AuNP^{-}. f) ΔT at $R = 0.5$ for different temperature rates. The black line visualizes that AuNP$^{\pm}$ show weak response to increasing temperature rate, but highly increased thermodynamic hysteresis for x = 0 °C/min. g) Time-dependent spectral changed of AuNP$^{\pm}$ from c, showing slow change of assembly degree upon cooling to 25 °C and burst-like disassembly to 45 °C.

than AuNPs^{-} at 0.2 °C/min. At 35°C, the gap in stair-like hysteresis for AuNP$^{\pm}$ was much larger than for AuNP^{-} (Figure 2.2.11 c,d), 2.6.6). In fact, it remained fully open. Relaxation dynamics to this temperature shows that for AuNP$^{\pm}$ the

assembly degree remains practically invariant over 20 minutes while for $AuNP^-$ it relaxed to produce a small gap (Figure 2.2.11 e). The width of rate-independent hysteresis (ΔT at 0 °C/min) was estimated to be $\sim$ 27 °C for $AuNP^{\pm}$ (Figure 2.2.11 f) while for $AuNP^-$ it was $\sim$ 2 °C (Figure 2.2.11 f). These results confirm that thermodynamic hysteresis is greatly increased with neutralizing surface potential.
To show that disassembly temperature is higher than clustering temperature the aggregation rate during cooling to 25 °C and redispersion rate during heating to 45 °C for $AuNP^{\pm}$ were compared. The clustering took 50 minutes to complete, redispersion less than a minute (Figure 2.2.11 g). Probably, particles with mixes surface charges exhibit better colloidal stability at 25 °C than nanoparticles with negative charges, slowing the kinetics of clustering upon cooling. To induce redispersion through electrostatic repulsion at 45 °C a larger energy input is required since these nanoparticles bears lower amount of temperature-sensitive molecules (BSPP), thereby leading to greater hysteresis. Further, eventual interactions of the nanoparticles with the agarose matrix can occur that can additionally alter the hysteresis. The cationic surfactant molecules can bind to negatively-charged agarose that can additionally increase the temperature difference of clustering and redispersion.

2.3 Conclusions

In summary, experimental parameters were defined to control the hysteretic behaviour in temperature-driven reversible clustering of gold nanoparticles. It was shown that ionic strength, controlled by salt and ligand concentrations, modulates the centre of the hysteresis within a temperature range from 5 to 45 °C. The rate of heating or cooling altered its magnitude suggesting that assemblies remain under a kinetic regime (rate-dependent hysteresis). Both the asymmetric relaxation profiles of assembly degree at fixed temperature and the intercept of temperature scan velocity at fixed assembly degree defined the value of rate-independent hysteresis for given experimental parameter - diameter of nanoparticles and their surface potential. From a broader perspective, the simplicity of this method for estimation of kinetic and thermodynamics hysteresis can be applied to any system (molecular, colloidal, supramolecular) undergoing phase transition upon the action of a stimulus.

2.4 Methods and Materials

2.4.1 Materials

Sodium citrate, sodium chloride, bis(p-sulfonatophenyl)-phenylphosphine, triphenylphosphine-3,3',3"-trisulfonic acid trisodium salt, agarose and tetrachloroauric(III) acid were

purchased from Sigma-Aldrich and used without any further purification. All glassware was cleaned with aqua regia and rinsed thouroughly with Milli-Q water.

2.5 Characterization

Influence of NaCl concentration on the temperature dependent AuNP@BSPP aggregation (Figure 2) was characterized using a MayaPro 2000 (Ocean Optics) equipped with a tungsten/halogen light source. The cuvette was mounted in CUV-ALL-UV cuvette holder (Ocean Optics) and connected via 400 μm optical fibers to the light source and the spectrometer. The temperature of the cuvette holder was controlled by an external thermostat and recorded with a temperature logger equipped with thermocouple (Thorlabs) placed inside the cuvette. All other optical experiments were carried out using a Zeiss Axio Scope A1 microscope with an integrated temperature control stage (Linkam Scientific Instruments, LTS420E Series) and a tungsten/halogen light source. The microscope was connected to a Flame UV-VIS spectrometer (Ocean Optics) with a 400 μm optical fiber. Transmission electron microscopy (TEM) images were collected with Titan 60-300 TEM/STEM (FEI Company) operating at 300 kV. The hydrodynamic radius was acquired by Dynamic light scattering (DLS) measurement using Zetasizer Nano ZS (Malvern analytical).

2.5.1 Synthesis of 13 nm AuNPs@BSPP

Nanoparticles were synthesized using the reversed Turkevich method for citrate capped AuNPs.[35] In a typical synthesis, to boiling solution of sodium citrate (50 mg in 100 mL) was added a solution of $HAuCl_4$ (29.83 mM, 1.68 mL) under magnetic stirring. Once the solution turned ruby red, it was cooled to room temperature. Afterwards, a solution of BSPP (0.5 mL, 78.4 mM) was added and under mild magnetic stirring and left overnight. The solution was centrifuged twice (6500 rpm, 1 h) and stored at 5 °C. The final concentration of gold was 312 mM. Note that stock solution without extra salt remains stable at 5 °C.

2.5.2 Synthesis of 9 nm AuNPs@BSPP using citrate as native stabilizer

Nanoparticles were synthesized using the seeded growth method for sub-10 nm AuNPs[110]. Gold seeds of 3.5 nm in diameter were formed by injection of $HAuCl_4$ (1 mL of 25 mM) into solution of sodium citrate (150 mL of 2.2 mM) containing of tannic acid (0.1 mL) K_2CO_3 (0.1 mL) at 70 °C. After 5 minutes, 55 mL of the reaction solution were replaced with 55 mL of fresh portion of sodium citrate solu-

tion (2.2 mM). Once the temperature of solution stabilized at 70 °C, two subsequent aliquots of $HAuCl_4$ (0.5 mL 25 mM) were injected with an interval of 10 minutes. This process was repeated until AuNPs reached the desired size. To funcionalize AuNPs@Citrate with BSPP to the as-prepared solution of AuNPs@Citrate (100 mL) was added BSPP (0.5 mL, 78.4 mM) under mild stirring and was left stirring overnight, followed by two-step centrifugation (9000 rpm, 1 h) and redispersed with Milli-Q water.

2.5.3 Synthesis of 9 nm AuNPs@BSPP using CTAC as native stabilizer

Nanoparticles were synthesized following the protocol by Yoon [111]. To prepare seeds nanoparticles, the solution of $HAuCl_4$ (0.25 mL of 10 mM) was added to the solution of CTAB (10 mL of 100 mM) and left stirring until total complexation of gold salt with surfactant micelles. Next, the solution of ice-cold $NaBH_4$ (600 μL, 10 mM) was injected under strong stirring. The solution was aged for 1 h. To overgrowth gold seeds to desire size, a solution of ascorbic acid (15 mL, 100 mM) was added to CTAC solution (20 mL of 200 mM) containing Au seeds (500 μL), followed by injection of $HAuCl_4$ solution (20 mL 0.5 mM) and stirred vigorously for 10 minutes. The as synthesized AuNPs@CTAC were washed thrice by centrifugation (14000 rpm, 1 h) and redispersed with CTAC solution (2 mM). At the last centrifugation, the pellet was dissolved in BSPP solution (20 mL, 2 mM) and left stirring overnight. Finally, the solution of AuNPs@BSPP was purified twice by centrifugation (9000 rpm, 1 h) and redispersed in BSPP (1 mM).

2.5.4 Synthesis of larger AuNPs@BSPP - 19, 39 nm

Nanoparticles were synthesized using the seeded growth method for AuNPs@Citrate by Bastus [40]. A solution of $HAuCl_4$ (1 mL of 25 mM) was added to the solution of sodium citrate (150 mL of 2.2 mM) at 100 °C under strong stirring. The solution was then cooled down to 90 °C followed by the addition of $HAuCl_4$ (1 mL of 25 mM). After 30 minutes the reaction was finished. Afterwards, 55 mL of the reaction solution were replaced by the solution of sodium citrate (55 mL 2.2 mM) and was used as seed solution.

2.5.5 Preparation of Au-agarose composite

To the aqueous solution containing AuNPs@BSPP (200 μl, 25 mM) was added a solution of BSPP (100 μL, 74.8 mM), followed by the addition of hot agarose (2 mL, 0.25 wt%, 90 °C) and NaCl (200 μL, 1 M). The mixture was left undisturbed for 2

hours before use. The sample was either prepared directly inside a cuvette or transferred instantly into one after mixing and sealed. To ensure good reproducibility the agarose solution should be sufficiently hot. To minimize the evaporation of water in hot agarose solution, a solution of 10 mL was prepared in a 20 mL flask with the lid laid reversed on the orifice. The dispersion was microwaved until the first boiling was observed and stopped instantly followed by thorough mixing and the second microwave heating until the very first moment of boiling. To study the effect of BSPP and NaCl concentrations the volumes of both chemicals were kept constant while the concentration of stock solutions were accordingly adjusted. The solution containing AuNPs@Citrate were transferred to a cuvette containing and sealed to prevent evaporation, which otherwise would alter the concentration of agarose.

2.5.6 Temperature-dependent clustering

All experiments were carried out with AuNPs embedded in an agarose matrix. Temperature-induce reversible aggregation of nanoparticles commenced with an isotherm at 45 °C for 15 minutes to ensure that AuNPs remain dispersed. The sample was cooled at give rate (0.2, 1 or 5 °C/min) with an isotherm (15 min) at 5 °C followed by heating to 45 °C at similar rate and isotherm for 15 minutes. For the stair-like hysteresis, the temperature was changed by 10 °/min followed by an isotherm for 15 minutes between 45 °C and 5 °C. In all experiments, temperature values and UV-Vis spectra were recorded in the interval of 10 seconds. Open source Python libraries (Pandas, Numpy, Scipy, Matplotlib) were used for automated spectral data analysis.

2.6 Appendix

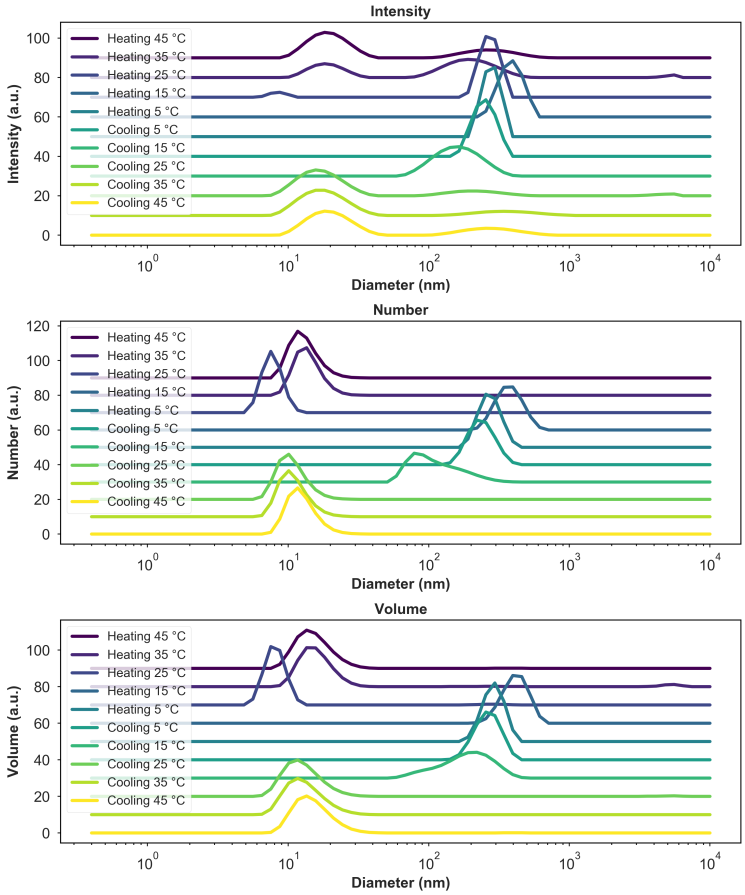

Figure 2.6.1: Change of hydrodynamic diameter of AuNPs@BSPP (NaCl: 80 mM; BSPP: 3 mM) upon cooling and heating. The change of hydrodynamic diameter at different temperatures is similar regardless the representation: intensity (upper), number (middle) and volume (lower) distribution

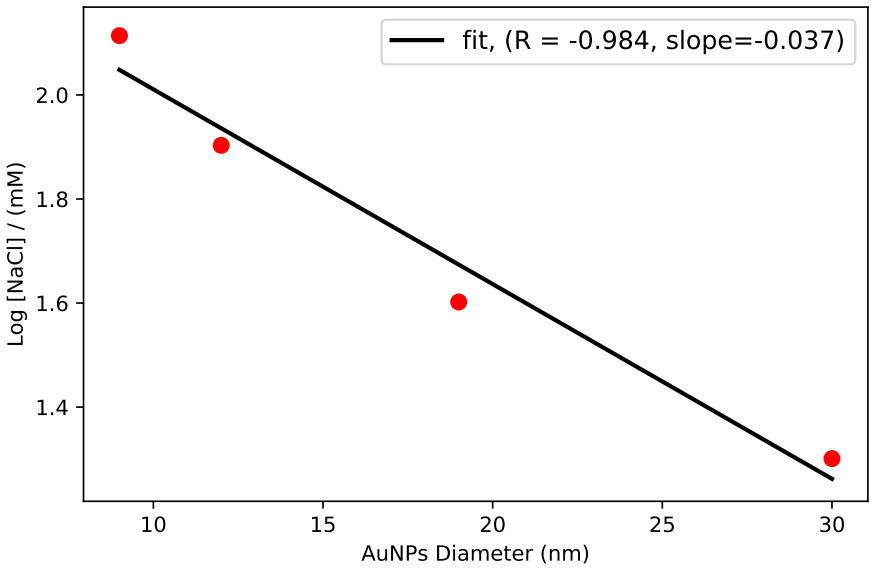

Figure 2.6.2: Semilog plot of NaCl concentration versus nanoparticle diameter at hysteresis centered in temperature window. (Note that for each nanoparticle diameter salt concentration was readjusted to center the hysteres). The fitting indicates that with the increase nanoparticle diameter by 1 nm the salt concentration need to be lowered by factor of 0.89.

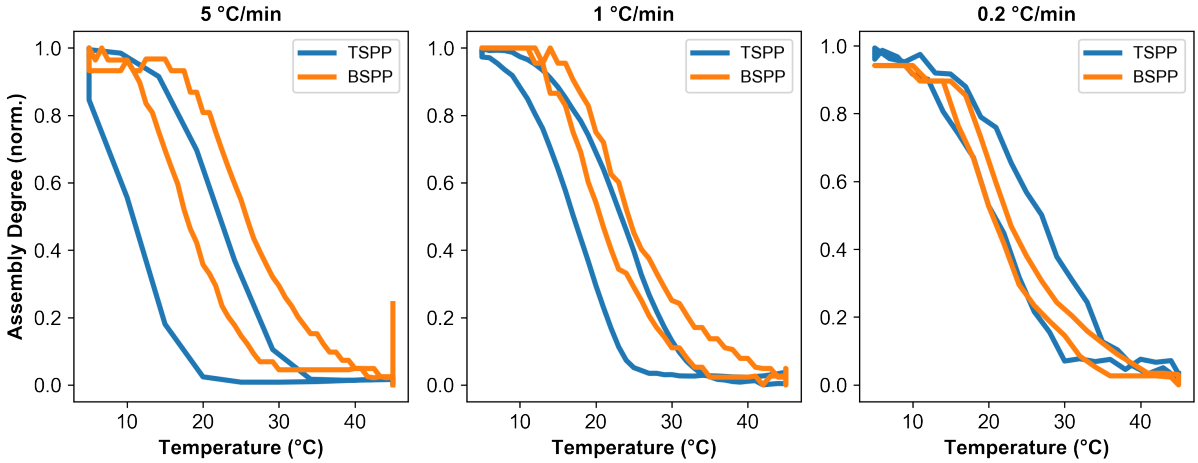

Figure 2.6.3: Comparison of AuNPs@BSPP (two sulfonate units) vs. AuNPs@TSPP, three sulfontate units).

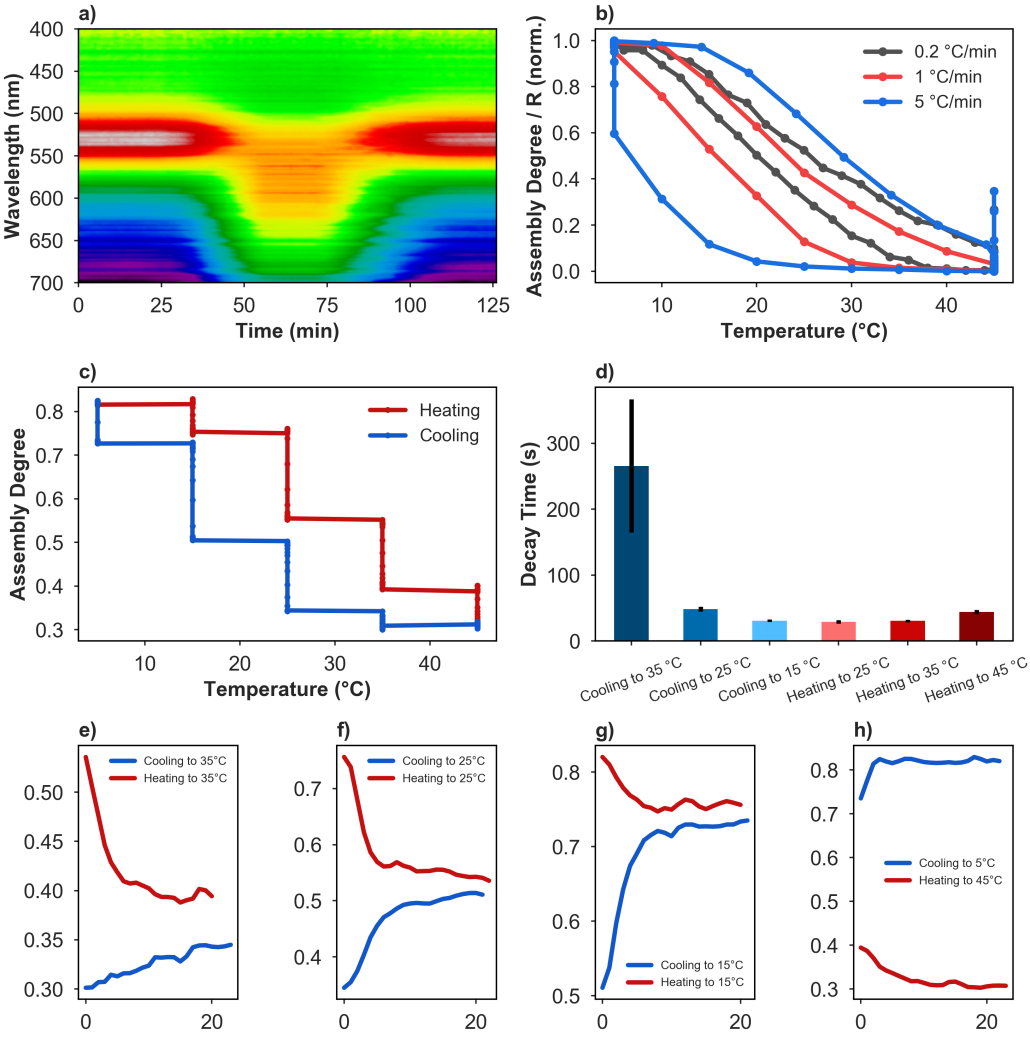

Figure 2.6.4: Summary of 19 nm AuNPs@BSPP. a) Time-dependent spectral evolution for 19 nm AuNPs@BSPP at 1 °C/min of scan rate. b) Assembly Degree, R, for three different temperature scan rates. c) Response of Assembly Degree R to a stair-like hysteresis. See Figure 3 in main text for details. d) Decay time constants for aggregation and redispersion at different temperatures calculated from e-h. e -h) The relaxation of R to given temperature for clustering and dissagregation obtained from stair like hysteresis (vertical lines in c).

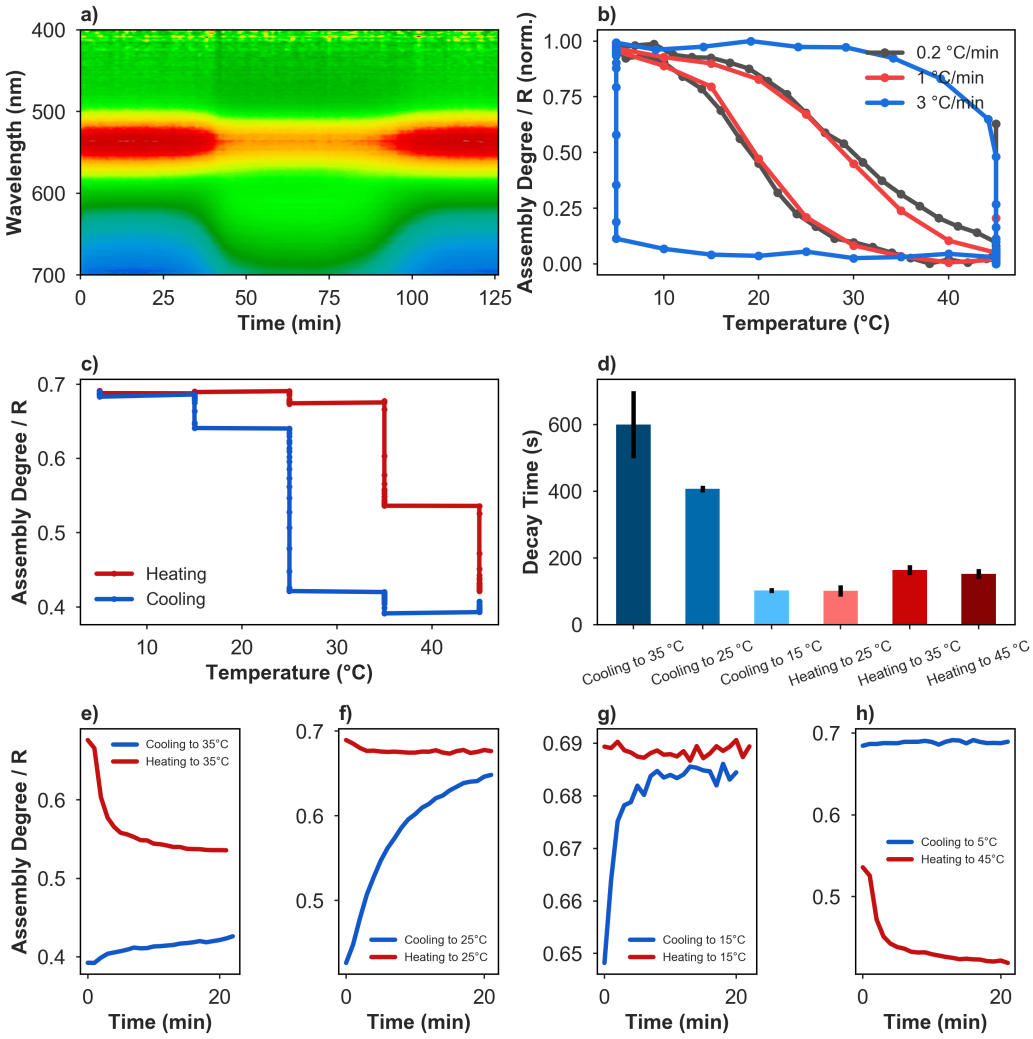

Figure 2.6.5: Summary of 39 nm AuNPs@BSPP. a) Time-dependent spectral evolution for 39 nm AuNPs@BSPP at 1 °C/min of scan rate. b) Assembly Degree R for three different temperature scan rates. c) Response of Assembly Degree R to a stair-like hysteresis. See Figure 3 in main text for details. d) Decay time constants for aggregation and redispersion at different temperatures calculated from e-h. e- h) The relaxation of R to given temperature for clustering and dissagregation obtained from stair like hysteresis (vertical lines in c).

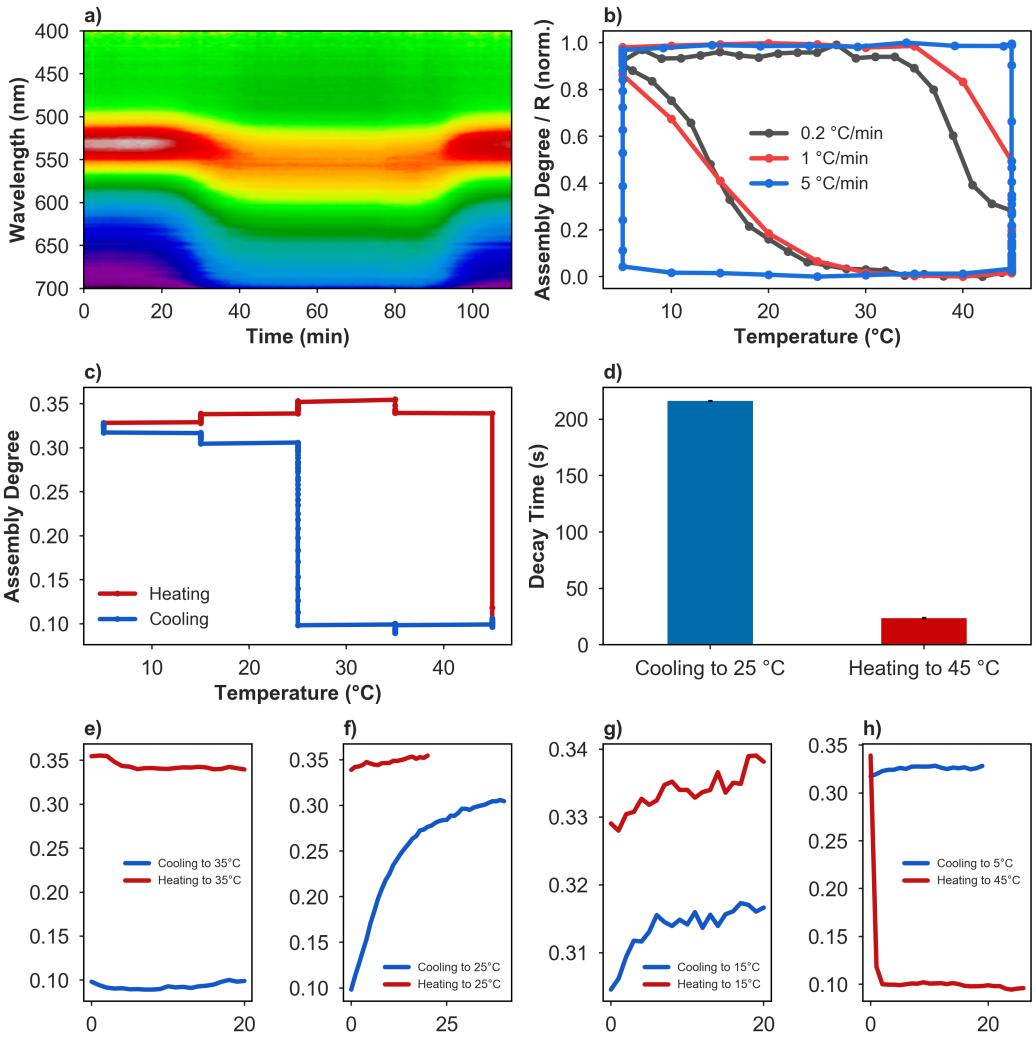

Figure 2.6.6: Summary of AuNPs@CTAC. a) Time-dependent spectral evolution for AuNPs^{+-} at 1 °C/min of scan rate. b) Assembly Degree R for three different temperature scan rates. c) Response of Assembly Degree R to a stair-like hysteresis. d) Decay time constants for aggregation at 25 °C and redispersion at 45 °C. The aggregation is about 8x slower. e - h) The relaxation of R to given temperature for clustering and dissagregation obtained from stair like hysteresis (vertical lines in c).

CHAPTER 3

Thermoresponsive Gold Nanorods

3.1 Introduction

The outcome of the previous chapter raises a question whether one can modulate reversible clustering (and hysteresis) of anisotropic nanoparticles at different temperatures using BSPP molecules as surface ligand. As already shown in the introduction section (section 1.3), the role of shape anisotropy of self-assembling building blocks offers additional optical features since the shape anisotropy leads to the reduction of degree of freedom, rendering different mutual orientations between the nanoparticles in clustered state. For example, in the case of gold nanorods, two orientations can be achieved, namely side-to-side and tip-to-tip, leading to drastically different optical response [20].

While the temperature-driven reversible clustering of spherical nanoparticles has been widely explored (subsection 1.6.1) the clustering of non-spherical particles using temperature as stimulus remains poorly studied. Table 3.1 lists the published works devoted to the reversible clustering of non-spherical nanoparticles. For example, Iida et al.[60, 63] have used gold nanorods functionalized with an hexaethyleneglycol derivative showing that surface ligand located on lateral parts or tips underwent dehydration at different temperatures leading to two-step clustering from side-to-side to tip-to-tip. In another example, the combination of thermoresponsive polymer (p-NIPAM [112, 113]) or alkanethiol ((1-mercaptoundec-11-yl)hexa(ethylene glycol) (MUDOL) [114]) allowed for clustering of gold nanorods at different temperatures. Nanoparticles coated with polyethylene glycol (PEG) have also shown thermoresponsive behavior as ordering into superlattices at elevated temperatures [115].

A detailed inspection of works available in the literature indicates that reversible clustering of anisotropic nanoparticles driven by temperature requires the presence of polymers on metal surface. Such bulky surface ligands, however, occupy much space in between the nanoparticles in the clustered state, compromising the extent of the enhancement of near electric field through the formation of hot spots. Therefore,

Ligand	Shape	Temperature	Ref.
DNA	Disk	50°C	[59]
DNA	Rod	60°C	[116]
HEG	Disk	50 - 70 °C	[117]
HEG	Rod	10 - 60 °C	[60]
PEG	Rod	50 °C	[115]
p-NIPAM	Rod	34 °C	[112]
MUDOL	Rod	120 °C	[114]

Table 3.1: Reported systems on temperature-induced reversible clustering of anisotropic nanoparticles. MUDOL - (1-mercaptoundec-11-yl)hexa(ethyleneglycol); p-NIPAM - Poly(N-isopropylacrylamide); HEG - Hexaethylene glycol; PEG - Polyethylene glycol

the use of small molecules for the clustering of anisotropic nanoparticles (which normally are rather large) is needed to obtain nanosystems with pronounced change of optical properties upon the change of temperatures.

An additional conclusion one can draw from literature is that virtually all examples related to the clustering of anisotropic nanoparticles are based on the use of molecules anchored covalently to gold surface via strong S-Au bond (50 kcal/mol [118]). Although this bond prevents degradation of the system through the detachment of molecules from the surface, they inhibit the incorporation of co-ligands that are of interest in a variety of applications including biosensing or catalysis. Thus, new experimental examples for reversible clustering of anisotropic nanoparticles are required based on the interactions different from that of S-Au.

The present chapter aims to solve these issues and seeks to develop a thermosensitive system based on gold nanorods. In particular, BSPP molecules together with native surfactant (CTAB) are proposed as convenient surface ligands to tailor the reversible clustering of nanorods. Note however that BSPP molecules has only been employed as auxiliary surface ligand to obtain biocompatible nanorods[119], but have never been reported as ligand for thermoresponsive properties. At the first place, a general methodology is proposed for thermoresponsive colloidal solution of gold nanorods. Then, a comprehensive thermal analysis is performed to give a quantitative description of the hysteretic behavior of reversibly clustering nanoparticles. Finally, a mechanism is proposed explaining the role of each molecule in the reversible clustering. The results presented in this chapter show a first experimental model for reversible clustering of anisotropic nanoparticles using BSPP as main surface ligand.

3.2 Results and Discussion

3.2.1 Synthesis and functionalization of gold nanorods

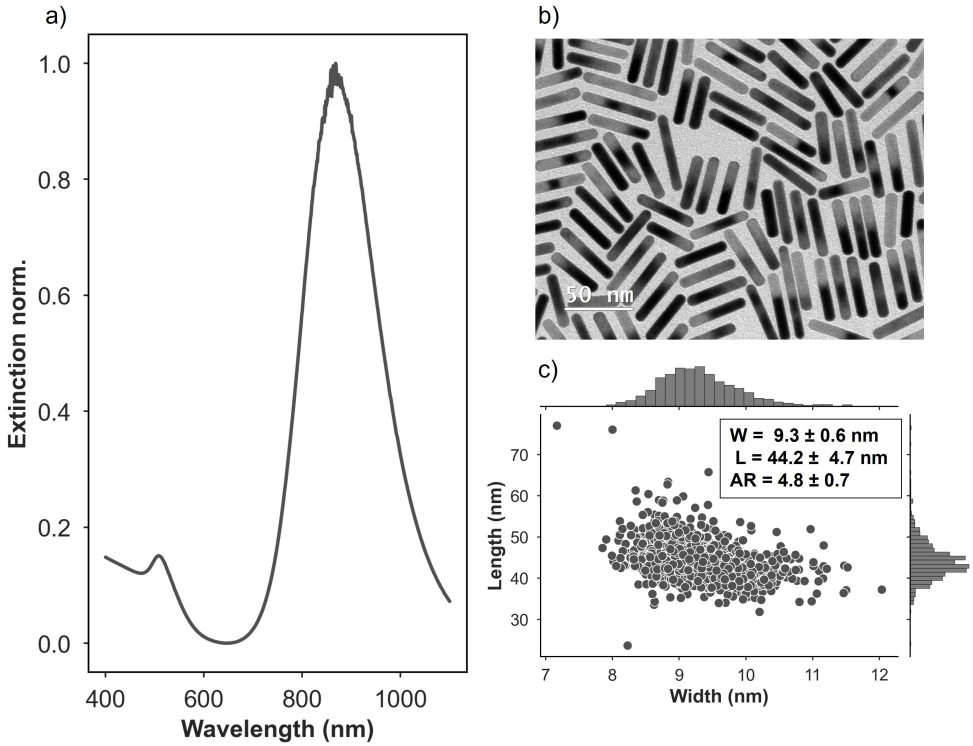

Figure 3.2.1: a) UV-Vis spectra of AuNRs. b) TEM image of synthesized AuNRs at 60k magnification. c) Size analysis of AuNRs based on TEM images.

Gold nanorods were synthesised by following the protocol of Murphy et al.[120]. Figure 3.2.1 a) shows typical extinction spectrum of as-prepared gold nanorods with maximum of the longitudinal LSPR located at 889 nm. An intense plasmon band located at NIR spectral range is sensitive to the mutual orientation of nanoparticles in aggregated state, rendering them a convenient system to study reversible clustering. The length (44.2 ± 4.7 nm) and the width (9.3 ± 0.6 nm) of nanorods were estimated by TEM analysis and subsequent images analysis (Figure 3.2.1 b - c) of ∼1000 particle using Biovoxxel plugin in ImageJ software. The aspect ratio of nanorods was 4.8 ± 0.7 (Figure 3.2.1 b - c).

To remove by-products remaining in the solution of as-synthesized nanorods three cycles of centrifugation (14000 rpm, 30 minutes) were implemented giving a concentrated stock solution of nanorods (25 mM) in CTAB (1 mM). The ligand exchange process comprised two steps (Figure 3.2.2 a). In a first step, stock solution (50 μL) was diluted in ligand exchange solution (5mL, BSPP/CTAB) at 50 °C and under sonication (Figure 3.2.2 a), left). The solution was left undisturbed for 16 hours to allow maximal BSPP incorporation on metal surface. In a second step, the solution

was centrifuged (11000 rpm, 30 minutes) and redispersed in freshly prepared ligand-exchange solution (5 mL, BSPP/CTAB), again, under sonication at 50 °C for 10 minutes (Figure 3.2.2 a), right). In analogy to the two-step ligand exchange proposed previously for pegylation of nanorods[121] it was observed, that double treatment favors the attachment of BSPP on the nanoparticle surface, rendering samples of reproducible thermoresponsive properties. Also the protocol gave additional control over adjusting CTAB concentrations in the final solution.

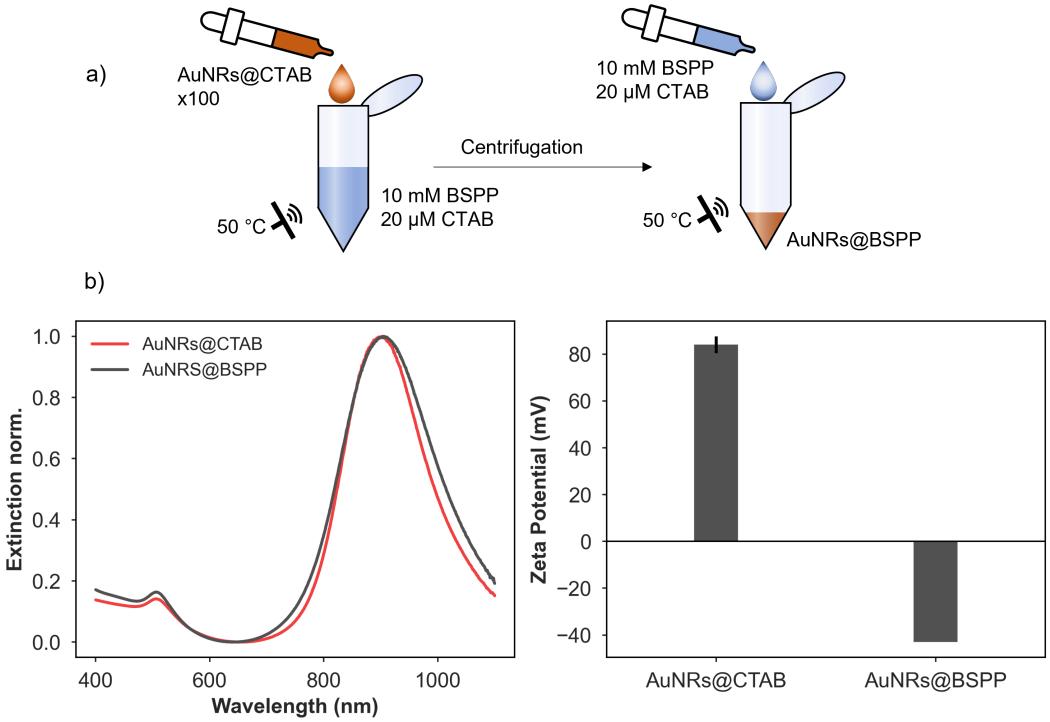

Figure 3.2.2: Surface functionalization of AuNRs@CTAB with BSPP. a) Schematics of two-step surface functionalization process. b) UV-Vis-NIR spectra of AuNRs before (CTAB) and after (BSPP) surface functionalization. c) ζ-potential measurements of AuNRs@CTAB and AuNRs@BSPP showing the inversion of surface charge.

Since BSPP is unable to act as a sole surface ligand there was a need to find optimal range of concentrations of BSPP and CTAB during ligand exchange to make nanorods colloidally stable and thermoresponsive. Thus, a coarse screening of concentrations for both molecules was executed in which the succesful ligand exchange was assesed by extinction spectra (see for example Figure Figure 3.2.2 b, left) or the inversion of ζ-potential from positive (+80 mV) to negative values (-40 mV) (see for example Figure Figure 3.2.2 b, right). In total, thirty six samples were prepared with different combinations of CTAB (0.1 - 1 mM) and BSPP (0 - 50 mM) (Figure 3.2.3). It was observed that when CTAB and BSPP concentration were similar nanorods aggregated spontanously due to charge neutralization (black squares in Figure 3.2.3 a and violet sample color in b). Thus the lower concentration limit for BSPP was set to 5 mM. At 50 mM BSPP and for all CTAB concentrations, AuNRs

aggregated irreversibly due to high ionic strength of the solution. At 20 mM BSPP, AuNRs were difficult to purify after centrifugation, because they easily formed pellet of aggregated AuNRs. Therefore, the optimal BSPP concentration was found to be 10 mM and was used in further screening.

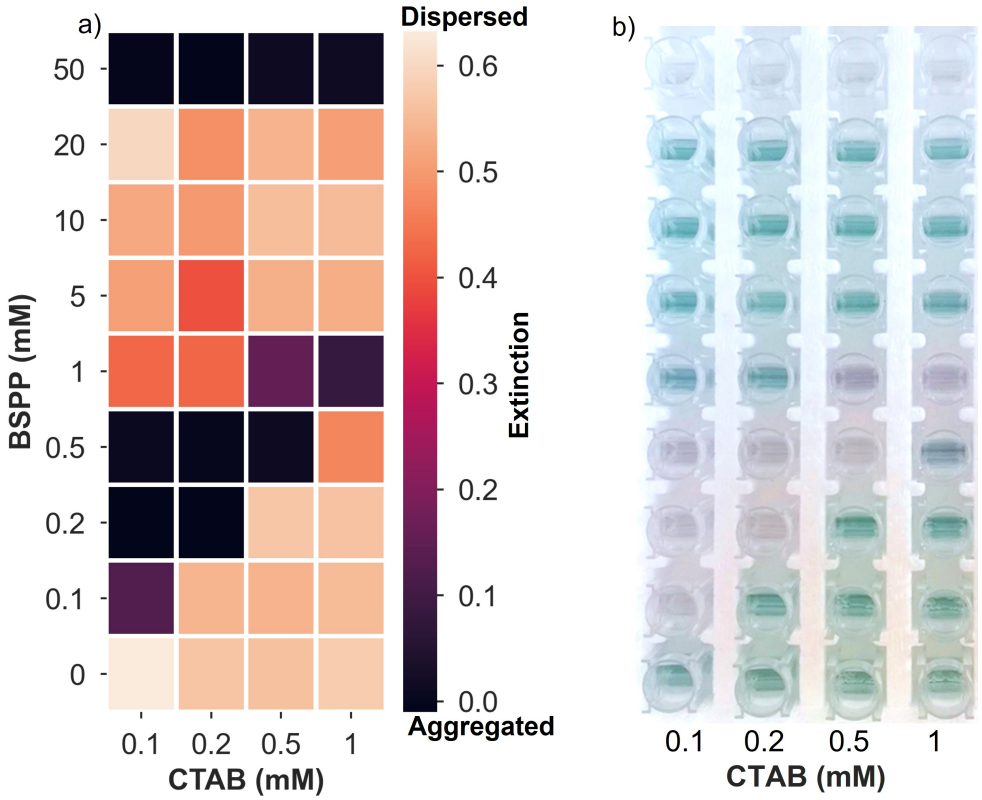

Figure 3.2.3: Coarse screening of BSPP and CTAB concentration during two-step surface functionalization of gold nanorods. a) Heatmap of parameter space with the extinction at longitudinal LSPR as measure for colloidal stability. b) Digital image of all samples from which the heat map in a) was obtained. Blue-dispersed nanoparticles, violet-aggregated.

Likewise spherical nanoparticles in the previous chapter, the thermoresponsive gold nanorods require the presence of an extra NaCl. To find the optimal conditions for thermoresponsive gold nanorods the concentration of BSPP was maintained constant (10 mM) and the concentration of CTAB was varied in the range of 0 - 1 mM and the concentration of NaCl in the range of 0-400 mM. In total 30 samples were prepared (Figure 3.2.4). The reason of setting the upper limit of CTAB at 1 mM was the need of avoiding micelles formation, as the critical micelle concentration for this surfactant is $\sim$ 0.9 mM[122].

UV-Vis-NIR spectroscopy was used to asses the thermoresponsive character of nanorods where three spectra were recorded at 50 °C, 5 °C and 50 °C after 20 minutes of incubation at given temperature. The change in UV-Vis-NIR spectra was evaluated and classified as one of four possible categories: Category 0 - irreversible clustering at low

temperature; Category 1 - reversible clustering but with minor sensitivity to temperature change; Category 2 - reversible clustering and with pronounced sensitivity to themperature change; Category 3 - absence of clustering (Figure 3.2.4).

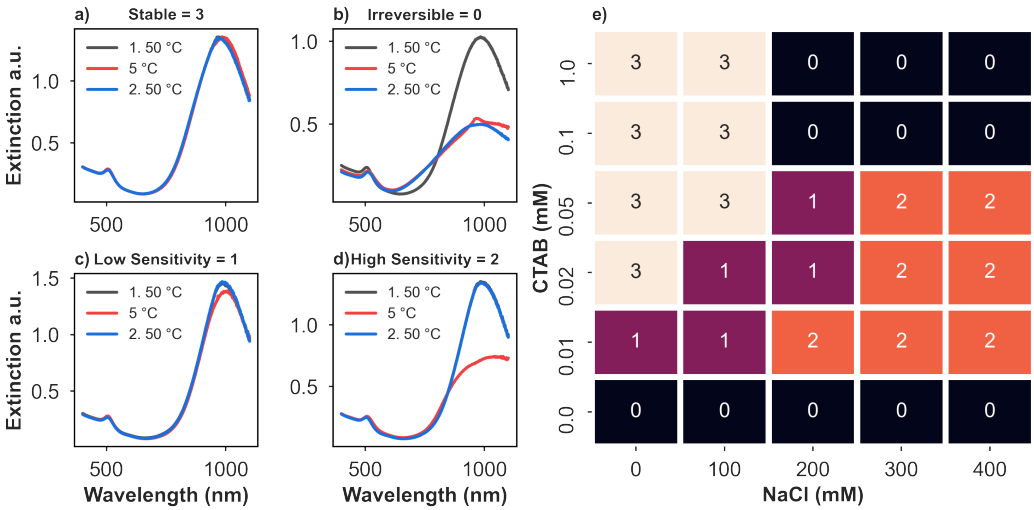

Figure 3.2.4: Experimental optimization of thermoresponsive nanorods. a) - d) four categories of thermoresponsive nanorods assesed by the extent of spectral change at low temperature and its recovery upon heating. e) Heatmap of the thermoresponsive gold nanorods solutions for different combinations of CTAB and NaCl concentrations. Category "2" shows optimized response.

With increasing NaCl and decreasing CTAB concentration, AuNRs resulted more responsive to the temperature change (Figure 3.2.4 e), orange tiles). In other words, CTAB and NaCl acted as antagonists: CTAB lowered the amount of clustering at a given temperature, while NaCl increased it. When CTAB concentration was 100 μM or higher, AuNRs were stable or aggregated irreversibly with 200 mM NaCl or more. Without CTAB, AuNRs immediately aggregated irreversibly independent on the concentration of NaCl. For CTAB concentrations between 10 μM and 50 μM, AuNRs showed increasing themorsensitivity with increasing NaCl concentration. While the role of NaCl is more obvious (destabilization of colloids through charge screening), the influence of CTAB on colloidal stability is not straightforward and will be discussed later in detail in subsection 3.2.4. To close, experiments allowed to define the optimal concentrations for CTAB, BSPP and NaCl which are 20 μM, 10 mM and 300 mM, respectively and will be used in the following experiments.

3.2.2 Thermoresponsive properties of AuNRs coated with BSPP

The colloidal dispersion of gold nanorods undergo clustering below 25 °C and fully recover its stability at 50 °C. The reversible clustering alters optical properties of the solution, as confirmed by the change of the intensity of the longitudinal LSPR (Figure 3.2.5 a).

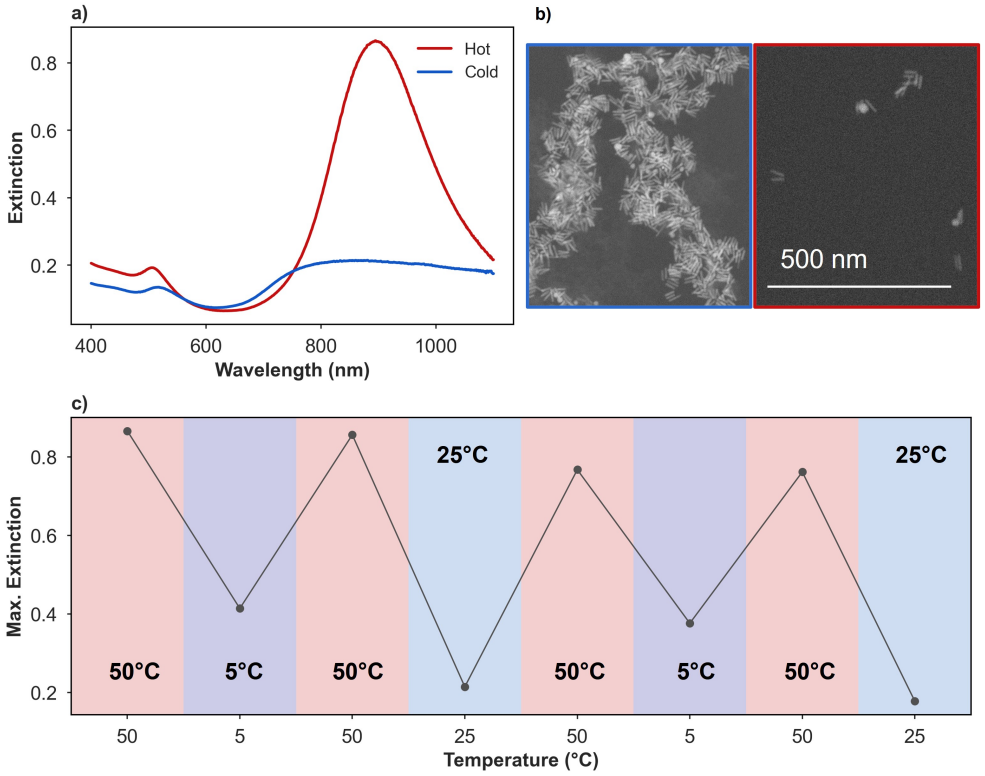

Figure 3.2.5: Overview of thermoresponsive properties of AuNRs@BSPP. a) UV-Vis-NIR spectra of AuNRs@BSPP at high (red) and low (blue) temperatures. b) Representative SEM spectra of aggregated (blue) and dispersed (red) AuNRs taken from the same sample at 5 °C and 50 °C, respectively. c) Maximal extinction of AuNRs@BSPP for different temperatures showing the reversible aggregation. Maximal extinction drops when AuNRs are being cooled and initial signal intensities are recovered upon heating to 50 °C.

The clustering of nanorods at low temperature was also confirmed by Scanning Electron Microscopy (SEM) analysis, showing dispersed particles at 50 °C and large aggregates of randomly distributed nanoparticles below room temperature (Figure 3.2.5 b).

To demonstrate reversible clustering of AuNRs@BSPP, the extinction value 889 nm was recorded at 50 °C, 25 °C and 5 °C after maintaining temperature for 30 minutes (Figure 3.2.5 c). Between lowering the temperature to 25 °C or 5 °C, initial values of dispersed AuNRs were recovered at 50 °C for at least four cycles. These data show that nanoparticles responds to the temperature change.

Note that the reversible clustering of AuNRs was assessed optically by monitoring the change of intensity of longitudinal LSPR. It was found that using a ratio between two wavelengths (as shown in the previous chapter for spherical nanoparticles) was not feasible because in contrast to isotropic gold nanospheres, the mutual orientation of gold nanorods can lead to either red- or blue-shift depending on particle-to-particle orientation (see Figure 1.3.2), and may lead to incoherent data interpretation.

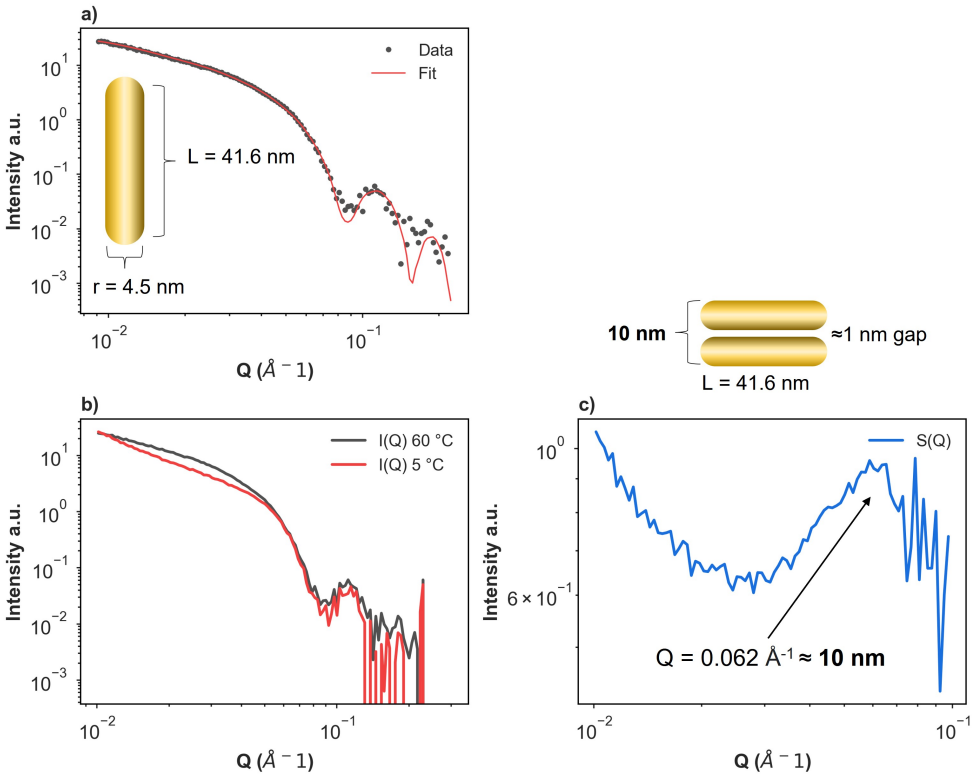

Figure 3.2.6: SAXS data for thermoresponsive AuNRs@BSPP. a) Form factor of AuNRs with fitting function for cylinder shaped colloids. b) Form factor of AuNRs at 60 °C and 5 °C and resulting structure factor in c) showing an interparticle distance of ∼ 10 nm, which is in agreement with side-to-side assembly of AuNRs.

The Small Angle X-Ray Scattering (SAXS) analysis of colloidally stable nanorods solution (no salt) confirmed that the dimension (41.6 nm x 9 nm) corresponds to the values obtained by TEM (Figure 3.2.6 a). The advantage of using SAXS analysis is the insight on the interparticle distance at aggregated state at low temperature. Thus, the spectra were recorded at 60 °C and 5 °C from which structure factor was calculated (Figure 3.2.6 b), resulting in a maximum at Q = 0.062 $Å^{-1}$, corresponding to an inter-particle distance of ∼ 10 nm (Figure 3.2.6 c). Such a distance indicates the presence of side-to-side orientations with interparticle distance of 1 nm. Although DLS and SEM analysis indicate that nanoparticles should also cluster in tip-to-tip orientation, the SAXS analysis was unable to resolve it since the Q-range was not wide enough.

3.2.3 Kinetic analysis of dynamic assembly of AuNRs@BSPP

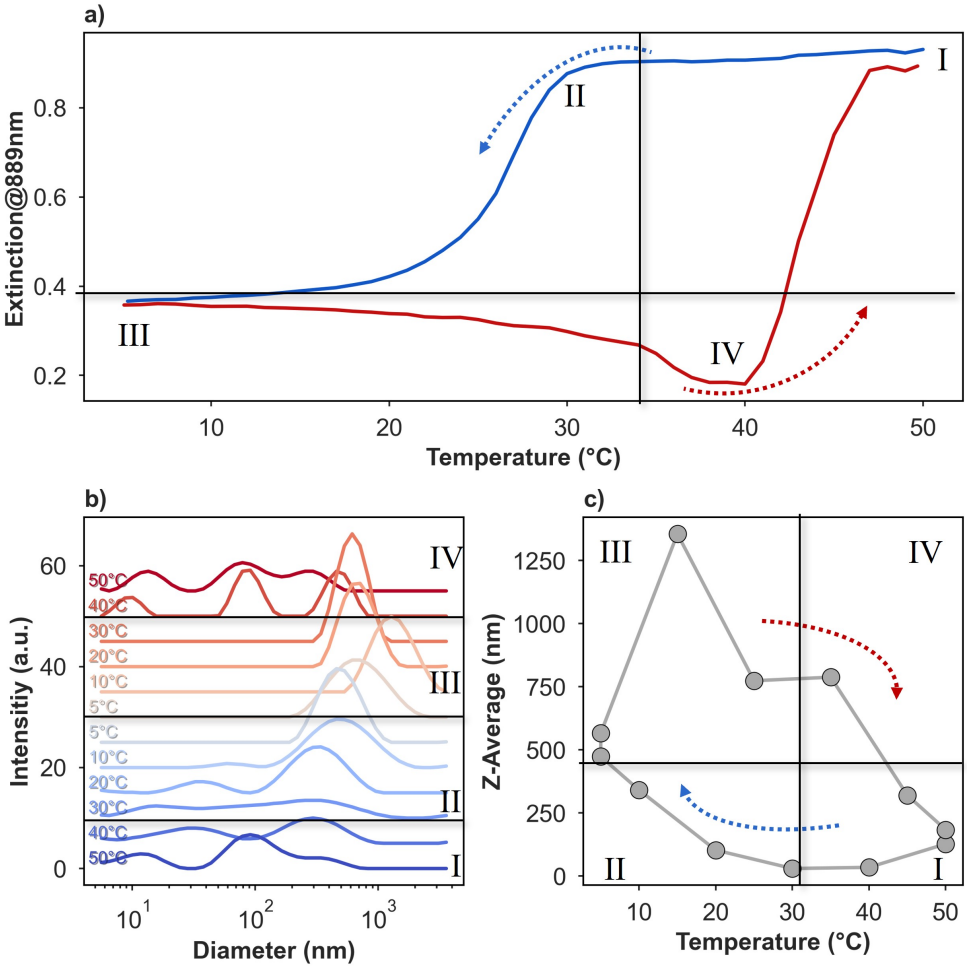

Figure 3.2.7: a) Thermal cycling of AuNRs between 50 °C and 5 °C at 0.2 °C/min as followed by the extinction measurement at 889 nm. b) Thermal cycling of AuNRs measured with DLS. First, bimodal distribution of dispersed AuNRs@BSPP at elevated temperatures that undergo isotropic aggregation at low temperatures and recovery of stable dispersion after rising the temperature again. c) Z-Average of AuNRs@BSPP calculated from intensity distribution in e) confirming the reversibility of the process.

Although above-described experiments confirmed the reversible clustering of nanorods, they lack the information on the eventual thermal hysteresis. Thus thermal cycling was performed between 50°C and 5 °C by tracking the wavelength at the maximum of longitudinal LSPR (Figure 3.2.7 a). The sample revealed a wide hysteresis, where four distinct phases (quadrant) were distinguished over the entire thermal cycle.

- Phase I - upon cooling from 50 °C the solution of nanorods remain dispersed since no change is observed in the maximum of LSPR.
- Phase II - further cooling causes a sudden drop in maximum of LSPR at 30°C that stabilizes at 5°C. At this stage the optical properties of the solution re-

main unchanged, that is, no further aggregation takes place while maintaining the temperature at 5 °C for 20 min. The solution remained undercooled.

- Phase III - upon heating from 5°C to 30°C particles experience further aggregation.
- Phase IV - further heating above 30°C leads to even more pronounced aggregation and then sudden redispersion and full recovery of the optical properties at 40°C.

The presence of relatively large hysteresis indicates similarities between the clustering of nanorods and the system from previous chapter which comprised spherical nanoparticles co-functionalized with surfactant and BSPP(Figure 2.2.11). Here, the composition of the sample is similar, the solution of gold nanorods contains both molecules - positive surfactant (CTA^+) and negatively charged BSPP - and both type of molecules can interact with metal surface, making feasible the scenario of co-functionalization and thus the origin of large hysteresis.
The shape of hysteresis depends on the shape of building blocks. In the previous chapter it was shown that thermal hysteresis of spherical nanoparticles is relatively symmetric at optimal salt concentration. Here, in the case of nanorods, the cooling and heating pathways show certain asymmetry (Figure 3.2.7 a). During the clustering, the anisotropic nanorods form isotropic aggregates (all probable mutual orientations between side-to-side and and tip-to-tip modes) that remain undercooled at 5°C (phase I and II). Then, during heating (phase III), the supplied thermal energy (up to 30 °C) can increase the mobility of nanoparticles allowing for further growth of the clusters. With further temperature increase the nanorods reorganize within the cluster making them more compact, thereby resulting in further drop of extinction at the maximum of LSPR. Note that the compactness of the clusters becomes more pronounced at the beginning of phase IV where a minimum of LSPR is reach just before redispersion (Figure 3.2.7 a). Such a thermally-induced organisation of nanoparticles has been reported by Korgel et al.[123], who used small gold nanocrystals of 2 nm coated with octadecanethiol. These nanoparticles assembled into an amorphous structures at room temperature, but upon rising the temperature above 55°C a compact superlattice formed. The phenomenon was explained by melting of the surface ligand and thus a softer corona that allows for better packing. The softer corona can deform, which compensates for facetted or polydisperse particles. In the present case, although the supercrystals are not observed, the rearrangement of anisotropic nanoparticles within cluster is a feasible mechanism behind the asymmetric shape of thermal hysteresis.
Temperature-dependent DLS measurement further confirmed the presence of reversible aggregation and hysteresis (Figure 3.2.5 b and c). At 50 °C two bands were

visible that corresponded to dispersed AuNRs [124]. Upon lowering the temperature below 50 °C, a monomodal band appeared. The presence of monomodal distribution indicates that anisotropic AuNRs form isotropic aggregates, which corroborate with results from TEM image analysis and optical analysis. After rising the temperature to 40 °C, bimodal distribution at low diameters was recovered.

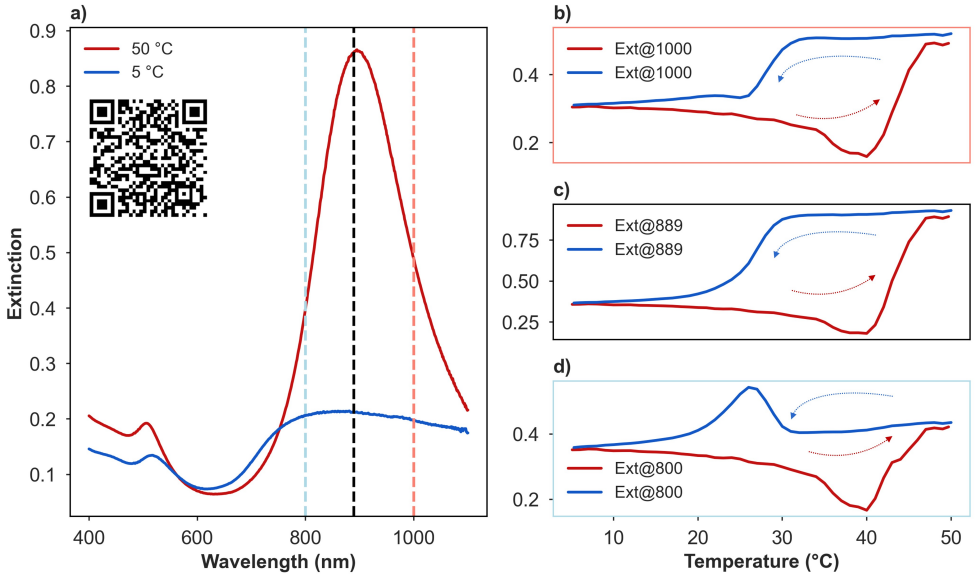

Figure 3.2.8: Optically-resolved mutual orientation of nanoparticles during clustering. a) UV-Vis-NIR spectra of nanorods at 50 and 5 °C, showing fully dispersed and aggregated nanoparticles (inset: QR for video showing temporal evolution of thermal hysteresis). b-d) Thermal hysteresis obtained from monitoring the extinction at three wavelengths: 800 nm (pale blue), 889 (black) and 1000 nm (orange). An increase of extinction at 800 nm during cooling (in d) indicates the presence of side-to-side nanorods arrangement within clusters. Experimental conditions: 20 μM CTAB, NaCl 300 mM.

The data obtained from DLS measurement were used to calculate intensity-weighted mean hydrodynamic diameter (Z-average) showing the change of the overall cluster diameter during thermal cycle (Figure 3.2.5 c). Again, thermal hysteresis showed a certain asymmetry. During the cooling from phase I to phase II, the cluster progressively increased their size up to 500 nm at 5 °C where remained stable. Upon heating, the size increased suddenly to 1300 nm, suggesting that undercooled structures at 5 °C underwent additional growth. Further heating led to progressive size decrease (cluster compactness) and eventual redispersion at 50 °C. Overall, the thermal hysteresis obtained by recording UV-Vis-NIR and DLS data allowed for detailed description of the dynamics of reversibly clustering gold nanorods.

In the previous section it was shown that SAXS analysis indicates the presence of side-to-side arrangement of gold nanorods during clustering. One could then ask whether optical analysis that was used to track thermal analysis could be used to provide an information on such orientation of nanoparticles during lowering the tem-

perature. It was already mentioned in the introduction section (Figure 1.3.2) that tip-to-tip interaction between gold nanorods leads to red-shift of LSPR whereas side-to-side interactions leads to blue-shift. Put differently, when side-to-side interaction dominates, the values of extinction at the wavelengths lower than the maximum of LSPR should increase. Oppositely, when tip-to-tip interaction dominates, the values extinction at the wavelengths higher than the maximum LSPR should increase. In the present case, there is no clear tendency for the shift of the plasmon band - there is decrease of the extinction over whole spectral range -, suggesting, at the first sight, the presence of different mutual orientations. It was then hypothesized that if there is an preferential increase of extinction on either side of plasmon band during the clustering then such a increase would serve to assess qualitatively preferential side-to-side or tip-to-tip arrangement.

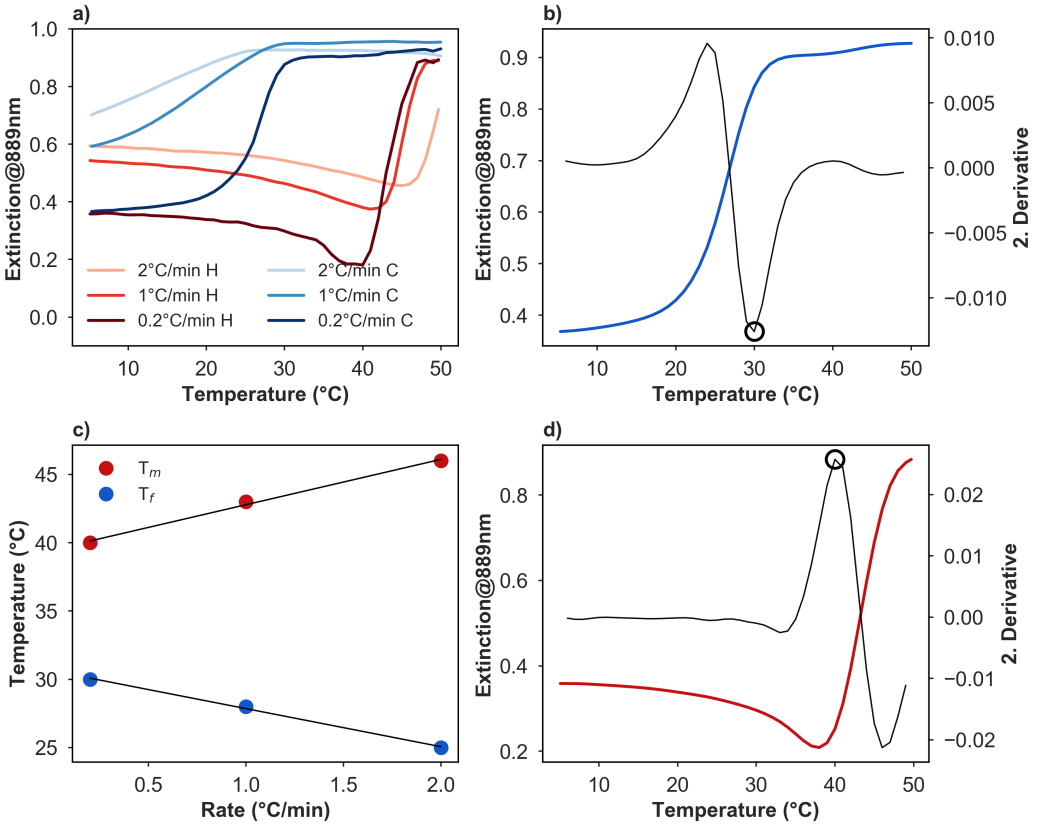

Figure 3.2.9: Methodology for calculating transition temperatures, T_m (melting), T_f (freezing) as well as the value of thermal hysteresis in clustering gold nanorods. a) Raw data of thermal hysteresis obtained at different scan rates: 0.2, 1, 2 °C/min). b,d) estimated local minimum (T_m - open circle) and maximum (T_f) from second derivatives for cooling b) and heating d) scans, respectively. c) extrapolation of fitted transition temperatures as a function of scan rate. Extrapolation of linear regression to 0 °C/min gives the value of rate-independent hysteresis, an intrinsic property of the system which depends on chemical composition of the sample (see Figure 3.2.10).

To evaluate such hypothesis the values of extinction at the three wavelengths (800,

889 and 1000) were tracked during thermal hysteresis (Figure 3.2.8). For the wavelengths at 889 and 1000 nm there was similar drop of extinction suggesting no preferencial tip-to-tip arrangement (Figure 3.2.8b, c). Interestingly, at 800 nm (a wavelength shorter than maximum of LSPR) there was a significant increase of the extinction below 30 °C, followed by its decrease at 20 °C (Figure 3.2.8 d). It is postulated that during the clustering, there is indeed a sign of side-to-side clustering. This analysis indicates that a real-time optical characterization of aggregating gold nanoparticles can provide a meaningful information on the mutual orientation of the nanoparticles and confirm data obtained by other more advanced techniques such as SAXS.

Next the effect of both the CTAB and NaCl concentrations on the extent of hysteresis was studied. To quantify the extent of rate-independent hysteresis, the data processing was developed in customized script in Python programming language. The values of extinction at 889 nm were recorded in temperature window between 50 °C and 5 °C at three scan rates: 2, 1 and 0.2 °C/min (Figure 3.2.9 a). The transition freezing temperature (T_f) was estimated from the minimum of second derivative of the cooling scan (Figure 3.2.9 b), while the transition melting temperature (T_m) was estimated from the maximum of second derivative of the heating scan (Figure 3.2.9 d). The change of transition temperatures as a function of scan rate was fitted with a linear regression of opposite slopes (Figure 3.2.9 c). Finally the value of thermal hysteresis (rate-independent) was estimated by extrapolation of fitted lines to an infinitely slow temperature rate giving thus the values of T_{m0} and T_{f0}. The difference of T_{m0} and T_{f0} gives the value of rate-independent hysteresis. As of note, second derivative of optical data vs. temperature gave a reliable data analysis, because application of fast scan rates for a rather slow aggregation would alter the data if first derivative would have been implemented.

Figure 3.2.10 shows the transition temperatures for three concentrations of CTAB (10, 20, 50 μM, upper panel) keeping constant the concentration of NaCl (300 mM) and three concentration of NaCl (200, 300, 400 mM, lower panel) at constant concentration of CTAB (20 μM). Figure 3.2.10 d) and h) summarize the change of T_{m0} and T_{f0} for both parameters. It is clear that the higher the CTAB and NaCl concentrations, the larger is the value of rate-independent hysteresis (The gray area between red and blue lines increases).

For CTAB the thermodynamic hysteresis increases from ∼5 °C to ∼12.5 °C while for NaCl from ∼2 °C to ∼10 °C(Figure 3.2.10 d, h). Worth mentioning is the change of slope (black lines fitted to red and blue points in upper panel) for increasing concentrations of CTAB that indicate the system change to applied stimulus (kinetic hysteresis). The slope flattens with increasing CTAB concentration suggesting that CTAB decreases the response of the system to the change of temperature or, in

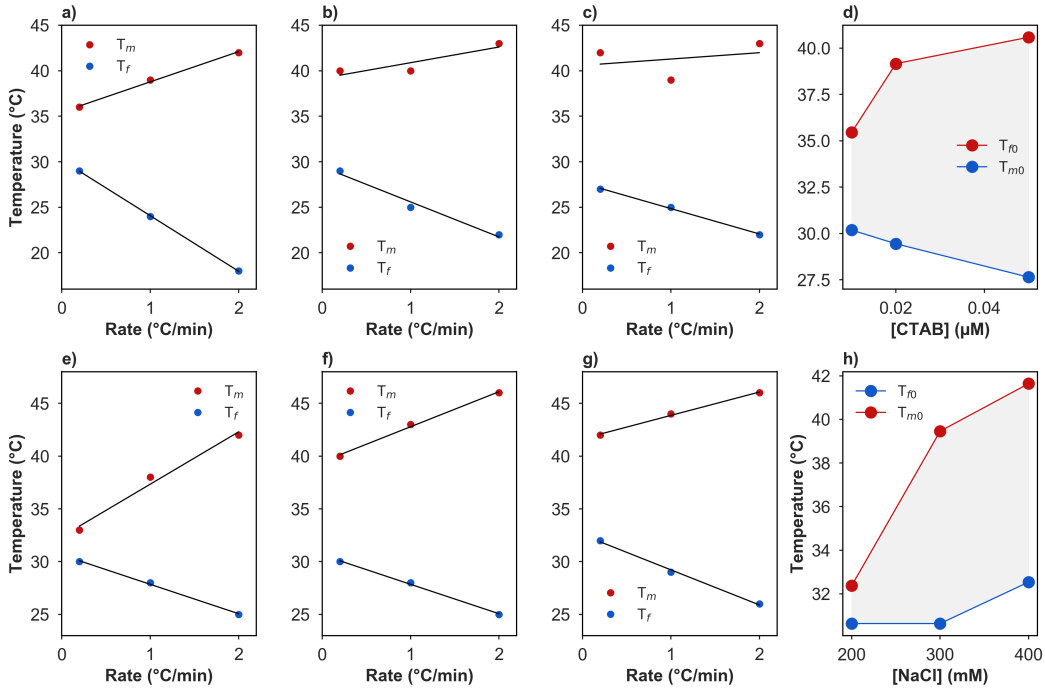

Figure 3.2.10: Effect of CTAB (upper panel) and NaCl (lower panel) concentration on the thermal hysteresis. a-c) Change of T_f and T_f versus scan rate for CTAB concentration ranging from 10, 20 to 50 μM. d) Change T_{f0} and T_{m0} as a function of CTAB concentration. e-g) Change of T_f and T_f versus scan rate for NaCl concentration ranging from 200, 300 to 400 μM. h) Values of T_{f0} and T_{m0} as a function of NaCl concentration.

other words, increases the lag of applied stimulus and system response to that stimulus. Similar trends were observed for increasing NaCl concentration, the nanorods became less susceptible to the change of scan rate (decrease of kinetic hysteresis). Overall, the increasing concentration of both CTAB and NaCl widen the thermal hysteresis by making the system less sensitive to the rate of applied stimulus (decrease of kinetic hystereis).

A careful reader might ask the question whether the aspect ratio of nanorods can affect the hysteretic signature of the system. As a reminder, the previous chapter 2 showed that nanoparticle dimensions had indeed a significant influence on the transition temperatures T_m and T_f. To test whether thermal hysteresis is sensitive to nanorods dimension, four samples were prepared with the following aspect ratios: 2.1, 2.6, 4.4, 4.8. Figure 3.2.11 a) and b) shows optical properties and size distributions of the samples. Each sample was subjected to thermal cycling process at constant conditions (10 mM BSPP, 20 μM CTAB and 300 mM NaCl). The only difference was the wavelength of monitored extinction because of different LSPR maxima (641, 711, 889 and 987 nm) for the samples with increasing aspect ratio. Figure 3.2.11 c) shows normalized thermal cycle of each sample. No clear tendency was observed, that is, all samples behaved similarly. A closer look at the transition

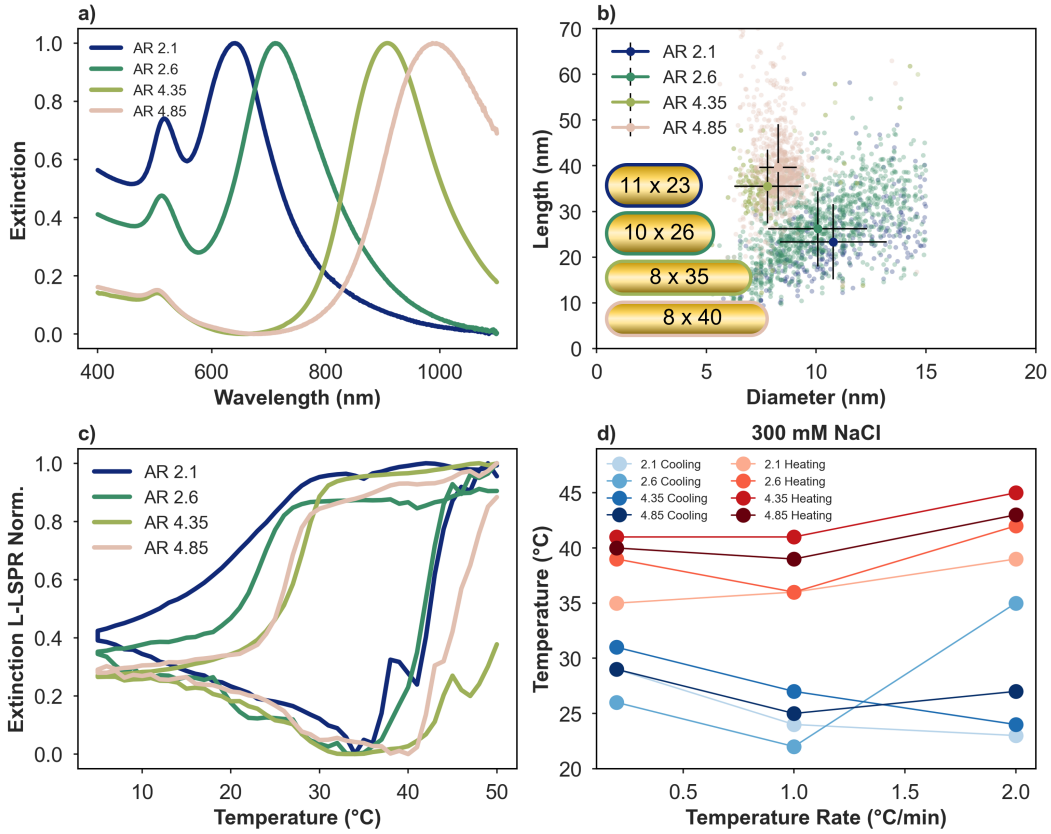

Figure 3.2.11: The effect of nanorods aspect ratio on thermal hysteresis. a) UV-Vis-NIR spectra of gold nanorods with different aspect ratio showing that the maximum of LSPR falls at longer wavelength with increasing aspect ratio. b) Length versus width for all samples with highlighted main values and standard deviations. Inset shows sizes of gold nanorods. c) Raw data of thermal cycling (0.2 °C/min) for gold nanorods with different aspect ratio showing no difference in thermal response of the samples. d) Calculated values of thermal hysteresis (see Figure 3.2.9) showing the lack of tendency of T_f and T_f for different aspect ratio.

temperatures, T_m and T_f confirmed that aspect ratio has no effect on thermal hysteresis. Similar results have been reported by Iida et al.,[60] who showed that the aspect ratio of nanorods has no major effect on the way these nanoparticles assemble during lowering the temperature. These authors have proposed that instead of aspect ratio it is the effective volume of the particle that plays a major role in the clustering process. It is reasonable to assume that in the present system a similar explanation applies since the volume of the particles remains constant (1806, 2042, 1759, 2010 nm^3 with increasing aspect ratio). Thus, it was concluded that thermoresponsive properties of sample containing nanoparticles is largely governed by surface composition of BSPP/CTAB and ionic strength of solution rather than the extent of the shape anisotropy.

3.2.4 Mechanistic considerations

The previous chapter showed that reversible clustering and the extent of hysteresis are governed by the change of electrostatic repulsion at different temperatures. Here, the proposed mechanism is further explored to shed light on the effect of NaCl and the role of CTAB in reversible clustering.

In regards the effect of NaCl, Figure 3.2.12 a) shows that at low amount of salt (25 mM) and in the absence of CTAB the ζ-potential of spherical particles drops from -30 to -48 mV during cooling, that is, the surface potential became more negative at low temperature. Note that at this salt concentration the nanoparticles do not cluster during cooling, which can be explained by the pronounced electrostatic repulsion over the entire temperature range. At higher NaCl concentration (e.g., 100 mM) the ζ-potential becomes practically invariant to the temperature change; it drops only by 5 mV to reach the value of - 18 mV at 5 °C. At this salt concentration the particles do cluster reversibly. Such a trend indicates that at higher salt concentration, during the drop of temperature to 5 °C, the salt ions screen the surface charge, inhibiting thus the electrostatic repulsion to become dominant and thereby allowing aggregation. Now, this trend does not explain why the clustering occurs at 100 mM, especially if ζ-potential remains negative over the entire temperature range (Figure 3.2.12 a - blue). It is postulated that BSPP can form reversible bonds with metal surface. BSPP molecules can strongly interact with gold via Au-P (15-20 kcal/mol)[119], serving as an anchor point on metal surface. Additionally, BSPP bears two Ph-SO_3 functional groups that can form a weak interaction with gold via Au-SO_3, as has been shown previously[125]. By lowering the temperature, both type of interactions are favored through a cooperative effect, making the molecular shell more compact resulting in the drop of steric repulsion, hence aggregation. During heating, molecular rearrangement - and presumably the breakage of Au-SO_3 bond[126] - provides sufficient energy (work) to overcome attractive van der Waals interactions and thus recover initial colloidal stability.

The role of CTAB in reversible clustering involves the blocking of attractive and repulsive interactions. As shown above, BSPP alone suffices to sustain reversible clustering of spherical nanoparticles, but extra CTAB is required in the case of nanorods. To understand the effect of CTAB on the composition of metal-liquid interface DLS and ζ-potential measurement were conducted for different concentration of the surfactant (Figure 3.2.12 b and c). It was shown that with increasing CTAB concentration the hydrodynamic diameter of spherical nanoparticles increased from 22 to 27 nm (Note that for the sake of simplicity spherical particles of 13 nm in diameter were used as a model system). Thus, the height (H) of the molecular shell increased 2.5 nm from 4.2 to 6.7 nm, indicating that CTAB molecules did adsorb

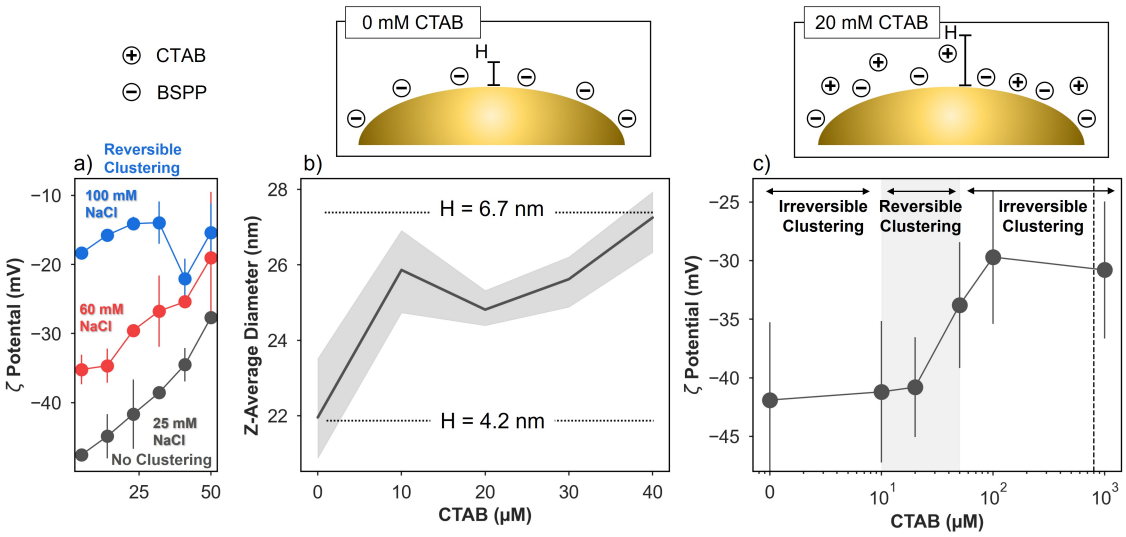

Figure 3.2.12: Effect of NaCl and CTAB concentrations on the change of surface composition during reversible aggregation of spherical nanoparticles. a) Change of ζ-potential as a function of temperature for different salt concentration, showing that at higher salt concentration potential become invariant. b) Change of thickness of molecular layer with increasing concentration of CTAB. c) Change of ζ-potential with increasing CTAB concentration, showing that reversible clustering falls at the change of zeta-potential, at sub-cmc concentration range. Upper panel: schematic representation of surface composition at 0 and 20 μM of CTAB and 10 mM of BSPP.

on metal surface in the concentration range from 0 to 50 μM. It is known that the thickness of CTAB bilayer is 4 nm above critical micelle concentration (cmc = 0.95 mM)[106]. Here, the concentration of CTAB is much below cmc (20 μM) what could explain the formation of a CTAB monolayer on gold surface. The formation of CTAB layer on gold surface was further confirmed by the change of ζ-potential (Figure 3.2.12 c). Interestingly, the change of ζ-potential towards more positive values takes place at the CTAB concentration window for reversible clustering. Finally, it is reasonable to assume that the ionic pair formation between negatively-charged BSPP and positively-charged CTAB on gold nanoparticles makes the molecular layer more 'rigid', resulting in the needs for higher energy input to rearrange the molecules upon aggregation or redispersion. Such a larger energy input leads to widening of thermal hysteresis, as observed experimentally.

3.3 Conclusion

In this Chapter, new experimental, two-step protocol has been proposed for obtaining solution of gold nanorods sensitive to temperature. The simplicity of the present methods is based on the use of canonical molecules in colloidal synthesis (CTAB and BSPP) without the need of using complex thermoresponsive macromolecules such as pNIPAM or DNA. In contrast to spherical nanoparticles it was found, that AuNRs

could became sensitive to temperature through a mixture of both BSPP and CTAB. The extent of thermal hysteresis increased with increasing CTAB and NaCl concentrations, but being CTAB a parameter possesing stronger influence on hysteresis, lowering T_{f0} and increasing T_{m0}. The aspect ratio of nanorods had a negligible influence on hysteretic behaviour. Mechanistic consideration indicates that the ionic pair between positively charged CTAB and negatively charged BSPP renders a rigid molecular shell that requires larger energy input to induce aggregation or redispersion, explaining thus the origin of wide thermal hysteresis.

3.4 Materials and Methods

3.4.1 Materials

Ascorbic acid, sodium chloride, bis(p-sulfonatophenyl)-phenylphosphine, tetrachloroauric(III) acid, silver nitrate, hydroquinone and CTAB were purchased from Sigma-Aldrich and used without any further purification. All glassware was cleaned with aqua regia and rinsed thouroughly with Milli-Q water.

3.4.2 CTAB assisted synthesis of gold nanorods

Mini gold nanorods stabilized with CTAB (AuNRs@CTAB) were synthesized following the protocol from Murphy[120]. First a seed solution was prepared. $HAuCl_4$ (100 μL , 50 μM) was added to CTAB solution (9.4 mL, 100 μM) in a 20 mL vial and kept at 27 °C for 10 minutes. Afterwards, freshly prepared ice-cold $NaBH_4$ (600 μL, 20 μM) solution was added fast to the prepared gold solution under heavy stirring (1000 rpm). The solution turned instantly brown and was aged for 2 hours at 27 °C. In the meantime the growth solution was prepared. $HAuCl_4$ (0.5 mL , 50 μM) was added to CTAB solution (45 mL, 100 μM) in a 250 mL Erlenmeyer flask and kept at 27 °C for 10 minutes. Then, silver nitrate solution (75 μL, 100 μM) and hydroquinone solution (2.5 mL, 100 μM) were added subsequently. After each addition, the solution was carefully inverted. At last, 5 mL of seed solution were added fast under heavy stirring (1000 rpm) to the growth solution and subsequently led to rest at 27 °C until particle growth was completed (ca. 6 hours). Obtained AuNRs@CTAB were washed thrice with centrifugation at 14000 rpm for 25 minutes and redispersed in 1 mM CTAB solution. After the last washing steps, AuNRs were redispersed in 1 mL 1 mM CTAB solution and stored for further use. Depending on the aspect ratio, the reagents and their concentration may vary. The here used parameters are described in Table 3.2. Especially the reducing agent ascorbic acid (AA) or hydroquinone (HQ) play a major role for final aspect ratio.

Aspect Ratio	Reducing agent	$AgNO_3$	HCl (1 M)	Seed	CTAB
2.1	AA 0.1 M, 80 μL	10 μM, 30 μL	200 μL	2 mL	8 mL
2.6	AA 0.1 M, 80 μL	10 μM, 50 μL	200 μL	2 mL	8 mL
4.35 - 4.85	Hq 0.1 M, 0.5 mL	100 μM, 40 μL	0 μL	1 mL	8 mL

Table 3.2: Synthesis parameter for AuNRs with different aspect ratios

3.4.3 Functionalization of gold nanorods with BSPP

AuNRs@CTAB were functionalized with BSPP using a two-step ligand exchange method. In a typical procedure, 50x concentrated AuNRs@CTAB (50 μL) were added to 5 mL of a solution containing BSPP (10 mM) and CTAB (20 μM) under sonication at 50 °C. The solution was sonicated for another 10 minutes and stored for 16 hours at room temperature. The next day, the sample was centrifuged (11000 rpm, 40 minutes) and redispersed in a solution containing 10 mM BSPP and 20 μM CTAB and sonicated at 50 °C for 10 minutes. Afterwards, the AuNRs were ready for usage.

3.4.4 Temperature resolved UV-Vis-NIR measurements

Aqueous dispersions of AuNRs@BSPP were measured in PMMA disposable semi-micro cuvettes (pathlength = 1 cm). Before executing thermal cycling, samples were equilibrated at 50 °C for 20 minutes to ensure full redispersion. The temperature was cycled between 50 and 5 °C subsequently with rates of 2, 1 and 0.2 °C/min. Data was acquired every 1 °C.

3.4.5 Temperature dependent SAXS measurements

Small-angle X-ray scattering (SAXS) experiments were conducted using a Rigaku 3-pinhole PSAXS-L equipment operating at 45 kV and 0.88 mA. The MicroMax-002+ X-ray Generator System is composed of a Microfocus sealed tube source module and an integrated X-ray generator unit and produces Cu Kα transition photons of wavelength $\lambda = 0.1542$ nm. The flight path and the sample chamber in this equipment are under vacuum. The scattered X-rays are detected on a two-dimensional multiwire X-ray detector (Gabriel design, 2D-200X). After radial integration, the scattered intensities were obtained as a function of momentum transfer $Q = 4\pi\lambda - 1 \sin\theta$. Silver behenate was used as standard for reciprocal space calibration. The sample to detector distance was 2 m, covering a q-range between 0.01 $Å^{-1}$ and 0.2 $Å^{-1}$. The measurements as a function of temperature were performed by means of a Linkam Scientific Instruments THMS600 temperature controller. AuNRs were placed between 2 mica windows separated by an O-ring and hermetically sealed placing the

set up into a sandwich type sample holder closed with screws. Data was fitted using a form factor of spherical particles with polydispersity described by the log normal distribution (SASfit software package). To obtain the form factor, SAXS data were collected for 60 minutes at RT for AuNRs@BSPP in 10 mM BSPP without NaCl. For themoresponsive AuNRs, 300 mM NaCl were added to the sample and spectra were recorded for 20 minutes at 60 °C and 5 °C. For each sample, SAXS spectra were corrected with background spectra taken at corresponding temperature.

CHAPTER 4

Oscillatory clustering of gold nanorods under light irradiation

4.1 Introduction

Owing to their large absorption cross-section, gold nanorods exhibit excellent photo thermal properties, rendering them efficient nano-heaters. Such property is fundamental for their application in nanomedicine, where nanoparticles, by absorbing infrared radiation in optical biological window, can enhance drug delivery[127–129] or induce death of cancer cell by thermal ablation.[130–132] But photothermal effect driven by plasmonic nanoparticles goes beyond biomedical applications. The interaction of light with nanoparticles is an interesting strategy for development of soft matter actuators. By embedding plasmonic nanoparticles within thermoresponsive matrix one can induce reversible actuation under light irradiation, giving rise to micro angular motion[133] sequential wavelength dependent actuation[134], smart windows through reversible turbidity, [135, 136] switchable displays[137] or shape memory materials based on DNA-hydrogel composites.[138] However, the reversible actuation of these systems is based on temporal application of stimulus (ON-OFF states) while the signal transducer (local heaters) and responsive matrix are physically decoupled entities. In this chapter, a question has been imposed whether one can induce a temporal change of system state (clustering) under the action of uninterrupted light irradiation.

Recent development of soft-matter actuators revealed that indeed such a system is feasible. For example, Zeng et al.[139] have designed a liquid crystal polymer network that possessed an oscillatory movement dependent on the beam position relative to the material and could be switched between bending, twisting and contraction/expansion. In a more recent example, Yang et al.[140] have demonstrated oscillatory change of structure in a carbon-nanotube-based bimorph actuator. Under constant white light irradiation, the material exhibited directed mechanical move-

ment. Without any doubt, a system that exhibits cyclic structural change under uninterrupted energy supply (e.g., light) is rather exotic in material science, and remains virtually unaddressed in nanoparticles self-assembly.
From a broader perspective, a system that exhibits oscillatory behavior (e.g., periodic movement) under external energy source that lacks corresponding oscillations (periodicity) is classified as self-oscillator[141, 142]. Self-oscillator differs from a resonant system where the oscillation is modulated externally by an energy source. To generate oscillations but without using periodic external energy source, a transducing material, by absorbing energy from the external source, should alter local environment which in turn affects the way the transducing material interacts with the external source. Thus, it is the oscillator itself that maintains the frequency with which it is driven, and transducing material and environment are coupled. Self-oscillation is the result of a subtle interplay between feedback responses within the system once it is subjected to the uninterrupted external power. On one side, under external source of power, the systems state can change in a way that can increase the transduction rate of energy from external source to environment, resulting in a positive feedback mechanism. On the other side, the systems state can also change in a way that decreases the transduction rate of energy from external source to environment, leading to a negative feedback mechanism. While positive feedback tends to induce instability within the system, the negative feedback promotes system stability. Interestingly, many biological phenomena, such as heartbeat or firing of neurons comprises both type of mechanisms and indeed exhibit self-oscillatory properties.[141]
In this chapter, we will exploit the possibility of obtaining experimentally an oscillatory clustering of gold nanoparticles under uninterrupted laser irradiation. First, we will discuss the conceptual design of a colloidal system and features the system should have to observe oscillations. Second, we will construct the experimental setup equipped with real-time analytics to detect eventual oscillatory signature under laser irradiation. Third, we will study light-induced reversible clustering of gold nanorods under interrupted light conditions (ON-OFF) to find the optimal conditions at which gold nanorods can transduce light energy into local heat to induce their own redispersion. Fourth, we will discus light-sustained oscillatory clustering of gold nanorods and show how to control them experimentally. Finally, the role of feedback mechanisms on the oscillatory clustering will be discussed.

4.2 Hypothesis

In the previous chapter we have seen that temperature - an external physical stimulus - can modulate the reversible clustering of gold nanoparticles. Also, it was shown in the introduction section (section 1.4) that gold nanoparticles can effectively convert light energy into heat, where the drop of interparticle distance favours collective heating which dominates the heat generated by individual nanoparticles. The combination of these two features - thermoresponsive clustering and photothermal effect - allows for the formulation of the central hypothesis of the present chapter:
The difference in the efficiency of photothermal effect in dispersed and aggregated solution of gold nanoparticles can lead to a scenario where under uninterrupted supply of light energy the colloidal solution experiences oscillatory clustering.
Figure 4.2.1 shows a visual description of the hypothesis. Gold nanorods undergo spontaneous and slow aggregation upon cooling, altering their optical properties in a way that the absorbance at LSPR decreases while the absorbance at longer wavelengths increases (Figure 4.2.1 a). In the course of aggregation, the system absorbs more light at 1064 nm making dominant the collective heating that eventually can rise the temperature of the solution to induce redispersion. Once the particle redisperse, the photothermal effect decreases because individual particles are unable to produce enough heat to maintain the colloidal solution in dispersed state; the temperature of the solution decreases. This will leads again to aggregation which in turn will increase photothermal effect allowing the particles to redisperse. Overall, the system exhibits oscillatory clustering (Figure 4.2.1 b).
Figure 4.2.1 c) shows a hypothetical temporal evolution of both, the extinction (black line) and local temperature (red).

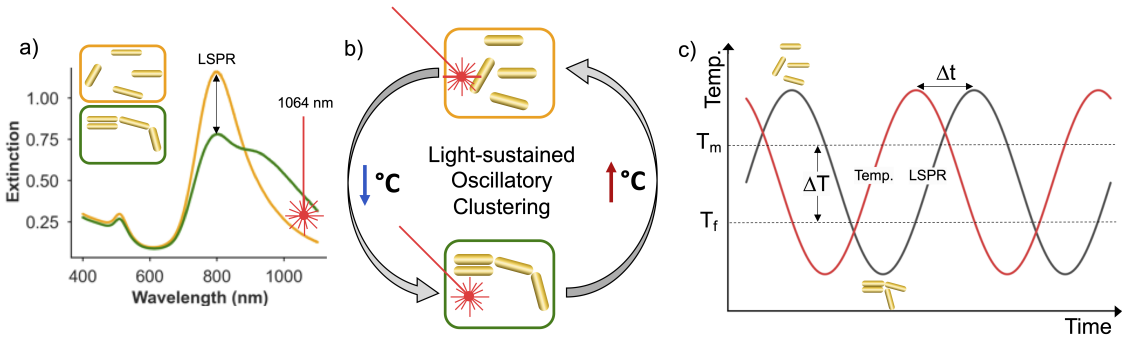

Figure 4.2.1: Conceptual design of light-sustained oscillatory clustering of gold nanorods. a) UV-Vis-NIR spectra of two limiting states: aggregated (green) and dispersed (yellow). b) Visual demonstration of oscillatory clustering under uninterrupted supply of external stimulus. c) A hypothetical scenario of temporal evolution of extinction at LSPR (black) and local temperature during oscillatory clustering. ΔT - thermal hysteresis, Δt kinetic hysteresis - the lag of nanoparticles redispersion to the changing temperature.

The change of extinction and the change of local temperature must be coupled, that is, the nanoparticles by absorbing light change their local environment and the change of the environment changes the way the particles interact with external uninterrupted stimulus, hence a self-oscillator. To obtain oscillatory clustering two following conditions must be met:

- The temporal change of aggregation and temperature need to be out of phase. The redispersion of nanoparticle should follow the change of local temperature. The origin of such a delay is the lag of redispersion rate under temperature increase (here action of light). The reader was familiarised with such a phenomena in previous chapters when kinetic hysteresis was discussed.

- The system to oscillate needs the presence of thermal hysteresis (or thermodynamic hysteresis), defined as the difference between T_m and T_f. Thus to oscillate, the nanosystem needs to traverse across the hysteresis, to be either above T_m or below T_f, otherwise the system reaches steady state conditions.

Both parameters, ΔT, Δt are intrinsic characteristic of gold nanorods solution undergoing reversible clustering, their values cannot be modulated on demand. The laser power is the sole experimental parameter one can tune in real-time to modulate the photothermal effect.

4.3 Experimental Design

The evaluation of proposed hysteresis requires careful design of experimental station equipped with real-time analytics. Figure 4.3.1 shows schematically the experimental design. A four-windows, temperature-controlled cuvette holder (qpod-2e) was coupled with the laser beam and white light (sphectrophotometer); both positioned orthogonally to monitor in real-time the change of optical properties of the solution in the volume exposed to laser light.
The laser operated at a frequency of 50 MHz with a pulse length of ∼10 ps and a nominal power ranging from 0 and 10 W. Note that the pulse length, was long enough to ensure photothermal relaxation of nanoparticles which takes approximately 1.7 ps independently of nanoparticle dimensions (Figure 1.4.1). Thus the possibility of generating hot carriers was minimized. The laser light (λ = 1064 nm) was coupled into an optical fiber that was connected to one of the qpod-2e ports with a collimator lens (diameter = 5 mm). The laser beam passing through the sample was collected in a beam stop.
The UV-Vis-NIR spectra were recorded using Halogen-Tungsten light source and MayaPro spectrometer (Ocean Optics), both connected with collimator lenses. A

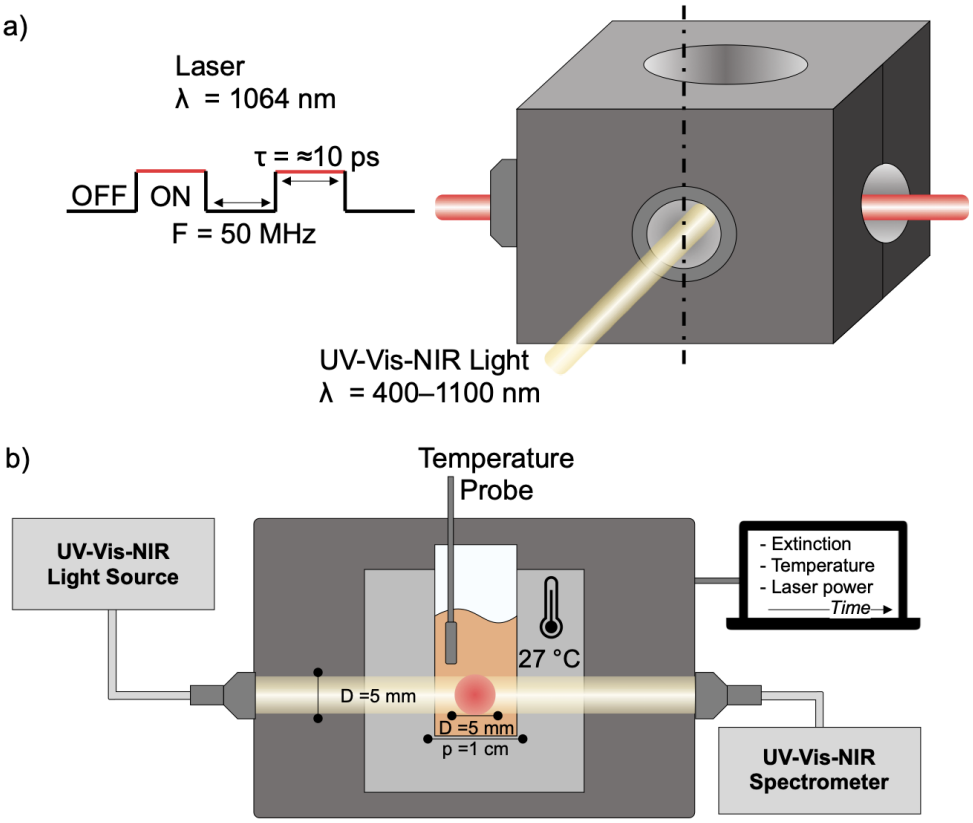

Figure 4.3.1: Experimental setup. a) Schematic description of laser light properties and location of both laser beam and light source for optical monitoring. b) Cross section view of the holder showing the beam size, temperature probe and based temperature. The holder was connected to external computer to monitor in real time extinction spectra and temperature, while laser power was modulated on demand.

quartz-cuvette (optical path = 1 cm) containing gold nanorods sample (2 mL) was placed into qpod-2e and was encased within a peltier element, so that temperature control was achieved from all sites and the bottom. The based temperature was kept constant of 27 °C. The temperature inside the solution was monitored through thermocouple (ThorLab) placed above the laser light beam to avoid laser induced-heating. The values of temperature and UV-Vis-NIR spectra of the solutions were recorded every 2 seconds. The laser power was changed on demand during the course of the experiments.

4.4 Results

The present section is organized as follows: first, the capacity of photothermal heating by gold nanorods is evaluated, followed by experiments in which laser light is used as physical stimulus to induce photothermal redispersion under ON/OFF stimulus state. Then, the kinetic analysis of the redispersion and temperature change is provided, followed by the analysis of oscillatory clustering, showing the importance

of thermal hysteresis within the thermoresponsive system. The effect of laser power density on frequency of oscillations is also discussed.

4.4.1 Light-to-heat conversion by gold nanorods

Before studying reversible clustering and oscillations, one needs to assure that gold nanorods are efficient heaters. To study this, a solution of stable gold nanorods (LSPR = 889 nm) was used.

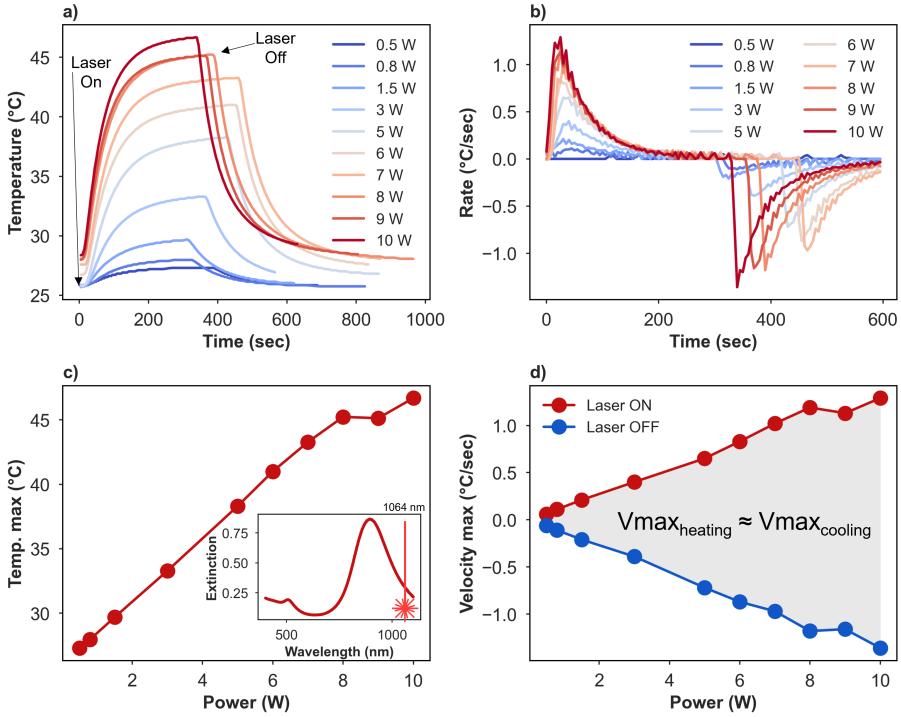

Figure 4.4.1: Temperature change in the solution of dispersed gold nanorods under ON and OFF light conditions. a) Temperature curves for laser power between 0.5 W and 10 W. b) Temperature rate estimated from (a). c) Maximum temperature achieved for given laser power. d) Maximum value of temperature change versus laser power, showing similar slops for both the heating (laser ON) and the cooling (laser OFF) periods.

The sample was subjected consecutive cycles of ON and OFF states with simultaneously monitoring temperature (Figure 4.4.1).
For photo-thermal heating, nominal laser power was increased from 0.5 to 10 W and temperature change was tracked in real-time. After the stabilization of temperature, the laser was turned off and next cycle was initiated when AuNRs solution reached based temperature. As expected, it was observed that with increasing the power laser from 0.5 to 10 W the temperature of the solution reached maximal values ranging from 25 to 47 °C (Figure 4.4.1 a, c). Just after switching laser ON, the heating rate and temperature increased rapidly, reaching the maximum heating rate at ∼1 minute, and decreased gradually afterwards until maximal temperature

was attained and steady state conditions were reached. Oppositely, after turning off the laser, the solution rapidly cooled down starting with high cooling rate which gradually slowed while approaching base temperature. For all laser powers, temperature of the solution stabilized after ∼250 sec, which is confirmed by estimating the heating rate in Figure 4.4.1 b. At 250 sec the value of rate become 0 °C/min. The maximum values of rates at ON and OFF states were plotted versus applied power, showing that the rate of heating and the rate of cooling for dispersed nanoparticles was similar (Figure 4.4.1 d). Note that at the present experimental setup, global temperature of the solution is measured. There is no information on the local temperature change close to the particles surface. The laser power of 10W is quite large energy; at this conditions nanoparticles can suffer from deformation. Thus in the following experiments the maximum power applied was 4.5 W.

4.4.2 Light-modulated reversible clustering of gold nanorods

The aim of the following paragraphs is to show that temperature-induced, reversible clustering of gold nanorods can be modulated externally using laser light as a physical stimulus where the aggregating nanoparticles play a role of light-to-heat transducers. As shown in the previous chapter 3, the clustering of gold nanorods conveys a pronounced change in their optical properties, especially the change in the intensity of LSPR (Figure 4.4.2 b). Such a change can be taken as a reliable measure of clustering dynamics given that the extinction spectra are recorded in time interval much lower than the clustering process itself. For this purpose, a sample was prepared which contained gold nanorods coated with BSPP/CTAB and in the presence of NaCl (300 mM NaCl). The gold nanorods underwent slow clustering (tens of minutes) when based temperature was fixed at 22 °C.

To show photo-thermal redispersion an experiment was designed in which alternating states of light ON-OFF lasted for 5 - 30 minutes and laser power at which ON state was progressively increased from 0.05 to 4.3 W (Figure 4.4.2 a). The temperature of the solution and extinction spectra were recorded every two 2 seconds during the course of whole experiment, giving in total 4800 spectra.

Figure 4.4.2 c) shows time-dependent evolution of temperature (red) and extinction (black) values. Before the first ON state, the particles were allowed to pre-aggregate that was confirmed by the drop of extinction value from 0.85 to 0.55. Then the alternate ON/OFF states commenced (0.05 -1 W), showing a continuous drop of extinction (aggregation) even though the temperature increased progressively from 22 to 26 °C (Figure 4.4.2 c). These results indicate that at this range of laser power, the photothermal effect is insufficient to induce redispersion. Interestingly, at the next ON state (1.69 W), an abrupt redispersion took place accompanied

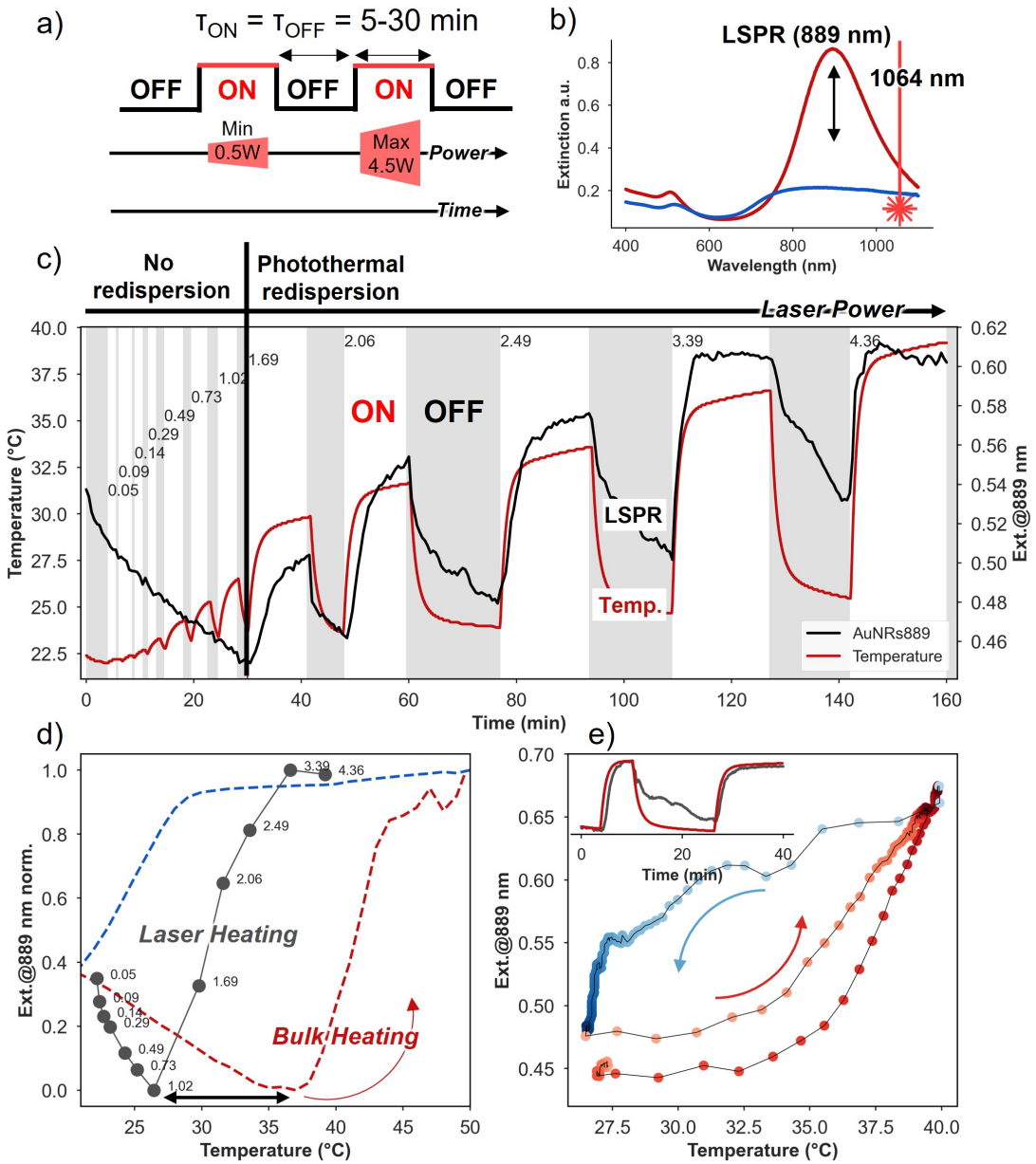

Figure 4.4.2: Reversible clustering of gold nanorods under alternated light irradiation. a) Schematic representation of the experiment. Laser was switched ON and OFF and power was gradually increased at each ON state from 0.05 W to 4.36 W. b) UV-Vis-NIR spectra of aggregated and dispersed nanoparticles, showing also the wavelength of applied laser light. c) Temporal evolution of LSPR and global temperature under ON/OFF laser light with progressively increasing nominal power. The black vertical line at 30 minutes indicates the transition from continuous aggregation to photo-thermal redisperion during ON state. d) Extinction versus temperature for bulk heating and photo-thermal heating, showing that onset of redispersion was downshifted 10 °C for laser heating, suggesting that local temperature close to particle surface is higher than the bulk temperature. e) Hysteresis in the reversible clustering under ON/OFF state.

by temperature jump to 29 °C, revealing the threshold of laser power at which the redispersion takes place. With each consecutive ON state, the temperature

and extinction experienced even larger increase, whereas with each OFF state both temperature and extinction decreased. This data show that (1) light is a valid physical stimulus to control remotely reversible clustering of nanorods stabilised with BSPP/CTAB, and (2) there is a threshold of laser power at which the photothermal redispersion occurs.

As mentioned above, the thermal profile obtained in this experiment provides an information on the global temperature change. That is, the thermocouple used in the experiment cannot provide an information on the local temperature in between the particles under irradiation. On the other hand, the change of extinction, being sensitive to the local orientation of the particles, provides direct information on the aggregation-to-dispersion transition down to nanoparticle level. Therefore, it was hypothesized that the observed threshold of laser power at which the redispersion commences (1.69 W) can give a hint on the difference between the global temperature (measured by thermocouple) and local temperature (indirectly detected by UV-Vis-NIR), given that T_m temperature of the sample is known. Figure 4.4.2 d) compares extinction change versus measured bulk temperature for bulk heating (thermal, red) and light heating (photo-thermal, black). The points in red were obtained by slow thermal cycling of the sample at 0.2 °C/min. The points in black correspond to the maximum extinction obtained at given ON states in Figure 4.4.2 c). Put differently, the points were obtained by removing time component in Figure 4.4.2 c) for the maximum extinction recorded at each ON state. Such analysis shows that aggregation-to-redispersion transition for light heating is downshifted by ∼10 °C. Thus, given that in both types of heating (thermal, photothermal) the measured temperature is the global temperature of the sample, the observed downshift can be used to estimate the temperature close to nanoparticle surface, and which is higher by ∼10 °C. If such reasoning is correct, the proposed method can be used to measure indirectly the local temperature close to particles surface under irradiation, which in fact is a long-lasting challenge in the field of thermoplasmonics.[143] Of course, this method would need to be contrasted with agreed method such as fluorescence life-time.

The data obtained in Figure 4.4.2 c) indicate qualitatively that temperature and extinction do not follow the same path during ON and OFF stages, indicating that there could be a hysteresis in reversible clustering. To confirm that, the mixture of aggregating gold nanoparticles was redispersed twice by irradiation with laser (3.39 W) (see inset in Figure 4.4.2 e). Time component from temperature and spectral data was removed, and temperature-resolved extinction of AuNRs was obtained by combining both data sets. Indeed, a hysteresis was observed, that is, at the same temperature the extinction can receive two values depending if the particles are undergoing redispersion or aggregation. The origin of the hysteresis can be a purely

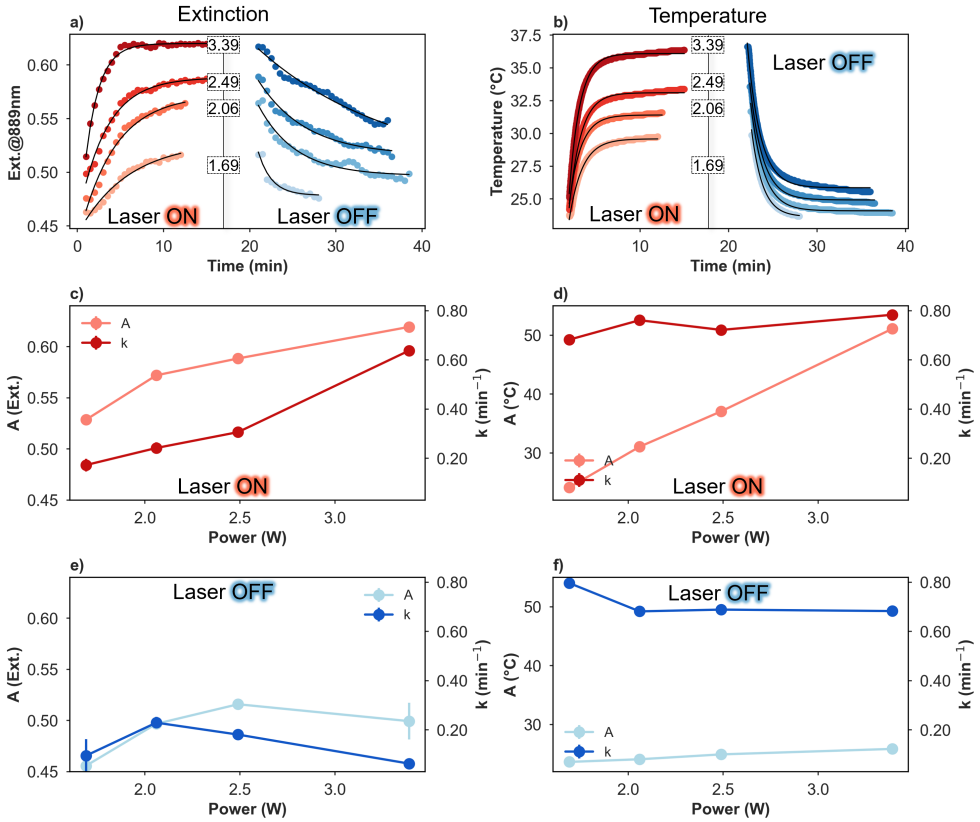

Figure 4.4.3: Analysis of extinction and temperature change at ON-OFF light state. The raw data were fitted with exponential function $y = A - be^{-kx}$ (black lines). A-b) Time-resolved change of extinction (a) and temperature (b) for varying laser power between 1.69 and 3.39 Watt. c-f) Fit parameters (A and k) of extinction (c, e) and temperature (d,f) during ON (c, d) and OFF (e, f) states.

kinetic effect, since redispersion is a fast process due to temperature jump, while aggregation is a slow process depending on the diffusion of the particles.

To quantify the dynamics of extinction and temperature change during ON-OFF states the data from Figure 4.4.2 were fitted with an exponential function of type $y = A - be^{-kx}$. The parameter A represents value at (quasi-)equilibrium, while k is rate constant, a measure of how fast local equilibrium is reached. Taking a closer look at redispersion kinetics during laser ON, one can deduce that the rate constant, k, of the extinction increases with laser power while the rate constant of temperature remains unchanged (compare red lines in Figure 4.4.3 c and d). The difference in the change of rate constants for extinction and temperature is due to the fact that measure of extinctionreflects local changes (interparticle distances) that are sensitive to local temperatures. The measure of temperature (out of laser beam) indicates the global temperature. Thus, even though the maximum temperature increases with laser power, the rate remain unchanged because of the thermal diffusivity of the medium and possible temperature gradient between irradiated and measured volume. By analyzing aggregation kinetics during laser OFF for different power

densities, one can clearly deduce that the rate constant remained unchanged, so did the rate constant of temperature. Overall, this analysis further confirms that photothermal redispersion of gold nanoparticles depends on the applied laser power, while bulk temperature rate remained constant.

4.4.3 Oscillatory clustering of gold nanorods under uninterrupted light stimulus

For studying oscillatory clustering of nanorods under uninterrupted laser light, the selected sample of gold nanorods (see characterisation in subsection 4.6.1) exhibited larger extinction when aggregated than in redispersed state (Figure 4.4.4 a). That is, upon clustering, the absorbance at 1064 nm increased, favouring collective heating due to low interparticle distances and the increase of absorbance at the wavelength of laser (compare the change of absorbance at 802 and 1064 nm obtained during thermal cycle, Figure 4.4.4 b). Such a cooperative effect is expected to promote stronger photo-thermal effect for aggregated nanorods. Figure 4.4.4 c) confirms such assumption where the measured global temperature the sample produced under laser irradiation was higher at aggregated state (large ionic strength) as compared to fully redipsersed state (no salt). The maximum temperature as a function of laser power was fitted with linear regression, resulting in heating efficiency of 0.87, 3.2 and 8.81 °C/W for water, redispersed and aggregated nanoparticles, respectively. Thus, aggregated nanorods exhibited 3 times higher photothermal effect than dispersed nanorods. As a results, under laser light excitation through continuous aggregation/redispersion cycles, AuNRs can "jump" between two different heating capacities which increase/decrease temperature under uninterrupted light irradiation leading to oscillations (Figure 4.2.1 d).

As mentioned above, the sole experimental parameter in the present setting is the laser power that one can modulate on demand during the course of aggregation. To study the presence of oscillations, the initially dispersed nanoparticles (300 mM NaCl) were allowed to slowly pre-aggregate at base temperature of 27 °C. During this process the laser was set ON and the power was modulated from 0.05 to 2.5 W. At each laser power, the system was left undisturbed for 15-25 minutes, recording in real-time the change of temperature and absorbance spectra (400-1100 nm). Indeed, the absorbance at the maximum of LSPR started to spontaneously oscillate when the power laser was modulated in the following, stair-like, order: 2.53, 1.29, 0.8, 1.29, 2.53 and 0.8 W. (Figure 4.4.5 a). The QR code (Figure 4.4.5 a - inset) provides an access to an animation showing spectral and temperature change in a typical experiment. Note that during the oscillation the extinction at LSPR changed within 0.2 units, indicating rather a small fraction of particles undergoing oscillatory

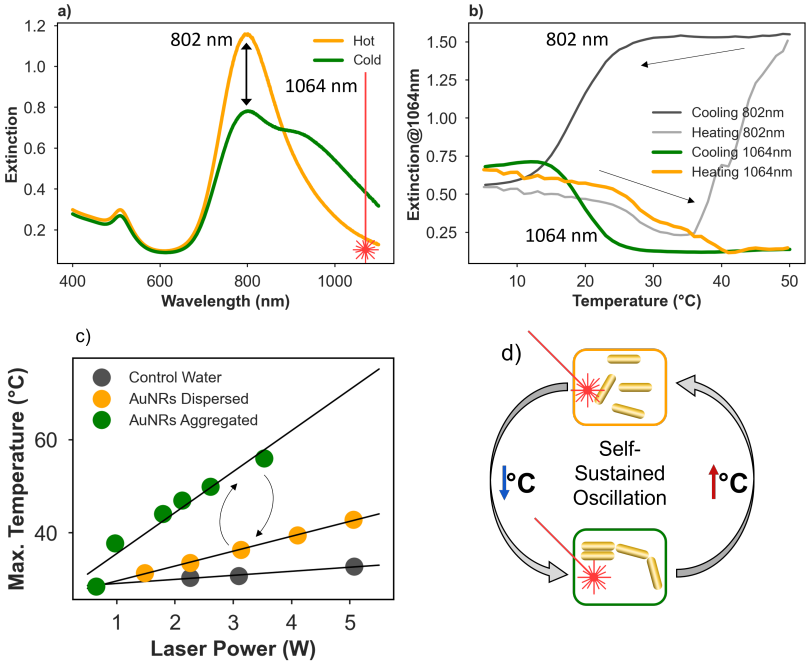

Figure 4.4.4: Optical and themoresponsive properties of gold nanorods. a) UV-Vis-NIR spectra of dipsersed AuNRs at high temperatures (yellow) and of aggregated AuNRs (green) at low temperatures. b) Thermal cycling (Rate = 0.2°C/min) showing increased extinction at 1064 nm at low temperatures, while the intensity at longitudinal LSPR (802 nm, grey lines) follows opposite trend. c) Photothermal heating of dispersed (orange) and aggregated (green) nanorods sample showing higher temperatures at the same laser power for aggregated nanorods. d) Schematic concept of self-sustained oscillation induced by the different heating efficiency of dispersed and aggregated AuNRs.

clustering. Any possible optical artefact accounting for oscillations were excluded, since dispersed nanoparticles under different power laser, showed no variation in the spectrum. During the whole experiment, the temperature remained stable at given power density. The invariance of temperature confirms, again, that in the current experimental setting one cannot resolve the change of temperature locally down to nanoparticles regime.

From Figure 4.4.5 a it is evident that the system exhibits a complex oscillatory pattern, showing various frequencies being superimposed. To resolve these frequencies, fast-fourier transformation (FFT) analysis was conducted for laser powers from 0.8 to 2.53 W (Figure 4.4.5 b-d). The FFT analysis revealed the presence of low frequency oscillation (0.3 - 0.5 $min^{-}1$, yellow bands) and three higher frequencies (2 - 4 $min^{-}1$, blue bands) Both frequency ranges are sensitive to the laser power (Figure 4.4.5 e). It is feasible to attribute the higher frequency pattern to the local increase/decrease of interparticle distance in the illuminated volume since redispersion kinetics depends on the laser power as shown above (Figure 4.4.3). The slow frequency pattern can be attributed to the change of particles and cluster concentra-

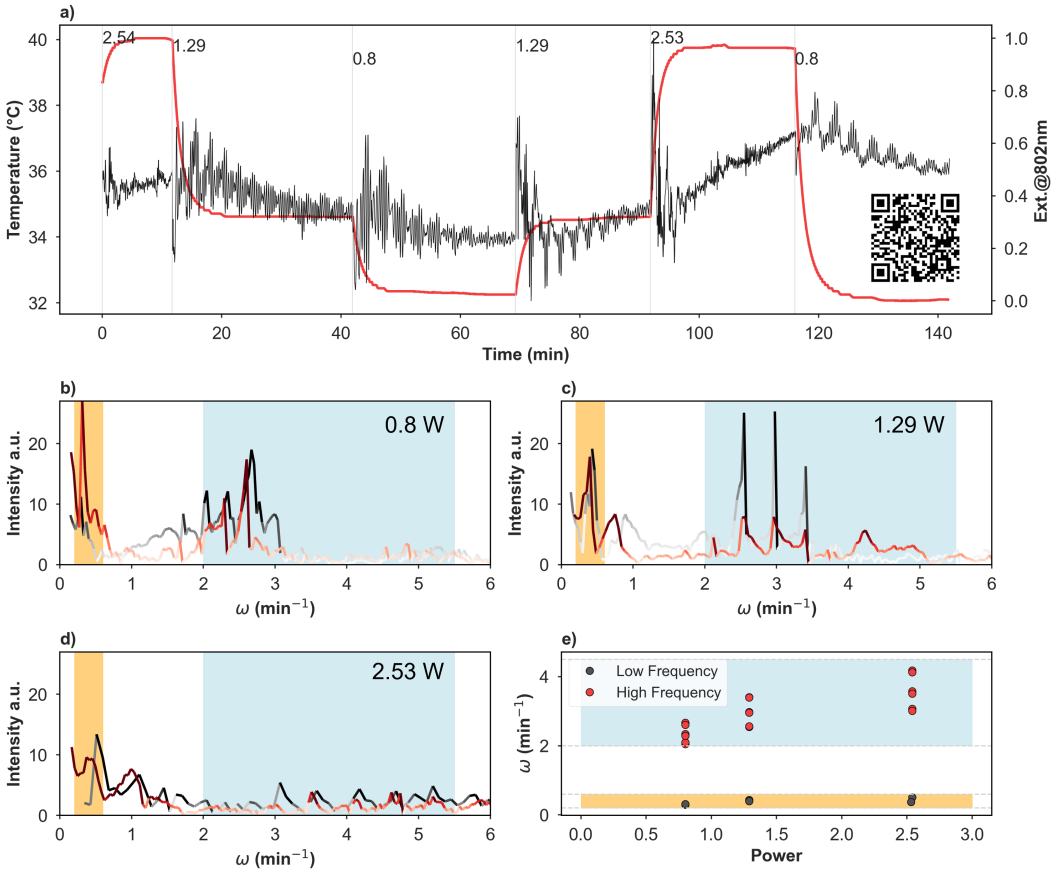

Figure 4.4.5: Oscillatory clustering. a) Time-resolved measurement of extinction (black, 802 nm) and temperature (red), showing the appearance of oscillations in spectral response under uninterrupted light irradiation. Numbers indicate laser power. Inset: QR code to an animation showing spectral and temperature change in a typical experiment. (b-d) FFT analysis of the extinction data in (a) for laser power from 0.8, 1.29 to 2.53 W. Red line- frequency in forward laser power (0.8, 1.29, 2.53 W), black line in backward direction (2.53, 1.29, 0.8 W) showing no effect of power laser on oscillation frequency. Yellow band- low frequency oscillations, blue band - high frequency oscillations. e) Low and high frequencies versus laser power, showing an increase of low frequency oscillation with increasing laser power.

tion within the irradiated volume of the sample. That is, the particles can diffuse out of the volume under irradiation through thermophoresis once the local temperature reach T_m, and later the concentration of particles within such volume is restored, giving rise to the temporal changes of the amount of particles in measured volume. Finally, the direction of changing laser power had no influence on the frequencies, which was confirmed by estimating the frequencies while lowering laser power (2.54, 1.29, 0.8 W) and increasing laser power (0.8, 1.29, 2.54 W), as shown in black and red plots in Figure 4.4.5 b-d), respectively.

Under dark conditions (laser OFF), no oscillations were observed. Figure 4.4.6 a) shows the change of normalised extinction at 802 nm under OFF-ON-OFF states, showing that under dark conditions, the nanoparticles experienced progressive ag-

gregation (drop of extinction), while under laser irradiation the system undergoes oscillatory clustering. This control experiment further confirmed that oscillatory behaviour is related to the interaction of gold nanoparticles with light.

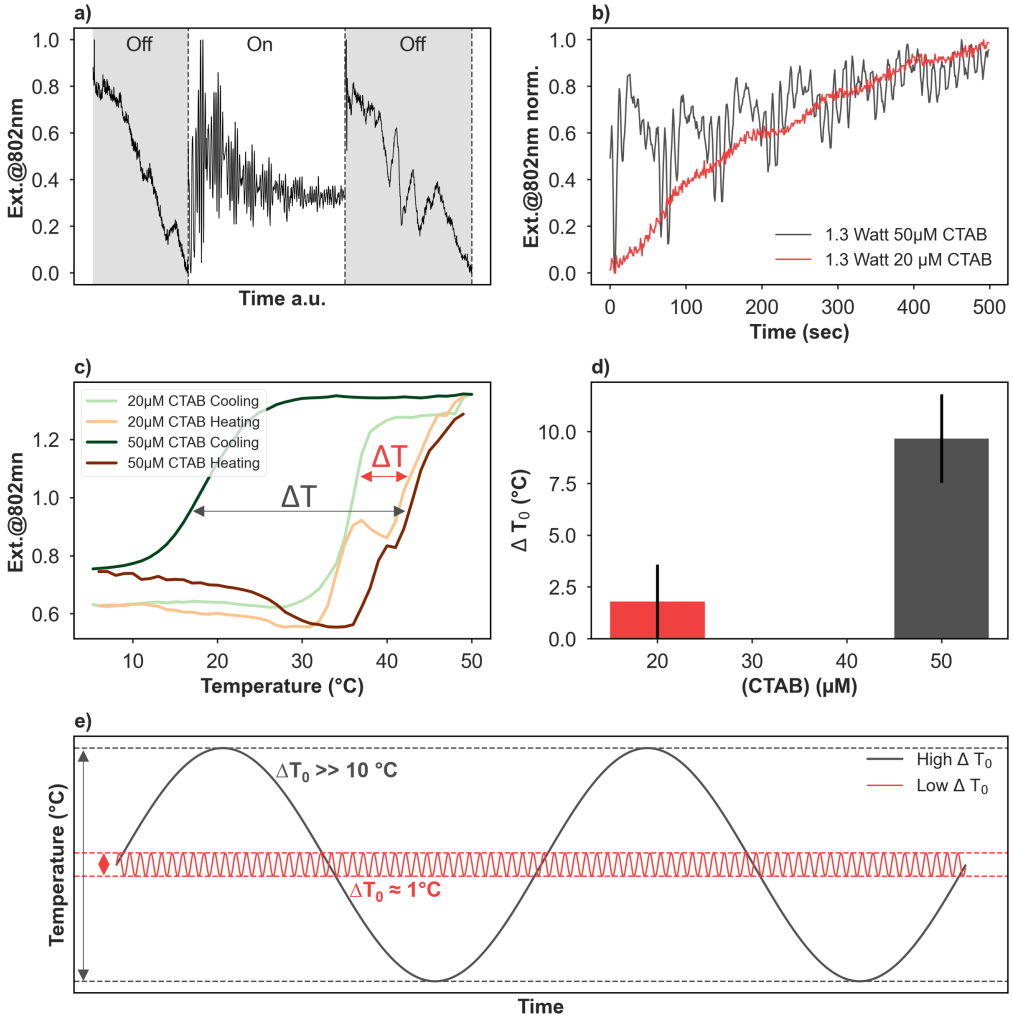

Figure 4.4.6: Control experiments. a) Oscillations were only observed under continues light excitation. b) Oscillations were only observed for nanords with high thermodynamic hysteresis, which was controlled by the amount of CTAB in the solution. c)Thermal cycling at 0.2 °C/min of nanorods with 20 μM CTAB (bright) and 50 μM CTAB (dark). d) Thermodynamic hysteresis for given samples showing large increase with higher CTAB concentration. d) Schematic representation of how oscillation amplitude and frequency change as a function of thermodynamic hysteresis.

Apart from light, histeretic behavior in reversible clustering is a condition for oscillations. As shown in chapter 3, the extent of hysteresis in reversible clustering of AuNRs@BSPP can be modulated by the concentration of CTAB in the sample. Thus, to evaluate the effect of hysteresis on oscillatory clustering two samples of gold nanorods were prepared, containing either 20 or 50 μM CTAB, both with the same concentration of NaCl (300 mM). The sample with lower CTAB concentration showed rather narrow hysteresis, whereas the sample with high CTAB concentration

showed much wider hysteresis (Figure 4.4.6 c). The quantified thermal hysteresis was ∼10 and ∼2 °C for nanorods containing 20 and 50 μM CTAB, respectively (Figure 4.4.6 d). Both samples were subjected to the same laser conditions of 1.3 W, observing that the sample with higher amount of CTAB exhibits more pronounced oscillatory pattern (Figure 4.4.6 b, black). The sample of smaller amount of CTAB had rather noisy response without visible oscillatory response (Figure 4.4.6 b, red). The observed scenario is analogical to the functioning of a thermostat, where hysteresis is deliberately introduced to avoid chaotic system response of cooling/heating at predefined temperature onset. The hysteresis forces the system to pass a threshold above or below temperature onset, resulting in increased amplitude and reduced frequency of oscillations. Figure 4.4.6 e) shows schematically such situation. If thermodynamic hysteresis is small, having small difference between T_{f0} and T_{m0}, the system is allowed to switch rapidly between aggregation/redispersion, rendering high frequency oscillations, that in practice are classified as steady state, since the measurement mean (here UV-Vis-NIR) has not enough resolution to observe oscillatory clustering. Only if a large difference between T_{f0} and T_{m0} is imposed, the system is forced to perform large amplitude oscillations at reduced frequency, which in practice can be detected by spectroscopy. This type of oscillations is classified as a relaxation oscillator[141] and is typically characterized by two threshold points, in which the system oscillates, which in our case are the transition temperatures T_{f0} and T_{m0}.

Although it was only the extinction and not local temperature that was accessible experimentally, it is convenient to picture schematically the interplay of both parameters to obtain better understanding of the mechanism behind oscillations.

Figure 4.4.7 describes the change of local temperature and extinction for different ranges of power laser. At the laser power below the oscillation threshold (Figure 4.4.7 b), the nanoparticles aggregation (drop of absorbance) induces the increase of local temperature that is due to the collective heating and the increase of absorbance at 1064 nm. The temperature increases, however, to a level that is insufficient to induce redispersion (T_m), resulting in the continuous aggregation. At the laser power matching the oscillation conditions (Figure 4.4.7 c), the nanoparticles aggregation induces a rapid increase of local temperature, overcoming the threshold of T_m that in turns induces redispersion. The redispersion, on the other hand, compromises the collective heating and absorbance at 1064 nm, decreasing local temperature which in turns leads to aggregation. In this scenario, the reversible clustering of nanoparticles exhibit a negative feedback mechanism: once the redispersion occurs, the absorbance at 1064 nm decreases, so does the contribution of collective heating and the system is unable to convert enough temperature from incoming light. The presence of negative feedback mechanism, which is introduced by hysteresis, deter-

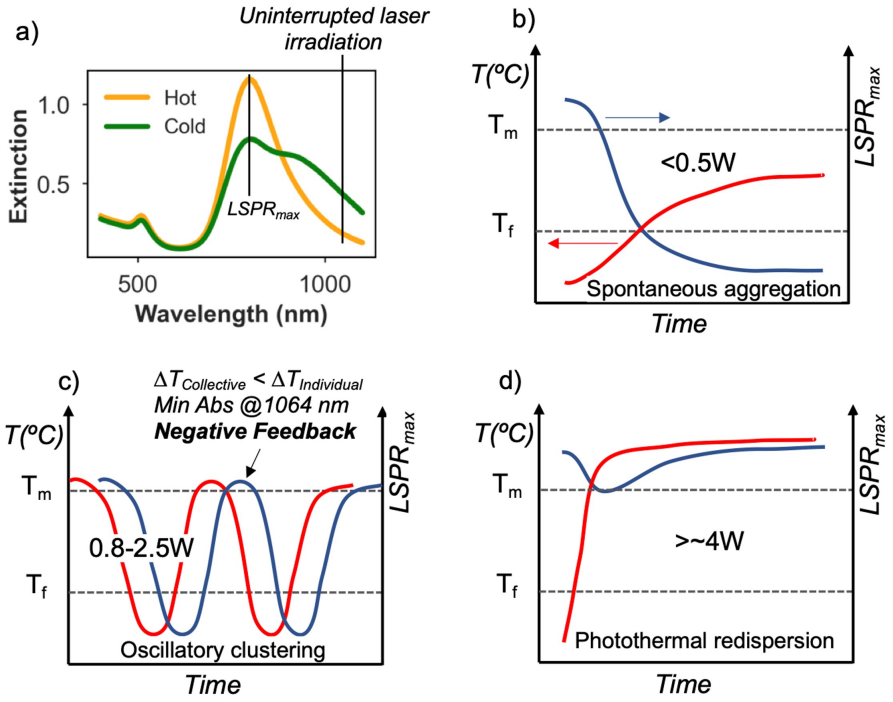

Figure 4.4.7: Mechanism of oscillatory clustering limited by negative feedback. a) UV-Vis-NIR spectra of aggregated and redispersed nanoparticles. b) Power laser below oscillation threshold. c) Power laser within oscillation conditions where negative feedback mechanism allows the system to switch the direction of aggregation and temperature. d) Power laser above oscillation conditions. Redispersed nanoparticles produce sufficient heat to maintain their colloidal stability and prevent aggregation.

mines the oscillatory clustering. A progressive increase of laser power within the oscillatory regime, increases the oscillation frequency that is due to the increase of redispersion rate of nanoparticles. At the laser power above the oscillation conditions (Figure 4.4.7 d), the nanoparticles solution in dispersed state (no collective heating) produces sufficient heat from incoming light to maintain their colloidal stability.

In the above described scenario, the interaction of aggregating nanoparticles with light takes place through a cooperative effect, increase of collective heating and absorbance at 1064 nm upon aggregation.

It has been asked whether an antagonistic scenario can lead to oscillations: increase of collective heating upon aggregation and increase of absorbance at 1064 nm upon redispersion. To explore such scenario, gold nanorods with maximum of LSPR close to the wavelength of incident laser were used (Figure 4.4.8 a). Upon aggregation the sample showed a decrease of extinction at both the maximum of LSPR and at 1064 nm, as confirmed by thermal cycling between 50 °C and 5 °C at the rate of 0.2 °C/min((Figure 4.4.8 b). The value of extinction at 1064 nm during aggregation was ∼6 times lower than during redispersion. In their dispersed state, the

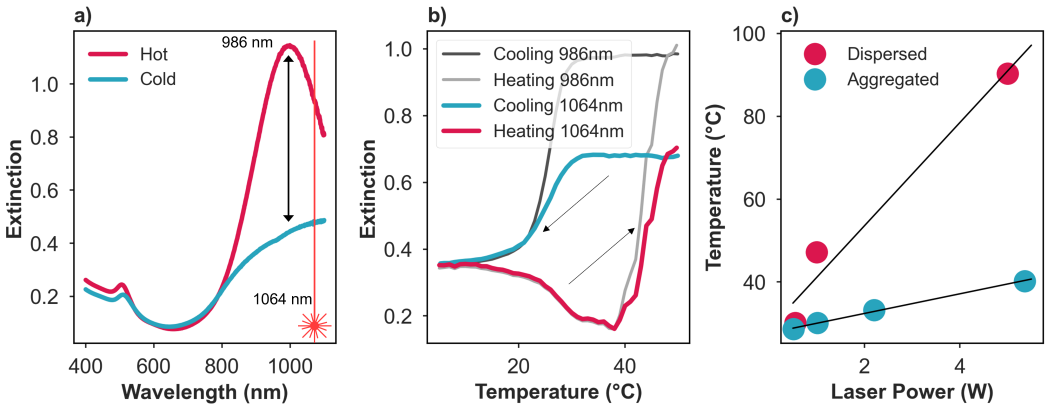

Figure 4.4.8: Optical and thermoresponsive properties of gold nanorods. a) UV-Vis-NIR spectra in their dispersed state at elevated temperatures (pink) and aggregated at low temperatures (cyan). b) Thermoresponsive properties of nanorods with thermal cycling (0.2°C/min) followed at the maximum of LSPR and at 1064 nm. Both wavelengths demonstrate the same trend with a decrease of extinction during cooling and an increase during heating. c) Linear regression of temperature vs. laser power during laser irradiation of aggregated and dispersed nanorods, showing steeper slope for dispersed nanorods.

nanorods showed heating rate of 12.45 °C/W, while in their aggregated state only 2.37 °C/W (Figure 4.4.8 c). Therefore, overall, these nanorods produced more heat in redispersed state under moderate laser power.

Next the redispersion kinetic of these nanorods was tested. The aggregated nanoparticles at the based temperature of 22 °C were exposed to laser power ranging from 0.5 to 3.4 W. Figure 4.4.9 a) and b) show the extinction and temperature change during laser irradiation. At 0.5 W, nanoparticles remained aggregated even though a slight increase of temperature was observed. At this power range, the collective heating dominates (particles remain aggregated) but is not sufficient to increase the temperature to induce redispersion.

With progressive increase of laser power the particles slowly redispersed accompanied by increase of temperature. The fitting of raw data with exponential function ($y = A - be^{-kx}$) showed that temperature rate constant, k, remained unchanged over the entire range of laser power, being consisted with the results shown above (Figure 4.4.9) c, d) The rate constant of extinction increased progressively with increasing power laser, also, being consisted with data shown above. Interestingly, at higher power (3.4 W) the extinction constant rate exceed the temperature constant rate, suggesting that the redispersion of nanoparticles is faster than the change of temperature at higher laser power. This results means that at high enough laser power, the rise of temperature is due to the contribution of both the collective heating and the increase of extinction at 1064 nm, resulting in sudden redispersion and temperature jump.

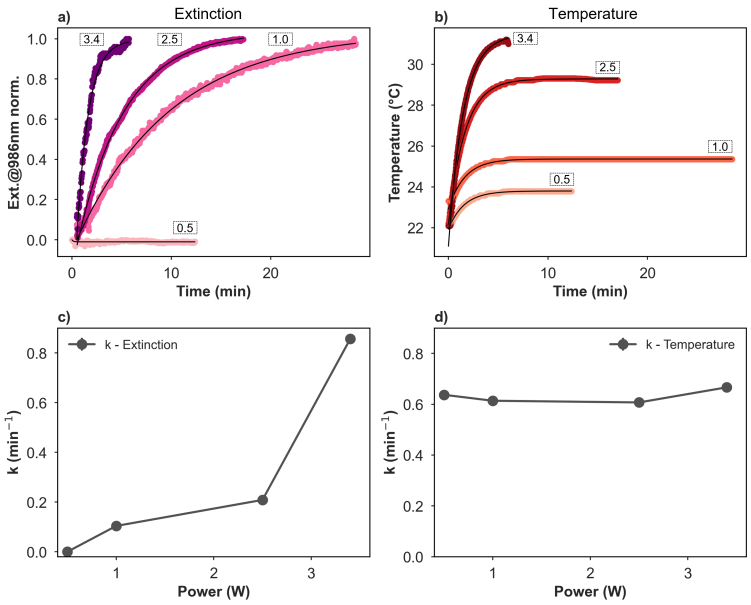

Figure 4.4.9: Photothermal redispersion at different laser powers. a) Normalized extinction at 986 nm versus time at different laser power (numbers). B) Temperature change versus time with increasing laser power. Data were fitted with exponential function $y = A - be^{-kx}$. c-d) Redispersion rate constant and temperature rate constant versus laser power, showing that redispersion rate constant increases with laser power while temperature rate constant remains unchanged.

To check oscillatory clustering, gold nanorods containing 50 μM CTAB and 300 mM NaCl were subjected to uninterrupted laser irradiation at power 1, 1.68 and 2.47 W. Stable oscillations were observed for 1 W laser power (Figure 4.4.10 a). Interestingly, only one dominant frequency at 5.9 min^{-1} was observed (Figure 4.4.10 b). At higher laser power (1.68 W) the frequency was shifted to 10 min^{-1}.

Although the origin of the oscillatory clustering is rather puzzling it can be explained by analyzing the change of extinction and local temperature over time for different laser powers (Figure 4.4.11). At laser power below oscillation threshold, the aggregating nanoparticles are unable to rise temperature above T_m, resulting in progressive aggregation (Figure 4.4.11 b). At laser power within oscillation conditions (Figure 4.4.11 c), the collective heating produces temperature jump to reach T_m, followed by a slow increase of extinction, particles start to redisperse.

During the slow redispersion, the effect of collective heating progressively decreases and so does the local temperature since the particles are not enough redispersed to maintain the temperature sufficiently high. Recall that photothermal effect of these nanoparticles is stronger at dispersed state as compared to aggregated state. Therefore, it is the slow kinetics of redisperision that induces the oscillations. The light acts as pump that induces slow redispersion that is not enough to undergo transition to full redispersion at which the system produces more heat. At laser power above oscillation conditions (Figure 4.4.11 c), a positive feedback mechanism

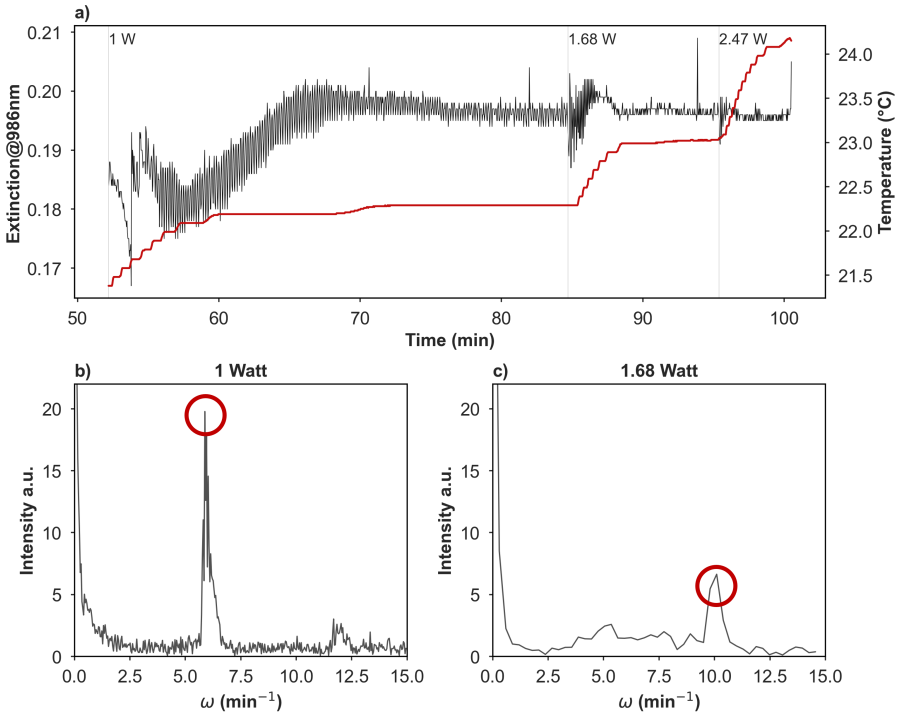

Figure 4.4.10: Oscillatory clustering under uninterrupted light laser irradiation. a) Temporal evolution of extinction at 986 nm and global temperature. Numbers indicate laser power. b) FFT analysis of extinction under 1W laser power showing a pronounced peak at 5.9 min^{-1}. c) FFT analysis of extinction under 1.68 W showing single peak at 10 min^{-1}.

dominates: with decreasing absorbance, the collective heating dominates causing temperature jump which is further augmented by fast redispersion of nanorods and the increase of absorbance at 1064 nm. The fast redispersoin causes a fast transition from dominating collective heating to the heat production by individual particles in dispersed state (larger absorbance at 1064 nm). As a results, the system is capable of generating sufficient heat to maintain its own redispersion.

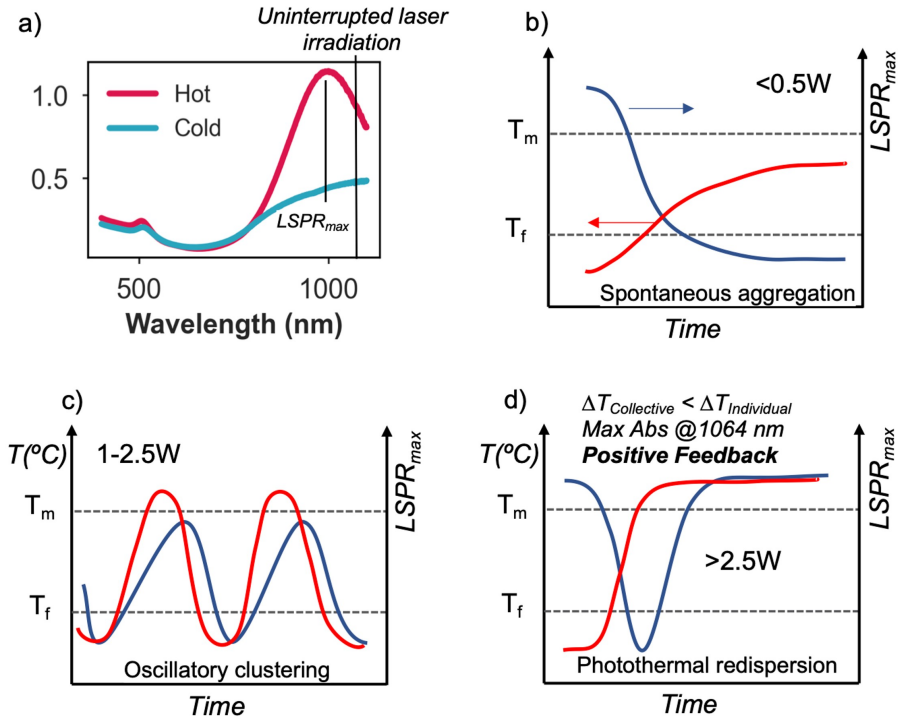

Figure 4.4.11: Mechanism of oscillatory clustering driven by slow redispersion kinetics. a) UV-Vis-NIR spectra of aggregated and redispersed nanoparticles. b) Power laser below oscillation threshold. c) Power laser within oscillation conditions where the redispersion is compromise by slow aggregation kinetics, leading to back aggregation. d) Power laser above oscillation conditions. Redispersed nanoparticles produce sufficient heat to maintain their colloidal stability and prevent aggregation.

4.5 Conclusions

In this chapter, it was shown that careful interplay between light interaction with spontaneously aggregating nanoparticles can lead to the oscillatory clustering of gold nanoparticles when subjected to uninterrupted laser irradiation. The central hypothesis indeed was confirmed showing that the change of optical properties of gold nanorods under clustering changes the way these particles transduce the light energy into heat, altering thus the local environment (temperature) which in turn modifies the way the particles interact with light. As a results, a rather exotic and unexplored behavior emerges known as self-oscillations.
The use of real-time analytics (extinction and temperature) during reversible clustering under light conditions allowed to draw the following specific conclusions:

- Laser light is a suitable physical stimulus to induce reversible clustering under ON/OFF states.

- The temperature at which the transition from aggregation to redispersion takes place is downshifted by nearly 10 °C when laser heating is used instead of bulk

heating, meaning that the local temperature close to particles surface is higher than temperature measured globally.

- The redispesion rate constant increases with laser power while temperature rate constant remains unchanged, indicating that extinction measurements resolve events down to nanoparticles level (small interparticles distances) while temperature measurement is sensitive only to global changes.

- To observe oscillatory clustering of gold nanoparticles under photothermal conditions, one needs to assure the presence of thermal hysteresis within the system.

- Cooperativity between collective heating and light absorption at laser irradiation imposes a negative feedback mechanisms under which self-oscillations take place.

- Antagonistic effect between collective heating and light absorption at laser irradiation imposes a positive feedback mechanisms that cancel self-oscillation. The oscillation then are driven by temporal lag between temperature and extinction change.

The present experimental system is unable to resolve local temperature change, and therefore cannot provide a full description of a phase portrait (change of extinction versus change of local temperature). Such a description would be an ultimate and infallible proof for oscillatory clustering. A convenient strategy for getting an insight on the local temperature change under irradiation is the use nanothermometers for example quantum dots or fluorescent dyes which exhibit temperature-sensitive emission or lifetime of excited states. Of course, if the measurement of extinction and global temperature in real time, as shown above, is already non-trivial from a technical point of view, further complexification of the system by introducing nanothermometer is even more challenging. The use of other thermoresponsive molecular shell (DNA or p-NIPAM) is probably an option, but relative large inter-particles distances by using these macromolecular system can compromise collective heating and thus kinetics of the system. An interesting direction for future exploitation of oscillatory clustering is the measurement of the system down to single cluster level, where the velocity and position of the particles can be precisely determined in real time and thus interparticle forces. In doing so, an advance characterisation techniques such as liquid-cell electron microscopy is probably the right experimental platform to study self-oscillations.

4.6 Experimental Methods

4.6.1 Oxidative Etching of AuNRs

Concentrated AuNRs@CTAB (400 μL, Au_0 = 2.5 mM) stock solution was diluted with CTAB (9.6 mL, 100 mM) to a concentration of 1 mM Au_0. AuNRs solution was stirred slowly at 30 °C and $HAuCl_4$ solution (100 μL, 1 mM) was added every 20 minutes. Before every addition a small aliquot (5 μL) was extracted for UV-Vis-NIR measurement (Figure 4.6.1 a.) These steps were repeated until the desired optical properties were obtained. Then, AuNRs solution was centrifuged at 1100 rpm for 30 minutes , the supernatant removed and AuNRs redispersed with 1 mM CTAB solution. Centrifugation was repeated three times. AuNRs dimensions were measure before and after oxidation and revealed slight reduction of length from 68.6 ± 8.2 nm to 65.69 ± 7.59 nm, while the width remained constant at ∼ 17 nm Figure 4.6.1 b). Aspect ratio was reduced from 4.02 ± 0.6 to 3.82 ± 0.55 and the polydispersity was significantly reduced.

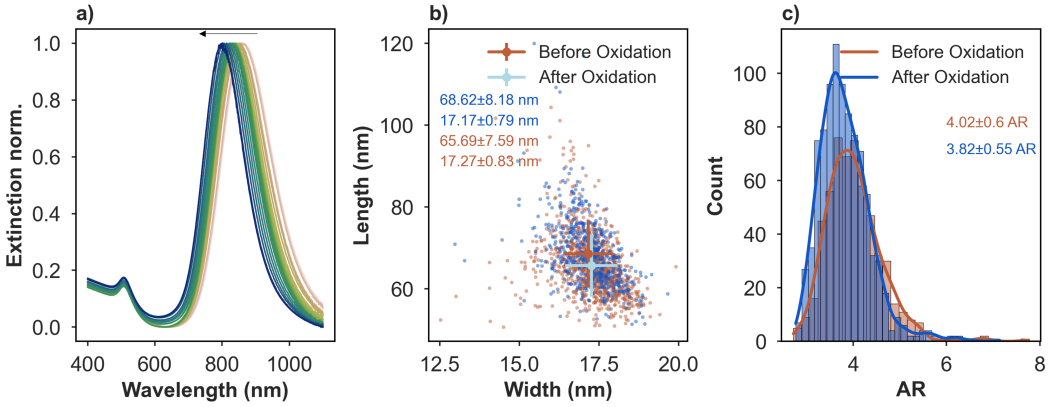

Figure 4.6.1: Au(III) assisted oxidation of AuNRs stabilized with CTAB. a) UV-Vis-NIR spectra after every $HAuCl_4$ addition. b) TEM analysis of AuNRs before and after oxidation. c) Aspect ratio before and after oxidation

4.6.2 Plasmonic heating of gold nanorods

AuNR@BSPP aggregation was characterized using a MayaPro 2000 (Ocean Optics) equipped with a tungsten/halogen light source. A quartz cuvette (1x1 cm) was mounted in qpod 2e cuvette holder (Quantum Northwest) and connected via 200 μm optical fibers to the light source and the spectrometer. The temperature of the cuvette holder was controlled with an integrated peltier element and. The temperature of the cuvette holder and inside of the cuvette were recorded with a temperature logger equipped with thermocouple (Thorlabs). The sample was illuminated in orthogonal direction to the UV-Vis-NIR measurement with a fiber coupled infrared

laser (λ = 1064 nm, ω = 500 kHz). The laser spot was enlarged with a collimator lense to 0.5 cm in diameter.

4.7 Appendix

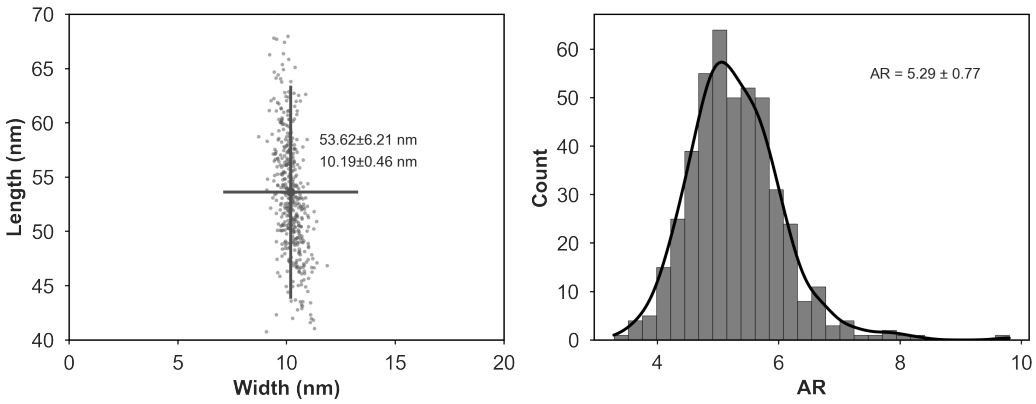

Figure 4.7.1: TEM analysis of AuNRS986

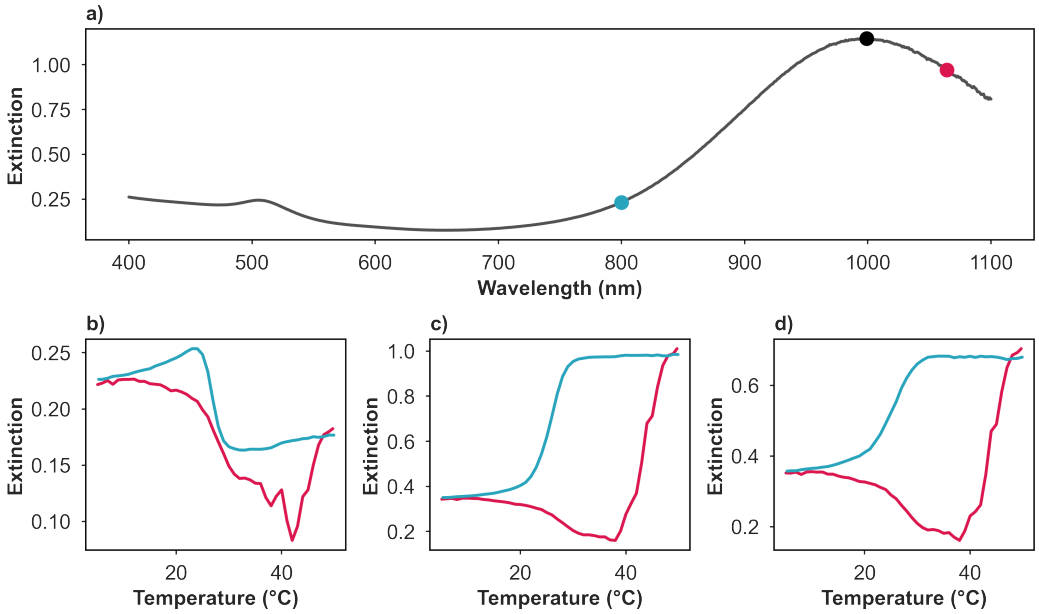

Figure 4.7.2: Thermal analysis at different wavelengths at 0.2 °C/min. a) UV-Vis-NIR spectra of dispersed AuNRs986. Colored dots show the followed wavelength. b) - d) shows thermal cycling at 800, 986 and 1064 nm respectively.

CHAPTER 5

Coupling reversible clustering of gold nanoparticles with chemothermal process

5.1 Introduction

The previous chapters showed that reversible clustering of gold nanoparticles can be controlled by two types of thermal stimuli: bulk heating using a thermostat of programmable temperature and laser heating of programmable power. In the field of nanoparticles self-assembly, these two kinds of thermal stimuli are the most exploited ones. In the present chapter a question has been imposed whether one can use yet another type of stimulus to regulate local temperature and couple that temperature to reversible clustering of gold nanoparticles.

In many biological processes, a temperature change due to a chemical process typically triggers a structural change of macromolecules, inducing a series of more complex events (e.g., signaling). For example, temperature-sensitive ion channels in can alter membrane potential at given temperature, resulting in inhibition or stimulation of the whole neural network.

Therefore controlling the state of given synthetic nanosystem through temperature using exothermic chemical reaction as a trigger is an appealing, yet poorly addressed, scenario for constructing complex chemical networks over different length scales. The difficulty in fabrication of such systems is based on the fact that temperature change is sensitive to the reagents concentration and kinetic parameter of chemothermal process. Also, accumulation of waste - products of chemothermal reactions - can interfere with the nanosystem functioning. Thus, the coupling of thermoresponsive nanosystems (e.g., aggregating nanoparticles) with temporally changing temperature through chemical reaction is challenging from experimental point of view, but with great potential for the use in chemical actuators.

From a broader perspective, chemically controlled state of give nanosystem is usually classified as "fuel-driven", where metastable supramolecular constructs feature an uphill energy consumption at the expense of energy flux from fuel.[144] Over last decade, several important works have been devoted to such a process where upon chemical stimulus (small molecules, proteins) the formation of supramolecular assemblies (micelles, [145] vesicles,[146] fibers,[147] discrete nanoparticle clusters,[148] and supercrystals[149]) rendered transient luminescence,[150, 151] gelation,[152, 153] or even catalytic properties. [146, 154, 155]
Recently, nanoparticles have attracted attention as building blocks of nanosystems with transient optical properties including reflectance, [156] absorption,[145] or fluorescence[157]. The experiments evidence the possibilities for conceptually new properties of such systems as selective signal generation,[158] aggregation pathway,[80] or self-sorting[159]. Although recent progress suggests new opportunities in fabrication of smart nanosystem, in the fuel-driven nanoparticles clustering the use of chemical stimulus to control thermoresponsive nanosystem state has been barely addressed.[160]
It is commonly known that radially distributed DNA strands on nanoparticles surface are sensitive to external temperature, allowing for a precise transition between double and single-stranded conformations that in turn determines colloidal phase (dispersed vs. aggregated).[161] Again, the question was imposed whether a reversible transition from double to single-stranded DNA can be coupled to chemothermal reaction - fed by fuel - that would result in a scenario where nanoparticles maintain their colloidal stability as long as the fuel is available.

5.2 Hypothesis

(Figure 5.2.1) shows a hypothetical design in which at room temperature, the lack of electrostatic repulsion drives the clustering of DNA coated gold nanoparticles (AuDNA) by the hybridization of free DNA strands (clustering DNA) with the ones anchored to the metal surface (redispersion DNA). The presence of fuel and catalyst triggers chemothermal reaction that raises the temperature of the mixture above DNA melting point (T_m), leading to its dehybridization and redispersion of nanoparticles. The consumption of fuel brings the temperature back to the initial values, letting the particles to cluster below freezing temperature (T_f). Overall, the cyclic execution of such process leads to the transient clustering of nanoparticles sustained by chemical reaction. To resolve the coupling of temperature change and transient nanoparticles clustering real-time analytics of sufficient temporal resolution are required.

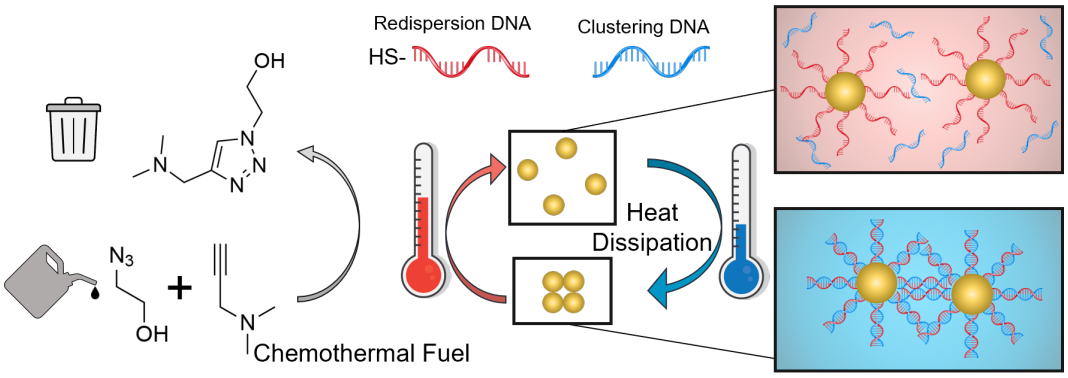

Figure 5.2.1: Coupling exothermic copper-catalyzed azide-alkyne cycloaddition reaction with thermally-responsive DNA-coated gold nanoparticles. Below melting temperature, the hybridization of "redispersion" and "clustering" DNA causes a spontaneous aggregation of gold nanoparticles. A sudden increase of temperature upon the addition of fuels (azide and alkyne) brings DNA duplex above melting temperature resulting in melting of redispersion and clustering DNA and thus redispersion of nanoparticles. Once the fuel is consumed, both DNA strand hybridize again, leading to spontaneous clustering of nanoparticles.

5.3 System design

Copper-catalysed azide-alkyne cycloadditions (CuAAC) was selected as a convenient chemothermal process.[162] This reaction involves the use of catalyst, Cu(I)[tris(3-hydroxy-propyltriazolylmethyl)amine] (Cu(I)-THPTA) and water-soluble fuel molecules, namely 2-azidoethanol and 3-dimethylaminopropyne(Figure 5.2.1)[163]. As a thermoresponsive nanosystem, DNA-coated gold nanoparticles were selected.[62] Of course, the thermoresponsive system based on BSPP (developed in the previous chapters) was, in fact, selected as a primary choice. However, BSPP molecules revealed incompatibility with CuAAC reaction since phosphine present in BSPP can rapidly complex copper ions and therefore inhibits the whole chemothermal process. Thus an alternative thermoresponsvie system, based on DNA, was selected since DNA, being a biological molecules, are chemically robust and can stand relatively high ionic strength.

5.3.1 DNA-coated gold nanoparticles

Colloidal gold was synthesized by Bastus method[40] producing nanoparticles of 26.6 ± 3.3 nm in diameter (Figure 5.3.1). The as-prepared gold nanoparticles were functionalized with DNA through well-known salt-ageing method[164]. Table 5.1 shows full list of DNA sequences used to stabilize and cluster gold nanoparticles. UV-Vis spectra before and after the functionalization with DNA sequence show a shift of the plasmon from 525 to 529 nm, indicating successful ligand exchange. DLS analysis confirmed such statement by showing the increase of hydrodynamic

diameter from 34.6 ± 0.2 nm for citrate-stabilized to 50.9 ± 0.6 nm for DNA-coated.

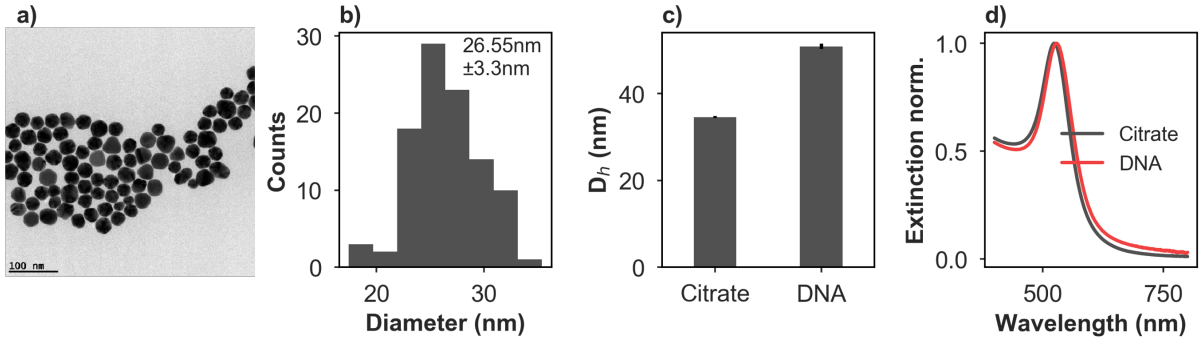

Figure 5.3.1: a) Transmission electron micrograph of initial spherical nanoparticles. b) Size distribution of gold nanoparticles. c) The change of hydrodynamic diameters of citrate and DNA-stabilized gold nanoparticles. d) UV-Vis-NIR spectra of nanoparticles before and after the functionalization with DNA, showing a red-shift of LSPR by 4 nm.

Name	Oligonucleotide Sequence (5' to 3')	T_m
Redispersion DNA	SH-Spacer18-TTA-ATA-TGA-GTC-GTT	38 °C
Clustering DNA	AAC-GAC-TCA-TAT-TAA	38 °C

Table 5.1: Sequences of DNA stabilising nanoparticles (Redispersion DNA) and complementary DNA inducing spontaneous clustering (Clustering DNA). Calculated melting temperatures are also provided. The redispersion DNA was modified at the 5'-end with a thiol group followed by a polyethylene-glycol spacer followed by the nucleotide sequence (SH-Spacer18-nucleotide sequence).

5.3.2 Chemothermal reaction

Generally, CuAAC are highly specific chemical reactions between an azide and an alkine to 1,2,3-triazoles catalyzed by Cu(I). 1,2,3-triazoles are highly inert against redox reactions or hydrolysis, which renders them ideal as waste product, because they will not participate in undesired side reactions[165].

The activation of copper catalyst is based on reduction of Cu(II) to Cu(I) in-situ by the fuel molecules through alcohol oxidation or alkyne oxidative homocoupling.[166] Upon the reduction of Cu(II) to Cu(I), a blue-coloured initial mixture typically turns colourless, decreasing the absorbance in 600 - 900 nm spectral range. This is a desired effect since upon the reduction, the optical window gets wide enough for monitoring the change of optical feature of clustering gold nanoparticles (Figure 5.3.2a, e).

To couple colloidal clustering and chemothermal reaction one needs to carefully optimize the range of concentrations of Cu-THPTA and fuel. It was found, that with increasing Cu-THPTA concentration (2, 4, 8 mM) the heating rate of the solution

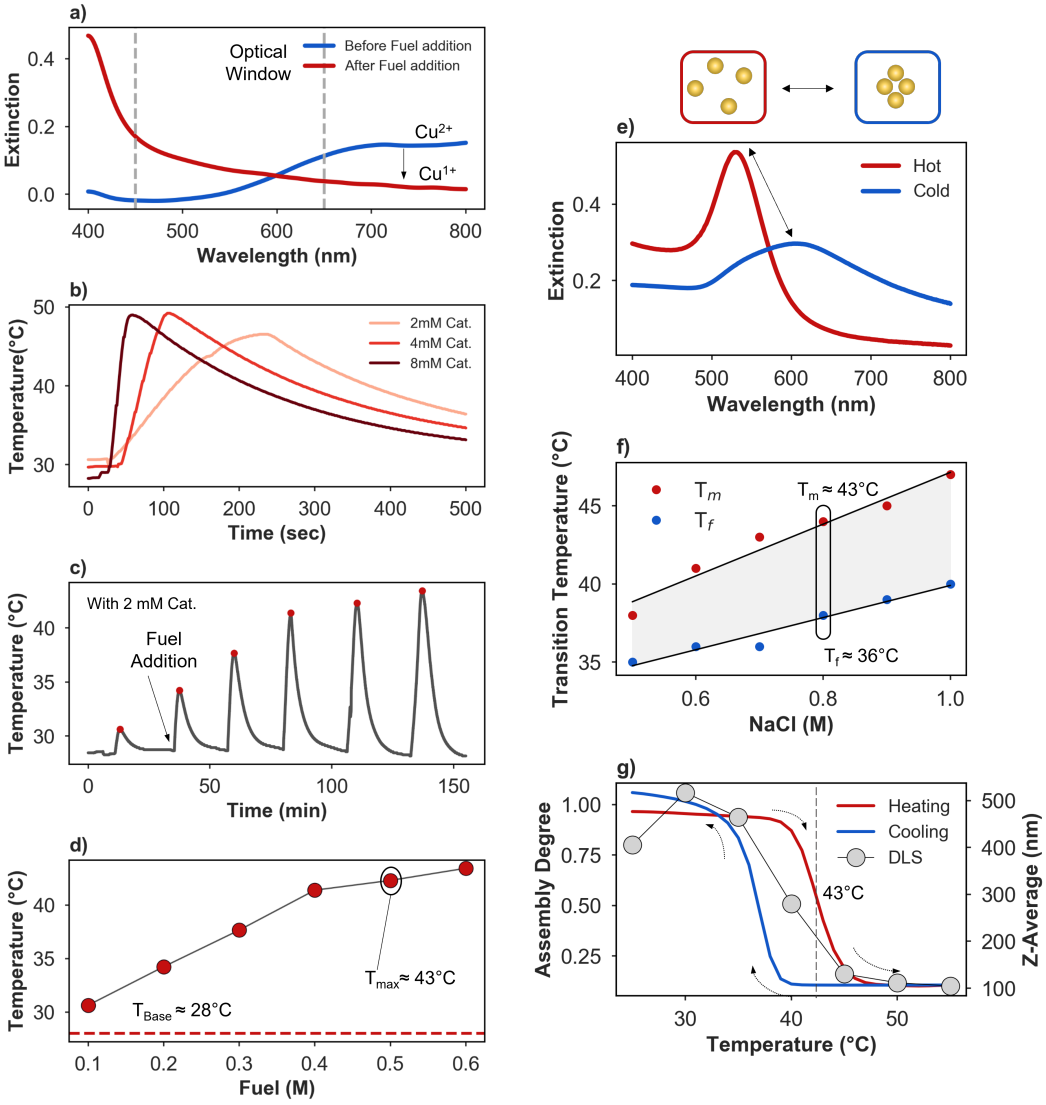

Figure 5.3.2: Optimisation of CuAAc reaction (left panel) and reversible clustering of DNA-coated gold nanoparticles (right panel). a) Decrease of absorbance during activation of copper catalyst (reduction of Cu(I) to Cu(II)) to render an optical window for monitoring optical changes during reversible clustering of DNA-coated gold nanoparticles. b) Effect of catalyst concentration on the temporal evolution of temperature. c) Temporal profile of temperature upon cyclic addition of fuel. d) Maximum temperature recorded at each fuel addition in c). e) UV-Vis-NIR spectra of aggregated (blue, low temperature) and dispersed (red, high temperature) AuDNAs. f) Change of DNA melting and freezing temperature versus NaCl concentration. Grayed area indicates the presence of thermal hysteresis at 1 °C/min scan rate. g) Change of optical properties (Assembly degree = Abs650/Abs520) of DNA-coated gold nanoparticles during heating (upper, red) and cooling (lower, blue) and DLS data (gray dots) at 0.7 M NaCl.

increased but without having an impact on the maximum temperature reached, being in the range of 2.5 °C (Figure 5.3.2 b). Thus, the concentration of Cu-THPTA was set to 2 mM, allowing to minimize the optical interference with the solution of gold nanoparticles and, from the other hand, assuring sufficient temperature increase

to dehybridize DNA on nanoparticles surface (*vide infra*). A progressive increase of a fuel dose from 0.1 to 0.6 M in the interval of 0.1 M (at 2 mM catalyst) led to a steady increase of temperature peak from 31 and 45°C at a base temperature of 28 °C (Figure 5.3.2 c, d). The results corroborate well with previous work from Muradyan et al.[162], showing that catalyst concentration controls the heating rate, while the fuel concentration dictates the maximum temperature.

Once the concentration range of chemothermal reaction was optimized the focus was put on optimizing the concentrations related to the reversible clustering of DNA-coated nanoparticles, that is to assure that nanoparticles cluster spontaneously in the presence of free complementary DNA strands (clustering DNA). The mechanism of reversible clustering is based on surface charge neutralization. That is, at low temperatures, below T_f, the hybridization of both DNA neutralize surface charge, decreasing the electrostatic repulsion and thus inducing progressive aggregation (blue spectrum in Figure 5.3.2 e). Above T_m, the melting of double strands on the nanoparticles surface led to their redispersion (red spectrum in Figure 5.3.2 e).

The benefit of using free complementary DNA to aggregate nanoparticles is two-fold: rapid aggregation kinetics and low melting temperatures.[167] This is because the aggregation of nanoparticles is driven by the change of electrostatic repulsion instead of the hydrogen bond formation between adjacent nanoparticles. In such scenario one can use very short DNA strands, only 15 base pairs, allowing thus for reaching a small value of $T_m \sim 40$ °C.

Likewise in BSPP-based reversible clustering, DNA-driven clustering is sensitive to ionic strength (NaCl concentration) which alter melting temperature. To check the effect of ionic strength on particles clustering, assembly degree (abs@650 / abs@530nm) was measured at up and down temperature scans (1 °C/min) for NaCl concentration ranging from 0.5 to 1 M. A linear increase of 1.6 °C/100 mM NaCl for T_m and 1 °C/100 mM NaCl for T_f (Figure 5.3.2 e) was revealed. A full analysis for estimating melting temperature is provided bellow in Appendix of the present chapter (Figure 5.7.1). The optimal salt concentration was found to be 0.7 M, allowing for a melting temperature at 43 °C.

Interestingly, the aggregation T_f and redispersion temperature T_m of AuDNA showed thermal hysteresis (grey area in Figure 5.3.2 f), a typical signature of thermosensitive nanosystems, as shown in the previous chapters.

Optimal concentration of clustering DNA was 250 nM, which is in large excess to immobilized redispersion DNA, allowing for the aggregation within minutes at room temperature and immediate redispersion at 40 - 45 °C (Figure 5.3.2 g, red line). Dynamic Light Scattering measurements further indicated that hydrodynamic diameter of the clusters decreased from 500 to ∼100 nm at 40 - 45 °C (Figure 5.3.2 g,

grey dots). Finally, under optimized conditions, the thermal redispersion of AuDNA required 0.8 M of fuel to reach T_m = 43 °C (Figure 5.3.2 d, g).

5.4 Coupling chemothermal reaction and reversible clustering of DNA-coated gold nanoparticles

To monitor chemothermal transient clustering of AuDNA, both UV-Vis-NIR and temperature data were recorded simultaneously (Figure 5.4.1). The sample was prepared in a disposable PMMA micro cuvette (850 μL) and placed in CUV-ALL-UV cuvette holder (Ocean Optics) connected via 200 μm optical fibers to the tungsten/halogen light source and the spectrometer (MayaPro 2000, Ocean Optics). The temperature of the cuvette holder was controlled with a heating plate (LINKAM). The temperature of the sample was recorded with a temperature logger equipped with thermocouple (Thorlabs), which was placed inside the solution, slightly above the light beam to not interfere with the UV-Vis-NIR signal. UV-Vis-NIR and temperature data were recorded every five seconds. In each experiment, nearly 5000 spectra were recorded.

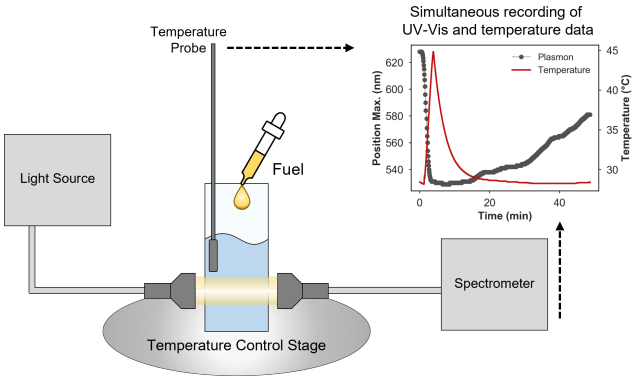

Figure 5.4.1: Experimental Setup for monitoring in real time how chemothermal reaction affects reversible clustering of DNA-coated gold nanoparticles.

Figure 5.4.2b shows an experimental outcome of temperature (red) and wavelength of LSPR (black) acquired simultaneously.

A typical experiment commenced with a stable AuDNA dispersion (LSPR = 530 nm and 28 °C base temperature) with the excess of free clustering DNA (Figure 5.4.2, stage I). Increasing the concentration of NaCl to 0.8 M induced the hybridization of both complementary DNA and thus aggregation of nanoparticles that was confirmed by progressive redshift of LSPR to ~ 650 nm (Figure 5.4.2, stage II). Clustering was also confirmed with time-resolved DLS measurement showing that cluster size stabilizes at 400 nm after 25 minutes (see Appendix of the present chapter: Figure 5.7.2). At the end of stage II, upon addition of Cu(II)-THPTA catalyst a band at 700 nm

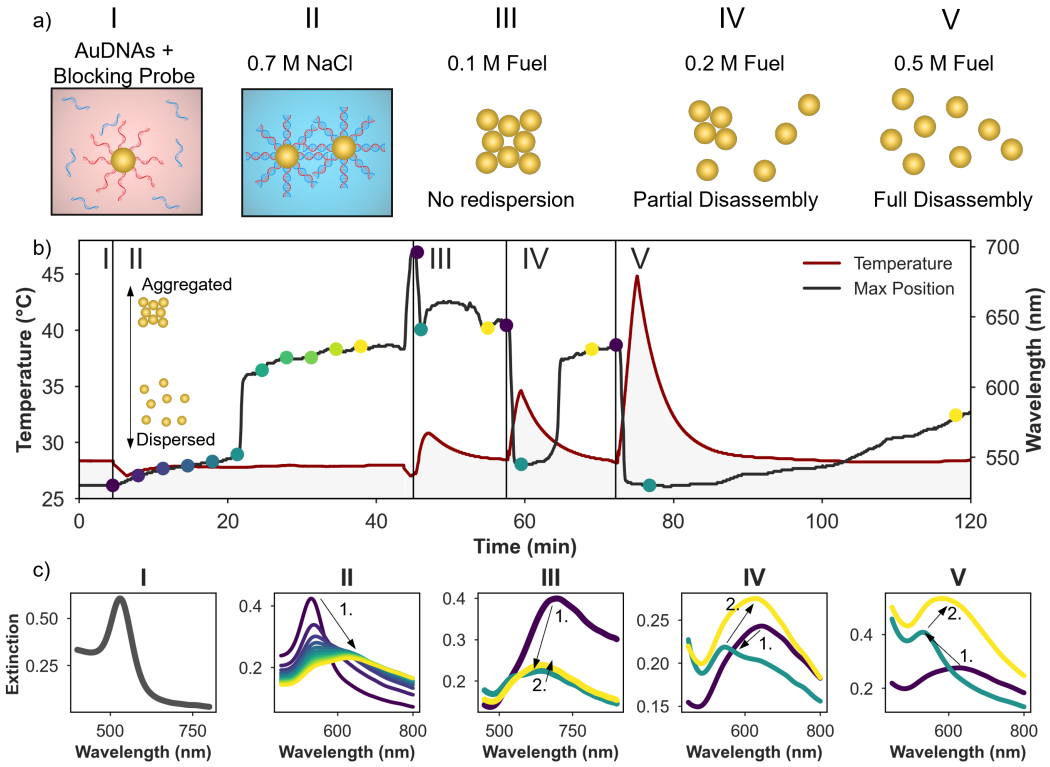

Figure 5.4.2: Real-time monitoring of chemothermal transient clustering of AuDNAs. (a) Schematic description of each step step in transient clustering process. (b) Real-time monitoring of LSPR and temperature change. (c) Selected spectra extracted from (b) marked with color codes at their respective phase. (I) AuDNA remain stable in the presence of clustering DNA. (II) Ionic strength is increased (0.8M NaCl) inducing clustering. (III) Cu-THPTA catalyst and low dose of fuel (0.1 M) are added with no effect on aggregates integrity. (IV) Intermediate fuel dose (0.2 M) leads to partial redispersion. (V) Large fuel dose (0.5 M) induces complete redispersion of gold nanoparticle.

emerged corresponding to copper present in the solution. Injection of fuel (0.1 M) induced rapid reduction of Cu(II) to Cu(I) that was manifested by the decrease of absorbance in 700 - 900 nm (Figure 5.4.2 c, stage III). Immediately after, the temperature increased to 31 °C, but being below T_m AuDNAs remained aggregated. After total consumption of fuel and temperature stabilization, a new portion of fuel (0.2 M) was added, resulting in a temperature increase to 35 °C. The maximum of LSPR blue-shifted from 650 nm to 540 nm, indicating partial redispersion of nanoparticles (Figure 5.4.2 a, stage IV). A closer inspection of UV-Vis-NIR spectra in Figure 5.4.2c-IV (green line) revealed two distinct bands, suggesting the presence of dispersed and clustered nanoparticles.

This behaviour is in agreement with temperature-controlled UV-Vis-NIR and DLS measurement in Figure 5.3.2 g, where partial redispersion was observed at $\sim$ 35 °C. At the highest fuel concentration (0.5 M) the temperature increased to 45 °C, causing complete redispersion of AuDNAs (Figure 5.4.2, stage V). The maximum of

LSPR blueshifted to 530 nm, reaching the value of initially stable AuDNA, followed by aggregation due to fuel consumption and temperature drop below 30 °C.

Notice rather slower aggregation kinetics in stage V, which is due to the dilution effect. The total concentrations of NaCl, AuDNA and blocking probe in the mixture dropped by 14 %, respectively, altering aggregation kinetics. In summary, these results show that indeed exothermic chemical reaction can be coupled with DNA-driven clustering of nanoparticles.

It is worth mentioning that the coupling of a molecular and colloidal system is sensitive to the order of addition of each component because of the possibility for interference (and cooperative effects) that can alter the course of the whole process. It was found that Cu(II)-THPTA solution needs to be added to fully aggregated nanoparticles since the presence of Cu(II) can interfere with the hybridization of both DNA strands. Also, fuel needs to be added after the catalyst addition. This is because an excess of 2-azidoethanol can disintegrate the clusters due to non-specific intercalation of small molecules with double-helix.[168] (Figure 5.4.3). Thus, the injected 2-azidoethanol to the solution can either react with Cu-THPTA catalyst (desired scenario) or bind to DNA altering cluster integrity (undesired scenario). In the present conditions, the former process is favoured since the concentration of Cu-THPTA is 8000 times higher than that of available DNA.

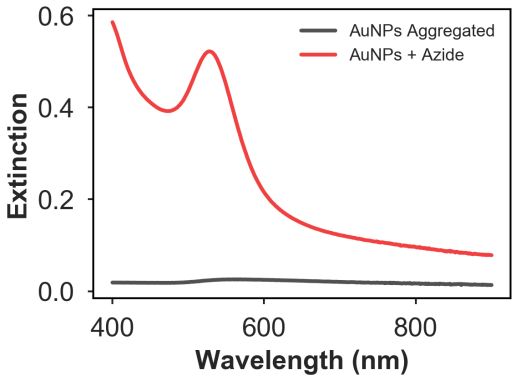

Figure 5.4.3: Clusters stability in the presence of fuel molecules. UV-Vis-NIR of spectra aggregated nanoparticles (black line) and after an addition of excess 2-azidoethanol (red line).

An eventual interference of 2-azidoethanol with DNA and Cu-ions can cause non-selective aggregation of nanoparticles. The coupling of chemothermal reaction and aggregation process was tested in the absence of free clustering DNA. In such scenario, the duplex formation is excluded and nanoparticles should remain stable independent on the concentration of added fuel. It was observed that LSPR blueshift at changing chemical environment, but its magnitude was substantially lower as compared to the shift observed in the presence of blocking (Figure 5.4.4). Therefore, it was concluded that temperature is the main driving stimuli inducing reversible clustering of gold nanoparticles, still observing a minor effect of non-thermal events that can interfere with the aggregation of nanoparticles.

Finally, to confirm that thermochemical process is coupled with transient aggregation of nanoparticles a phase plot was prepared by removing time component

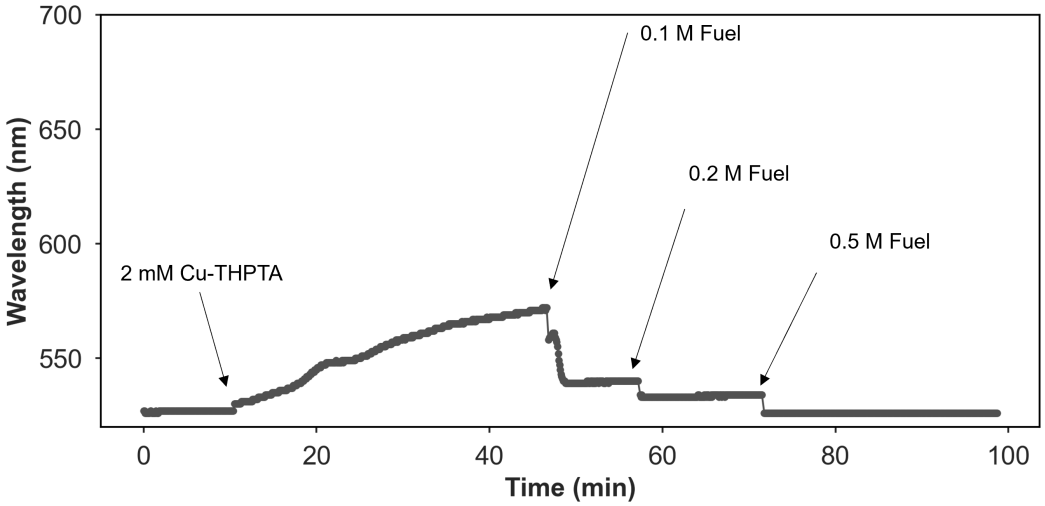

Figure 5.4.4: The change of LSPR maximum during chemothermal reaction of AuDNA without free clustering DNA. After each dose of fuel, there was no redshift of LSPR observed suggesting that in the absence of free clustering DNA no aggregation of particles occurs.

from Figure 5.4.2. Figure 5.4.5 shows the results of such analysis. It was observed that below the concentration threshold of fuel the plasmon band position remains stationary at larger wavelengths since the temperature varies only 3 °C.

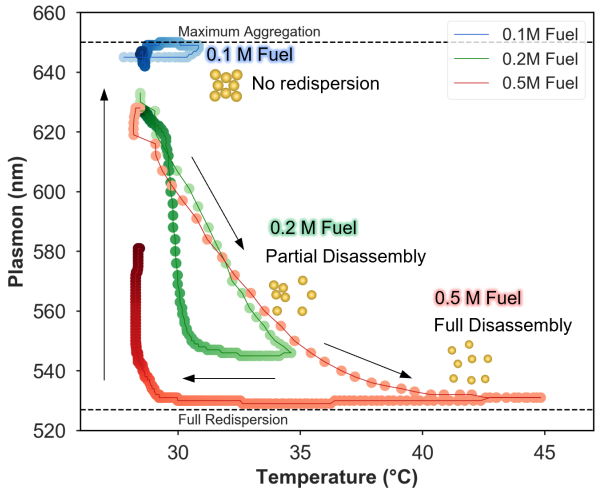

Figure 5.4.5: Phase plot extracted from Figure 5.4.2 and representing the trajectory of plasmon band position and temperature for the fuel concentration from 0.1, 0.2 to 0.5 M. The horizontal lines indicate the limiting value of LSPR. The phase portrait confirms the presence of hysteresis in temperature-driven redispersion/aggregation of nanoparticles. While the redispersion follows temperature profile, the aggregation commences only after freezing temperature is reached.

For higher fuel concentrations (0.2 and 0.5 M), the initial shift of the LSPR band followed similar paths but reached different minimums: 540 nm and 530 nm, respectively. In the backward process, during the temperature drop the LSPR maximum remains initially stable, but once the onset T_m is reached there is a continuous

red-shift of LSPR, indicating the recovery of the initial aggregated state. This analysis shows that aggregation and redispersion display a hysteresis, because of the difference in aggregation/redispersion kinetics. In contrast to aggregation, the redispersion is able to follow a fast heating rate, resulting in a substantial lag.

5.5 Conclusions and Outlook

The results from the present chapter can extent the list of current thermal stimulus used to cluster nanoparticles. Apart from bulk or laser heating one can use copper-catalyzed click-reaction to increase locally the temperature and thus alter the colloidal state of nanoparticles. The successful coupling of exothermic reaction with thermosensitive DNA-coated gold nanoparticles led to their transient stability. The extent extent of such coupling can be controlled with the amount of fuel added. It was found that interfering effects on the colloidal stability of fuel and catalyst could be controlled by controlling the order of reagent addition. Further sophistication of this system is foreseen by using, for example, gold nanoparticles coated with DNA strands of different melting temperatures or using bimetallic gold-copper nanoparticles[169] to exclude the need for copper ions and minimize waste production.

5.6 Methods and Materials

5.6.1 Materials

Sodium citrate, sodium chloride, and tetrachloroauric(III) acid, tris(3-hydroxy- propyltriazolylmethyl)amine (THPTA), sodium dodecyl sulfate, phosphate buffer 3-bromopropanol and $Cu(OAc)_2$ were purchased from Sigma-Aldrich and used without any further purification. DNA sequences were purchased from Biomers. All glassware was cleaned with aqua regia and rinsed thouroughly with Milli-Q water.

5.6.2 Synthesis 2-azidoethanol

2-azidoethanol was synthesized following the procedure described by Choi et al[170]. It should be noted that lower molecular weight organoazides are explosive and should be handled with caution! The synthesis was performed on a multigram scale (1-3 g) and no explosion was encountered.

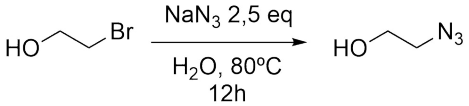

Sodium azide (3.12 g, 47.98 mmol, 2.5 equiv.) was cautiously weighed using a plastic spatula into a round bottom flask equipped with a stir bar and then 28.7 mL distilled water was slowly added. 2-Bromoethanol (2.40 g, 19.16 mmol, 1 equiv.) was drop-wise added at RT. The mixture was heated to 80 °C for 12h. The reaction mixture was cooled to RT. To this mixture was added diethyl ether, and then, it was transferred to a separatory funnel for extraction (3x25 mL). The combined organic layers were dried over $MgSO_4$, filtered and concentrated under vacuum. The isolated yield for 2-azidoethanol was 81%. ^{1}H NMR or ^{13}C NMR spectra were recorded at 400 and 101 for ^{13}C NMR, equipped with a z-gradient BBOF probe, in $CDCl_3$. The data are reported as s = singlet, d = doublet, t = triplet, m = multiplet or unresolved, br s = broad signal, coupling constant(s) in Hz, integration. ^{1}H NMR (400 MHz, $CDCl_3$, 298 K) δ 3.80 – 3.73 (m, 2H), 3.48 – 3.39 (m, 2H), 2.80 (dd, J = 6.2, 3.3 Hz, 1H). ^{13}C NMR (101 MHz, $CDCl_3$) δ 61.36, 53.47, 50.72.

5.6.3 Synthesis of 27 nm gold nanoparticles, DNA functionalization and characterization

Following a seeded growth method[40], the synthesis of the Au seeds was performed with trisodium citrate solution (150 mL, 2.2 mM) heated for 15 min under vigorous stirring until boiling, followed by the injection of $HAuCl_4$ (1 mL, 25 mM). Under these conditions, the colour of the solution changed from yellow to bluish grey and then to light pink in 10 min. Thereafter, the seeded growth process comprised cyclic addition of metal precursor and nanoparticles extraction, by cooling to 90 °C and then adding $HAuCl_4$ (1 mL, 25 mM) in two steps 30 min apart. After additional 30 min, 55 mL of the growth solution were removed and the remaining 98 mL were mixed with water (53 mL) and sodium citrate (2 mL, 60 mM). This process was repeated 2 times to obtain nanoparticles of $\sim$ 27 nm gold core diameter.

DNA functionalization (15-mer) of gold nanoparticles was followed by Hurst et al. protocol[164]. An excess of thiolated oligonucleotides (0.1 mM) was added to AuCitrate (5.55 mL) containing sodium dodecyl sulfate (SDS) 0.1% and phosphate buffer 0.01 M, followed by incubation at room temperature for 20 min. To improve oligonucleotide binding, a salt aging process was carried out by sequential addition of 25 uL, 25 uL, 75 uL, 125 uL and 250 uL of a solution containing NaCl 2 M, SDS 0.01% and phosphate buffer 0.01 M, up to a final concentration of NaCl 0.2 M. Each salt aging step was sonicated (10 s) and incubated (20 min), and the last one was incubated for 12 h, at 25 °C. To remove the excess of oligonucleotides, the solutions were centrifuged (7000 rpm, 30 min) and re-dispersed in 2 mL of SDS 0.01%. This step was repeated three times. AuDNAs were characterised by TEM, DLS and UV-Vis, see Figure 5.3.1. For TEM, 50 uL of nanoparticles were drop

casted onto copper grid placed on filter paper and left for drying. Transmission electron microscopy (TEM) analysis was performed by JEOL JEM-1400 PLUS, operating at 120kV. The hydrodynamic diameter of AuDNA was determined by 6 measurements of DLS with 5 runs of 5 s each. The study was carried out at 25 °C with 120 s of sample equilibration.

5.6.4 Experimental setup and procedure

In a typical clustering experiment (V_{total} = 500 μL), AuDNAs (50 μL) were diluted with water (223 μL) and complimentary clustering DNA (62.5 μL, 2 μM, 250 nM final concentration. The solution was placed inside the cuvette holder and data recording (UV-Vis-NIR and temperature) was initiated. Next, NaCl (70 μL 5 M, 0.7 M final concentration) were added to the nanoparticle solution, initiating aggregation. After UV-Vis-NIR spectra stabilized, Cu(II)-THPTA (31.3 μL, 32 mM) was added and then in subsequent steps fuel mixture (9.45, 18.9 and 47 μL). Between each fuel addition, the sample was led to equilibrate followed by the removal of a portion of the mixture (equal to the volume of added fuel) prior to adding another batch.

5.7 Appendix

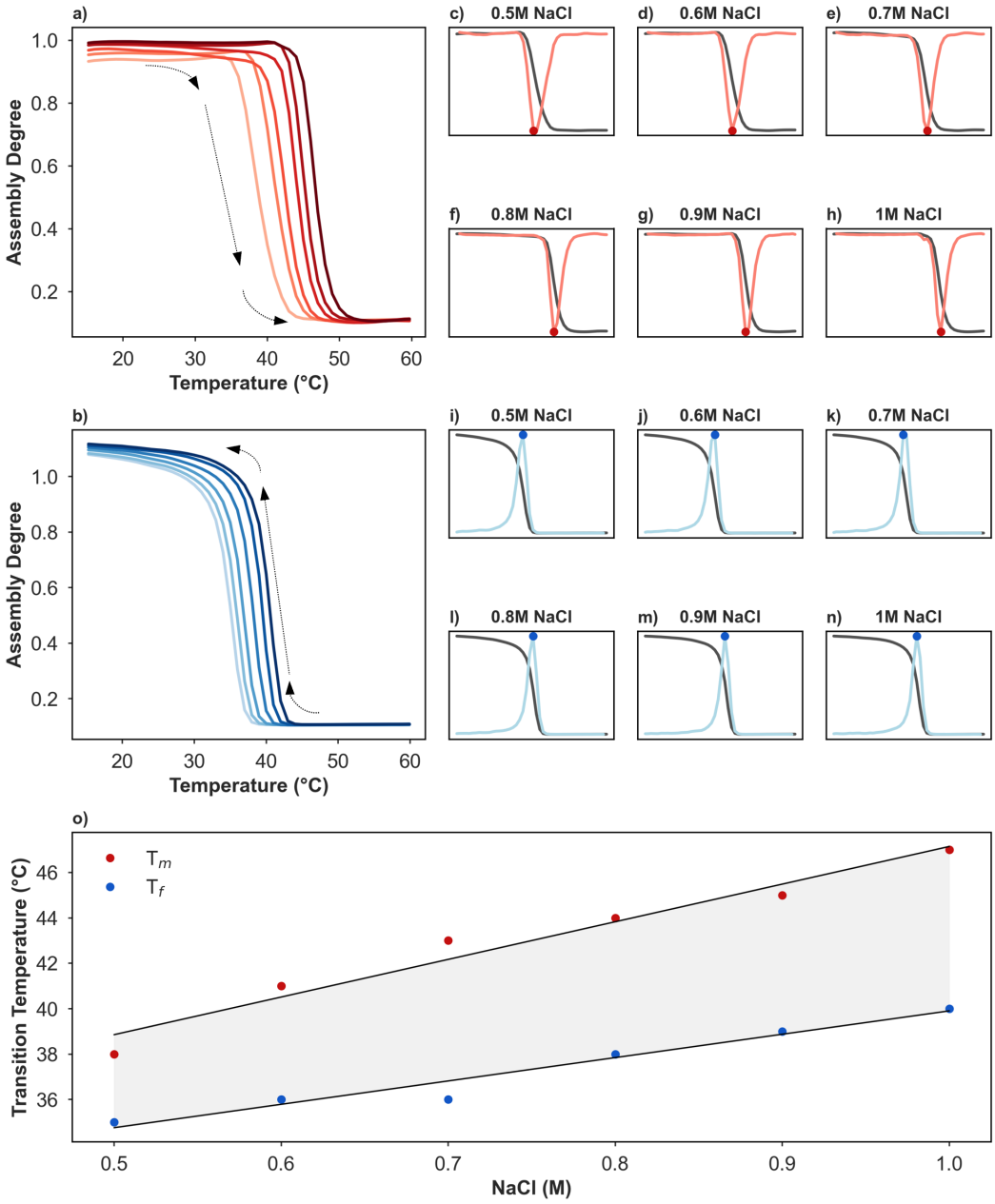

Figure 5.7.1: Determination of AuDNA transition temperatures for different NaCl concentration. a,b) Assembly Degree (abs650nm / abs530nm) was followed for heating/cooling ramp (1°C/min) between 15 °C and 60 °C. Aggregation and redispersion temperatures (c - n) were obtained by calculating the local maximum of first derivative. The resulting transition temperatures were fitted with a linear regression o).

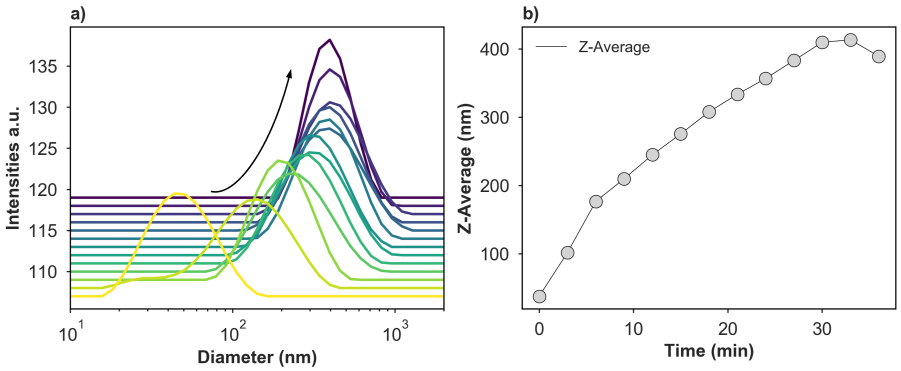

Figure 5.7.2: Time-dependent DLS measurements at based temperature of AuDNAs at 0.7M NaCl and 250 nM clustering DNA. a) Intensity weighted size distribution and b) Z-average.

Bibliography

1. Ken Shirriff. *The Surprising Story of the First Microprocessors. You thought it started with the Intel 4004, but the tale is more complicated* http://spectrum.ieee.org/tech-history/silicon-revolution/the-surprising-story-of-the-first-microprocessors.

2. Peide D. Ye, Thomas Ernst, Mukesh V. Khare. *The nanosheet transistor is the next (and maybe last) step in Moore's Law. Nanosheet devices are scheduled for the 3-nanometer node as soon as 2021* https://spectrum.ieee.org/the-nanosheet-transistor-is-the-next-and-maybe-last-step-in-moores-law (2022).

3. Vega-Vásquez, P., Mosier, N. S. & Irudayaraj, J. Nanoscale Drug Delivery Systems: From Medicine to Agriculture. *Frontiers in Bioengineering and Biotechnology* **8,** 79 (2020).

4. Karakuş, E., Erdemir, E., Demirbilek, N. & Liv, L. Colorimetric and electrochemical detection of SARS-CoV-2 spike antigen with a gold nanoparticle-based biosensor. *Analytica Chimica Acta* **1182,** 338939 (2021).

5. Shi, J., Kantoff, P. W., Wooster, R. & Farokhzad, O. C. Cancer nanomedicine: progress, challenges and opportunities. *Nature Reviews Cancer* **17,** 20–37 (2017).

6. Grzybowski, B. A. & Huck, W. T. S. The nanotechnology of life-inspired systems. *Nature Nanotechnology* **11,** 585 (2016).

7. Morowitz, H. J. *Energy flow in biology* (Ox Bow, S.l., 1979).

8. *Modern Plasmonics* (Elsevier, 2014).

9. Willets, K. A. & van Duyne, R. P. Localized surface plasmon resonance spectroscopy and sensing. *Annual Review of Physical Chemistry* **58,** 267–297 (2007).

10. *Plasmonics: Fundamentals and Applications* (ed Maier, S. A.) (Springer US, New York, NY, 2007).

11. Kreibig, U. & Vollmer, M. *Optical properties of metal clusters* 1 volume (Springer, Berlin and London, 2011).

12. Aslam, U., Rao, V. G., Chavez, S. & Linic, S. Catalytic conversion of solar to chemical energy on plasmonic metal nanostructures. *Nature Catalysis* **1,** 656–665 (2018).

13. Jain, P. K., Lee, K. S., El-Sayed, I. H. & El-Sayed, M. A. Calculated absorption and scattering properties of gold nanoparticles of different size, shape, and composition: applications in biological imaging and biomedicine. *The Journal of Physical Chemistry B* **110,** 7238–7248 (2006).

14. Jensen, T., Kelly, L., Lazarides, A. & Schatz, G. C. *Journal of Cluster Science* **10,** 295–317 (1999).

15. Zhong, Z., Patskovskyy, S., Bouvrette, P., Luong, J. H. T. & Gedanken, A. The Surface Chemistry of Au Colloids and Their Interactions with Functional Amino Acids. *The Journal of Physical Chemistry B* **108,** 4046–4052 (2004).

16. Jain, P. K., Huang, W. & El-Sayed, M. A. On the Universal Scaling Behavior of the Distance Decay of Plasmon Coupling in Metal Nanoparticle Pairs: A Plasmon Ruler Equation. *Nano letters* **7,** 2080–2088 (2007).

17. Prodan, E., Radloff, C., Halas, N. J. & Nordlander, P. A hybridization model for the plasmon response of complex nanostructures. *Science* **302,** 419–422 (2003).

18. Prodan, E. & Nordlander, P. Plasmon hybridization in spherical nanoparticles. *The Journal of Chemical Physics* **120,** 5444–5454 (2004).

19. Nordlander, P., Oubre, C., Prodan, E., Li, K. & Stockman, M. I. Plasmon Hybridization in Nanoparticle Dimers. *Nano Letters* **4,** 899–903 (2004).

20. Funston, A. M., Novo, C., Davis, T. J. & Mulvaney, P. Plasmon coupling of gold nanorods at short distances and in different geometries. *Nano letters* **9,** 1651–1658 (2009).

21. Fong, K. E. & Yung, L.-Y. L. Localized surface plasmon resonance: a unique property of plasmonic nanoparticles for nucleic acid detection. *Nanoscale* **5,** 12043–12071 (2013).

22. Inouye, H., Tanaka, K., Tanahashi, I. & Hirao, K. Ultrafast dynamics of nonequilibrium electrons in a gold nanoparticle system. *Physical Review B* **57,** 11334–11340 (1998).

23. Huang, W., Qian, W., El-Sayed, M. A., Ding, Y. & Wang, Z. L. Effect of the Lattice Crystallinity on the Electron−Phonon Relaxation Rates in Gold Nanoparticles. *The Journal of Physical Chemistry C* **111,** 10751–10757 (2007).

24. Hu, M. & Hartland, G. V. Heat Dissipation for Au Particles in Aqueous Solution: Relaxation Time versus Size. *The Journal of Physical Chemistry B* **107,** 1284 (2003).

25. Zhan, C. *et al.* From plasmon-enhanced molecular spectroscopy to plasmon-mediated chemical reactions. *Nature Reviews Chemistry* **2,** 216–230 (2018).

26. Baffou, G. & Rigneault, H. Femtosecond-pulsed optical heating of gold nanoparticles. *Physical Review B* **84** (2011).

27. Richardson, H. H., Carlson, M. T., Tandler, P. J., Hernandez, P. & Govorov, A. O. Experimental and theoretical studies of light-to-heat conversion and collective heating effects in metal nanoparticle solutions. *Nano Letters* **9,** 1139–1146 (2009).

28. Govorov, A. O. *et al.* Gold nanoparticle ensembles as heaters and actuators: melting and collective plasmon resonances. *Nanoscale Research Letters* **1** (2006).

29. Keblinski, P., Cahill, D. G., Bodapati, A., Sullivan, C. R. & Taton, T. A. Limits of localized heating by electromagnetically excited nanoparticles. *Journal of Applied Physics* **100,** 054305 (2006).

30. Baffou, G., Cichos, F. & Quidant, R. Applications and challenges of thermoplasmonics. *Nature materials* **19,** 946–958 (2020).

31. Mukherjee, S. *et al.* Hot-electron-induced dissociation of H2 on gold nanoparticles supported on SiO2. *Journal of the American Chemical Society* **136,** 64–67 (2014).

32. Grzelczak, M. & Liz-Marzán, L. M. The relevance of light in the formation of colloidal metal nanoparticles. *Chem. Soc. Rev.* **43,** 2089–2097 (2014).

33. Turkevich, J. Colloidal gold. Part I. *Gold Bulletin* **18,** 86–91 (1985).

34. Turkevich, J., Stevenson, P. C. & Hillier, J. A study of the nucleation and growth processes in the synthesis of colloidal gold. *Discussions of the Faraday Society* **11,** 55 (1951).

35. Ojea-Jiménez, I., Bastús, N. G. & Puntes, V. Influence of the Sequence of the Reagents Addition in the Citrate-Mediated Synthesis of Gold Nanoparticles. *The Journal of Physical Chemistry C* **115,** 15752–15757 (2011).

36. Schulz, F. *et al.* Little adjustments significantly improve the Turkevich synthesis of gold nanoparticles. *Langmuir : the ACS journal of surfaces and colloids* **30,** 10779–10784 (2014).

37. Gao, Y. & Torrente-Murciano, L. Mechanistic insights of the reduction of gold salts in the Turkevich protocol. *Nanoscale* **12,** 2740–2751 (2020).

38. Sivaraman, S. K., Kumar, S. & Santhanam, V. Monodisperse sub-10 nm gold nanoparticles by reversing the order of addition in Turkevich method–the role of chloroauric acid. *Journal of Colloid and Interface Science* **361,** 543–547 (2011).

39. Ji, X. *et al.* Size control of gold nanocrystals in citrate reduction: the third role of citrate. *Journal of the American Chemical Society* **129,** 13939–13948 (2007).

40. Bastús, N. G., Comenge, J. & Puntes, V. Kinetically controlled seeded growth synthesis of citrate-stabilized gold nanoparticles of up to 200 nm. Size focusing versus Ostwald ripening. *Langmuir : the ACS journal of surfaces and colloids* **27,** 11098–11105 (2011).

41. Jana, N. R., Gearheart, L. & Murphy, C. J. Seed-Mediated Growth Approach for Shape-Controlled Synthesis of Spheroidal and Rod-like Gold Nanoparticles Using a Surfactant Template. *Advanced Materials* **13,** 1389–1393 (2001).

42. Nikoobakht, B. & El-Sayed, M. A. Preparation and Growth Mechanism of Gold Nanorods (NRs) Using Seed-Mediated Growth Method. *Chemistry of Materials* **15,** 1957–1962 (2003).

43. Mafuné, F. & Kondow, T. Formation of small gold clusters in solution by laser excitation of interband transition. *Chemical Physics Letters* **372,** 199–204 (2003).

44. Haiss, W., Thanh, N. T. K., Aveyard, J. & Fernig, D. G. Determination of size and concentration of gold nanoparticles from UV-vis spectra. *Analytical chemistry* **79,** 4215–4221 (2007).

45. Liu, M. & Guyot-Sionnest, P. Mechanism of silver(I)-assisted growth of gold nanorods and bipyramids. *The Journal of Physical Chemistry B* **109,** 22192–22200 (2005).

46. Scarabelli, L., Sánchez-Iglesias, A., Pérez-Juste, J. & Liz-Marzán, L. M. A "Tips and Tricks" Practical Guide to the Synthesis of Gold Nanorods. *The journal of physical chemistry letters* **6,** 4270–4279 (2015).

47. Almora-Barrios, N., Novell-Leruth, G., Whiting, P., Liz-Marzán, L. M. & López, N. Theoretical description of the role of halides, silver, and surfactants on the structure of gold nanorods. *Nano Letters* **14,** 871–875 (2014).

48. Imae, T., Kamiya, R. & Ikeda, S. Formation of spherical and rod-like micelles of cetyltrimethylammonium bromide in aqueous NaBr solutions. *Journal of Colloid and Interface Science* **108,** 215–225 (1985).

49. Whitesides, G. M. & Grzybowski, B. Self-assembly at all scales. *Science (New York, N.Y.)* **295,** 2418–2421 (2002).

50. Navarro, J. F., Frenk, C. S. & White, S. D. M. The assembly of galaxies in a hierarchically clustering universe. *Monthly Notices of the Royal Astronomical Society* **275,** 56–66 (1995).

51. Timsit, Y. DNA self-assembly: from chirality to evolution. *International Journal of Molecular Sciences* **14,** 8252–8270 (2013).

52. Saad, S. & Jarosz, D. F. Protein self-assembly: A new frontier in cell signaling. *Current Opinion in Cell Biology* **69,** 62–69 (2021).

53. Kapuscinski, M. *et al.* Temporal Evolution of Superlattice Contraction and Defect-Induced Strain Anisotropy in Mesocrystals during Nanocube Self-Assembly. *ACS nano* **14,** 5337–5347 (2020).

54. Connolly, S., Fullam, S., Korgel, B. & Fitzmaurice, D. Time-Resolved Small-Angle X-ray Scattering Studies of Nanocrystal Superlattice Self-Assembly. *Journal of the American Chemical Society* **120,** 2969–2970 (1998).

55. Huang, X. *et al.* Understanding Fe3O4 Nanocube Assembly with Reconstruction of a Consistent Superlattice Phase Diagram. *Journal of the American Chemical Society* **141,** 3198–3206 (2019).

56. Huang, X. *et al.* In Situ Constructing the Kinetic Roadmap of Octahedral Nanocrystal Assembly Toward Controlled Superlattice Fabrication. *Journal of the American Chemical Society* **143,** 4234–4243 (2021).

57. Grzelczak, M., Vermant, J., Furst, E. M. & Liz-Marzán, L. M. Directed self-assembly of nanoparticles. *ACS Nano* **4,** 3591–3605 (2010).

58. Grzelczak, M., Liz-Marzán, L. M. & Klajn, R. Stimuli-responsive self-assembly of nanoparticles. *Chemical Society Reviews.*

59. O'Brien, M. N., Brown, K. A. & Mirkin, C. A. Critical Undercooling in DNA-Mediated Nanoparticle Crystallization. *ACS nano* **10,** 1363–1368 (2016).

60. Iida, R., Mitomo, H., Niikura, K., Matsuo, Y. & Ijiro, K. Two-Step Assembly of Thermoresponsive Gold Nanorods Coated with a Single Kind of Ligand. *Small (Weinheim an der Bergstrasse, Germany)* **14,** e1704230 (2018).

61. Wu, L. *et al.* High-temperature crystallization of nanocrystals into three-dimensional superlattices. *Nature* **548,** 197–201 (2017).

62. Ding, T. *et al.* Light-induced actuating nanotransducers. *Proceedings of the National Academy of Sciences of the United States of America* **113,** 5503–5507 (2016).

63. Iida, R., Mitomo, H., Matsuo, Y., Niikura, K. & Ijiro, K. Thermoresponsive Assembly of Gold Nanoparticles Coated with Oligo(Ethylene Glycol) Ligands with an Alkyl Head. *The Journal of Physical Chemistry C* **120,** 15846–15854 (2016).

64. Bian, T., Chu, Z. & Klajn, R. The Many Ways to Assemble Nanoparticles Using Light. *Advanced materials (Deerfield Beach, Fla.),* e1905866 (2019).

65. Kundu, P. K., Das, S., Ahrens, J. & Klajn, R. Controlling the lifetimes of dynamic nanoparticle aggregates by spiropyran functionalization. *Nanoscale* **8,** 19280–19286 (2016).

66. Nabika, H., Oikawa, T., Iwasaki, K., Murakoshi, K. & Unoura, K. Dynamics of Gold Nanoparticle Assembly and Disassembly Induced by pH Oscillations. *The Journal of Physical Chemistry C* **116,** 6153–6158 (2012).

67. Deng, F., Feng, J. & Ding, T. Chemoplasmonic Oscillation: A Chemomechanical Energy Transducer. *ACS applied materials & interfaces* (2019).

68. Jeong, K.-J. *et al.* Helical Magnetic Field-Induced Real-Time Plasmonic Chirality Modulation. *ACS nano* **14,** 7152–7160 (2020).

69. Montelongo, Y. *et al.* Electrotunable nanoplasmonic liquid mirror. *Nature materials* **16,** 1127–1135 (2017).

70. Yu, Y., Yu, D., Sadigh, B. & Orme, C. A. Space- and time-resolved small angle X-ray scattering to probe assembly of silver nanocrystal superlattices. *Nature Communications* **9,** 4211 (2018).

71. Lehmkühler, F. *et al.* Kinetics of pressure-induced nanocrystal superlattice formation. *Physical chemistry chemical physics : PCCP* **21,** 21349–21354 (2019).

72. Schroer, M. A. *et al.* Supercrystal Formation of Gold Nanorods by High Pressure Stimulation. *The Journal of Physical Chemistry C* **123,** 29994–30000 (2019).

73. Ferrell, J. E. & Machleder, E. M. The biochemical basis of an all-or-none cell fate switch in Xenopus oocytes (1998).

74. Pomerening, J. R., Sontag, E. D. & Ferrell, J. E. Building a cell cycle oscillator: hysteresis and bistability in the activation of Cdc2. *Nature cell biology* **5,** 346–351 (2003).

75. Harfe, B. D. *et al.* Evidence for an expansion-based temporal Shh gradient in specifying vertebrate digit identities. *Cell* **118,** 517–528 (2004).

76. Das, J. *et al.* Digital signaling and hysteresis characterize ras activation in lymphoid cells. *Cell* **136,** 337–351 (2009).

77. Morris, K. A. What is Hysteresis? *Applied Mechanics Reviews* **64** (2011).

78. Grzybowski, B. A., Fitzner, K., Paczesny, J. & Granick, S. From dynamic self-assembly to networked chemical systems. *Chemical Society reviews* **46,** 5647–5678 (2017).

79. Deng, F., Wang, Y., Lu, X. & Ding, T. Probing hidden colloidal transitions with the assistance of surface plasmons. *Physical chemistry chemical physics : PCCP* **21,** 15742–15746 (2019).

80. Grötsch, R. K. *et al.* Pathway Dependence in the Fuel-Driven Dissipative Self-Assembly of Nanoparticles. *Journal of the American Chemical Society* **141,** 9872–9878 (2019).

81. Zhang, H., Zeng, H., Priimagi, A. & Ikkala, O. Programmable responsive hydrogels inspired by classical conditioning algorithm. *Nature Communications* **10,** 3267 (2019).

82. Wang, D., Kowalczyk, B., Lagzi, I. & Grzybowski, B. A. Bistability and Hysteresis During Aggregation of Charged Nanoparticles. *The Journal of Physical Chemistry Letters* **1,** 1459–1462 (2010).

83. Geyer, T., Born, P. & Kraus, T. Switching between crystallization and amorphous agglomeration of alkyl thiol-coated gold nanoparticles. *Physical Review Letters* **109,** 128302 (2012).

84. Born, P. & Kraus, T. Ligand-dominated temperature dependence of agglomeration kinetics and morphology in alkyl-thiol-coated gold nanoparticles. *Physical review. E, Statistical, nonlinear, and soft matter physics* **87,** 062313 (2013).

85. Tóth-Szeles, E. *et al.* Chemically coded time-programmed self-assembly. *Molecular Systems Design & Engineering* **2,** 274–282 (2017).

86. Guo, Y., Ma, Y., Xu, L., Li, J. & Yang, W. Conformational Change Induced Reversible Assembly/Disassembly of Poly- l -lysine-Functionalized Gold Nanoparticles. *Journal of Physical Chemistry C* **111,** 9172–9176 (2007).

87. Liu, F. & Agarwal, S. Thermoresponsive Gold Nanoparticles with Positive UCST-Type Thermoresponsivity. *Macromolecular Chemistry and Physics* **216,** 460–465 (2015).

88. Ye, J., Hou, Y., Zhang, G. & Wu, C. Temperature-induced aggregation of poly(N-isopropylacrylamide)-stabilized CdS quantum dots in water. *Langmuir : the ACS journal of surfaces and colloids* **24,** 2727–2731 (2008).

89. Bhattacharjee, R. R., Chakraborty, M. & Mandal, T. K. Reversible association of thermoresponsive gold nanoparticles: polyelectrolyte effect on the lower critical solution temperature of poly(vinyl methyl ether). *The Journal of Physical Chemistry B* **110,** 6768–6775 (2006).

90. Kim, D. J. *et al.* Formation of Thermoresponsive Gold Nanoparticle/PNIPAAm Hybrids by Surface-Initiated, Atom Transfer Radical Polymerization in Aqueous Media. *Macromolecular Chemistry and Physics* **206,** 1941–1946 (2005).

91. Li, C. *et al.* Synthesis of thiol-terminated thermoresponsive polymers and their enhancement effect on optical limiting property of gold nanoparticles. *European Polymer Journal* (2019).

92. Liu, X.-Y. *et al.* Thermoresponsive gold nanoparticles with adjustable lower critical solution temperature as colorimetric sensors for temperature, pH and salt concentration. *J. Mater. Chem.* **20,** 278–284 (2010).

93. Hill, A. P., Kunstmann-Olsen, C., Grzelczak, M. P. & Brust, M. Entropy-Driven Reversible Agglomeration of Crown Ether Capped Gold Nanoparticles. *Chemistry (Weinheim an der Bergstrasse, Germany)* **24,** 3151–3155 (2018).

94. Bishop, K. J. M., Kowalczyk, B. & Grzybowski, B. A. Precipitation of oppositely charged nanoparticles by dilution and/or temperature increase. *The Journal of Physical Chemistry B* **113,** 1413–1417 (2009).

95. Gan, J., Mei, Z., Chen, X., Zhou, Y. & Ge, M.-F. A Modified Duhem Model for Rate-Dependent Hysteresis Behaviors. *Micromachines* **10** (2019).

96. He, X. *et al.* Synthetic homeostatic materials with chemo-mechano-chemical self-regulation. *Nature* **487,** 214–218 (2012).

97. Semenov, S. N. *et al.* Autocatalytic, bistable, oscillatory networks of biologically relevant organic reactions. *Nature* **537,** 656–660 (2016).

98. Klajn, R., Wesson, P. J., Bishop, K. J. M. & Grzybowski, B. A. Writing self-erasing images using metastable nanoparticle "inks". *Angewandte Chemie (International ed. in English)* **48,** 7035–7039 (2009).

99. Liu, Y., Han, X., Le He & Yin, Y. Thermoresponsive assembly of charged gold nanoparticles and their reversible tuning of plasmon coupling. *Angewandte Chemie (International ed. in English)* **51,** 6373–6377 (2012).

100. Aymard, P. *et al.* Influence of thermal history on the structural and mechanical properties of agarose gels. *Biopolymers* **59,** 131–144 (2001).

101. Narayanan, J., Xiong, J.-Y. & Liu, X.-Y. Determination of agarose gel pore size: Absorbance measurements vis a vis other techniques. en. *Journal of Physics: Conference Series* **28,** 83 (2006).

102. Jones, S. T. *et al.* The Importance of Excess Poly(N-isopropylacrylamide) for the Aggregation of Poly(N-isopropylacrylamide)-Coated Gold Nanoparticles. *ACS Nano* **10,** 3158–3165 (2016).

103. Israelachvili, J. N. *Intermolecular and Surface Forces* 3rd (Academic Press, Nov. 2010).

104. Zámbó, D., Radnóczi, G. Z. & Deák, A. Preparation of compact nanoparticle clusters from polyethylene glycol-coated gold nanoparticles by fine-tuning colloidal interactions. *Langmuir : the ACS journal of surfaces and colloids* **31,** 2662–2668 (2015).

105. Nikoobakht, B. & El-Sayed, M. A. Evidence for Bilayer Assembly of Cationic Surfactants on the Surface of Gold Nanorods. *Langmuir : the ACS journal of surfaces and colloids* **17,** 6368–6374 (2001).

106. Gómez-Graña, S. *et al.* Surfactant (bi)layers on gold nanorods. *Langmuir : the ACS journal of surfaces and colloids* **28,** 1453–1459 (2012).

107. Dewi, M. R., Laufersky, G. & Nann, T. A highly efficient ligand exchange reaction on gold nanoparticles: preserving their size, shape and colloidal stability. *RSC Adv* **4,** 34217–34220 (2014).

108. García, I. *et al.* Residual CTAB Ligands as Mass Spectrometry Labels to Monitor Cellular Uptake of Au Nanorods. *The Journal of Physical Chemistry Letters* **6,** 2003–2008 (2015).

109. Zhou, S. *et al.* Enabling Complete Ligand Exchange on the Surface of Gold Nanocrystals through the Deposition and Then Etching of Silver. *Journal of the American Chemical Society* **140,** 11898–11901 (2018).

110. Piella, J., Bastús, N. G. & Puntes, V. Size-Controlled Synthesis of Sub-10-nanometer Citrate-Stabilized Gold Nanoparticles and Related Optical Properties. *Chemistry of Materials* **28,** 1066–1075 (2016).

111. Yoon, S., Kim, C., Lee, B. & Lee, J. H. From a precursor to an etchant: spontaneous inversion of the role of Au(iii) chloride for one-pot synthesis of smooth and spherical gold nanoparticles. *Nanoscale Advances* **1,** 2157–2161 (2019).

112. Karg, M., Pastoriza-Santos, I., Pérez-Juste, J., Hellweg, T. & Liz-Marzán, L. M. Nanorod-coated PNIPAM microgels: thermoresponsive optical properties. *Small* **3,** 1222–1229 (2007).

113. Schweizerhof, S., Demco, D. E., Mourran, A., Fechete, R. & Möller, M. Diffusion of Gold Nanorods Functionalized with Thermoresponsive Polymer Brushes. *Langmuir : the ACS journal of surfaces and colloids* **34,** 8031–8041 (2018).

114. Grzelak, D. *et al.* In situ tracking of colloidally stable and ordered assemblies of gold nanorods. *Journal of the American Chemical Society* (2020).

115. Kim, H. J., Wang, W., Travesset, A., Mallapragada, S. K. & Vaknin, D. Temperature-Induced Tunable Assembly of Columnar Phases of Nanorods. *ACS nano* **14,** 6007–6012 (2020).

116. Dujardin, E., Mann, S., Hsin, L.-B. & Wang, C. R. C. DNA-driven self-assembly of gold nanorods. *Chemical Communications,* 1264–1265 (2001).

117. Mba, J. C. *et al.* Hysteresis in the Thermo-Responsive Assembly of Hexa(ethylene glycol) Derivative-Modified Gold Nanodiscs as an Effect of Shape. *Nanomaterials (Basel, Switzerland)* **12,** 1421 (2022).

118. Ford, M. J., Masens, C. & Cortie, M. B. The Application of Gold Surfaces in Nanotechnology. *Surface Review and Letters* **13,** 297–307 (2006).

119. Liu, K. *et al.* Biocompatible gold nanorods: one-step surface functionalization, highly colloidal stability, and low cytotoxicity. *Langmuir : the ACS journal of surfaces and colloids* **31,** 4973–4980 (2015).

120. Chang, H.-H. & Murphy, C. J. Mini Gold Nanorods with Tunable Plasmonic Peaks beyond 1000 nm. *Chemistry of Materials* **30,** 1427–1435 (2018).

121. Kinnear, C. *et al.* Gold nanorods: controlling their surface chemistry and complete detoxification by a two-step place exchange. *Angewandte Chemie (International ed. in English)* **52,** 1934–1938 (2013).

122. Goronja, J. *et al.* Determination of critical micelle concentration of cetyltrimethylammonium bromide: Different procedures for analysis of experimental data. *Hemijska industrija* **70,** 485–492 (2016).

123. Yu, Y. *et al.* Nanocrystal superlattices that exhibit improved order on heating: an example of inverse melting? *Faraday Discussions* **181,** 181–192 (2015).

124. Liu, H., Pierre-Pierre, N. & Huo, Q. Dynamic light scattering for gold nanorod size characterization and study of nanorod–protein interactions. *Gold Bulletin* **45,** 187–195 (2012).

125. Yon, M., Pibourret, C., Marty, J.-D. & Ciuculescu-Pradines, D. Easy colorimetric detection of gadolinium ions based on gold nanoparticles: key role of phosphine-sulfonate ligands. *Nanoscale Advances* **2,** 4671–4681 (2020).

126. Mehtala, J. G. *et al.* Citrate-stabilized gold nanorods. *Langmuir : the ACS journal of surfaces and colloids* **30,** 13727–13730 (2014).

127. Kawano, T., Niidome, Y., Mori, T., Katayama, Y. & Niidome, T. PNIPAM gel-coated gold nanorods for targeted delivery responding to a near-infrared laser. *Bioconjugate Chemistry* **20,** 209–212 (2009).

128. Guerrero, A. R. *et al.* Gold nanoparticles for photothermally controlled drug release. *Nanomedicine (London, England)* **9,** 2023–2039 (2014).

129. Liu, J. *et al.* Gold nanorods coated with a thermo-responsive poly(ethylene glycol)-b-poly(N-vinylcaprolactam) corona as drug delivery systems for remotely near infrared-triggered release. *Polymer Chemistry* **5,** 799–813 (2014).

130. Pissuwan, D., Valenzuela, S. M., Killingsworth, M. C., Xu, X. & Cortie, M. B. Targeted destruction of murine macrophage cells with bioconjugated gold nanorods. *Journal of Nanoparticle Research* **9,** 1109–1124 (2007).

131. Hleb, E. Y. *et al.* LANTCET: elimination of solid tumor cells with photothermal bubbles generated around clusters of gold nanoparticles. *Nanomedicine (London, England)* **3,** 647–667 (2008).

132. Gong, B. *et al.* Thermo-responsive polymer encapsulated gold nanorods for single continuous wave laser-induced photodynamic/photothermal tumour therapy. *Journal of Nanobiotechnology* **19,** 41 (2021).

133. Parreira, R., Özelçi, E. & Sakar, M. S. Remotely Controlled Colloidal Assembly of Soft Microrobotic Artificial Muscle. *Advanced Intelligent Systems* **2,** 2000062 (2020).

134. Mishra, S. R. & Tracy, J. B. Sequential Actuation of Shape-Memory Polymers through Wavelength-Selective Photothermal Heating of Gold Nanospheres and Nanorods. *ACS Applied Nano Materials* **1,** 3063–3067 (2018).

135. Pierini, F. *et al.* Thermoplasmonic–Activated Hydrogel Based Dynamic Light Attenuator. *Advanced Optical Materials* **8,** 2000324 (2020).

136. Cao, D., Xu, C., Lu, W., Qin, C. & Cheng, S. Sunlight-Driven Photo-Thermochromic Smart Windows. *Solar RRL* **2,** 1700219 (2018).

137. Cormier, S., Ding, T., Turek, V. & Baumberg, J. J. Actuating Single Nano-Oscillators with Light. *Advanced Optical Materials* **6,** 1701281 (2018).

138. Wang, C. *et al.* DNA-Based Hydrogels Loaded with Au Nanoparticles or Au Nanorods: Thermoresponsive Plasmonic Matrices for Shape-Memory, Self-Healing, Controlled Release and Mechanical Applications. *ACS Nano* (2019).

139. Zeng, H. *et al.* Light-fuelled freestyle self-oscillators. *Nature Communications* **10,** 5057 (2019).

140. Yang, L. *et al.* An Autonomous Soft Actuator with Light–Driven Self–Sustained Wavelike Oscillation for Phototactic Self–Locomotion and Power Generation. *Advanced Functional Materials* **30,** 1908842 (2020).

141. Jenkins, A. Self-oscillation. *Physics Reports* **525,** 167–222 (2013).

142. Bill Unruh. *Negative Resistance* Dec. 4, 2002.

143. Jain, P. K. Taking the Heat Off of Plasmonic Chemistry. *The Journal of Physical Chemistry C* **123,** 24347–24351 (2019).

144. Das, K., Gabrielli, L. & Prins, L. J. Chemically Fueled Self-Assembly in Biology and Chemistry. *Angewandte Chemie (International ed. in English)* **60,** 20120–20143 (2021).

145. Heuser, T., Steppert, A.-K., Lopez, C. M., Zhu, B. & Walther, A. Generic concept to program the time domain of self-assemblies with a self-regulation mechanism. *Nano Letters* **15,** 2213–2219 (2015).

146. Maiti, S., Fortunati, I., Ferrante, C., Scrimin, P. & Prins, L. J. Dissipative self-assembly of vesicular nanoreactors. *Nature Chemistry* **8,** 725–731 (2016).

147. Boekhoven, J., Hendriksen, W. E., Koper, G. J. M., Eelkema, R. & van Esch, J. H. Transient assembly of active materials fueled by a chemical reaction. *Science* **349,** 1075–1079 (2015).

148. Luo, M. *et al.* Four–Dimensional Deoxyribonucleic Acid–Gold Nanoparticle Assemblies. *Angewandte Chemie* **132,** 17403–17408 (2020).

149. Bian, T. *et al.* Electrostatic co-assembly of nanoparticles with oppositely charged small molecules into static and dynamic superstructures. *Nature Chemistry* **13,** 940–949 (2021).

150. Chen, J. L.-Y., Maiti, S., Fortunati, I., Ferrante, C. & Prins, L. J. Temporal Control over Transient Chemical Systems using Structurally Diverse Chemical Fuels. *Chemistry – A European Journal* **23,** 11549–11559 (2017).

151. Del Grosso, E., Amodio, A., Ragazzon, G., Prins, L. J. & Ricci, F. Dissipative Synthetic DNA-Based Receptors for the Transient Loading and Release of Molecular Cargo. *Angewandte Chemie (International ed. in English)* **57,** 10489–10493 (2018).

152. Boekhoven, J. *et al.* Dissipative self-assembly of a molecular gelator by using a chemical fuel. *Angewandte Chemie (International ed. in English)* **49,** 4825–4828 (2010).

153. Chevigny, R. *et al.* Triggering a transient organo-gelation system in a chemically active solvent. *Chemical Communications* **57,** 10375–10378 (2021).

154. Würbser, M. A. *et al.* Chemically Fueled Block Copolymer Self–Assembly into Transient Nanoreactors**. *ChemSystemsChem* **3** (2021).

155. Deng, J., Liu, W., Sun, M. & Walther, A. Dissipative Organization of DNA Oligomers for Transient Catalytic Function. *Angewandte Chemie* **134** (2022).

156. Sawczyk, M. & Klajn, R. Out-of-Equilibrium Aggregates and Coatings during Seeded Growth of Metallic Nanoparticles. *Journal of the American Chemical Society* **139,** 17973–17978 (2017).

157. Ouyang, Y., Zhang, P., Manis-Levy, H., Paltiel, Y. & Willner, I. Transient Dissipative Optical Properties of Aggregated Au Nanoparticles, CdSe/ZnS Quantum Dots, and Supramolecular Nucleic Acid-Stabilized Ag Nanoclusters. *Journal of the American Chemical Society* **143,** 17622–17632 (2021).

158. Della Sala, F., Maiti, S., Bonanni, A., Scrimin, P. & Prins, L. J. Fuel-Selective Transient Activation of Nanosystems for Signal Generation. *Angewandte Chemie (International ed. in English)* **57,** 1611–1615 (2018).

159. Deng, J. & Walther, A. ATP-powered molecular recognition to engineer transient multivalency and self-sorting 4D hierarchical systems. *Nature Communications* **11,** 3658 (2020).

160. Wang, G. & Liu, S. Strategies to Construct a Chemical–Fuel–Driven Self–Assembly. *ChemSystemsChem* **2** (2020).

161. Sato, K., Hosokawa, K. & Maeda, M. Rapid aggregation of gold nanoparticles induced by non-cross-linking DNA hybridization. *Journal of the American Chemical Society* **125,** 8102–8103 (2003).

162. Muradyan, H. & Guan, Z. Chemothermally Driven Out–of–Equilibrium Materials for Macroscopic Motion. *ChemSystemsChem* **2** (2020).

163. Jones, G. O. & Houk, K. N. Predictions of substituent effects in thermal azide 1,3-dipolar cycloadditions: implications for dynamic combinatorial (reversible) and click (irreversible) chemistry. *Journal of Organic Chemistry* **73,** 1333–1342 (2008).

164. Hurst, S. J., Lytton-Jean, A. K. R. & Mirkin, C. A. Maximizing DNA loading on a range of gold nanoparticle sizes. *Analytical chemistry* **78,** 8313–8318 (2006).

165. Bock, V. D., Hiemstra, H. & van Maarseveen, J. H. Cu I –Catalyzed Alkyne–Azide "Click" Cycloadditions from a Mechanistic and Synthetic Perspective. *European Journal of Organic Chemistry* **2006,** 51–68 (2006).

166. Brotherton, W. S. *et al.* Apparent copper(II)-accelerated azide-alkyne cycloaddition. *Organic Letters* **11,** 4954–4957 (2009).

167. Wang, G. *et al.* Cross-Linking versus Non-Cross-Linking Aggregation of Gold Nanoparticles Induced by DNA Hybridization: A Comparison of the Rapidity of Solution Color Change. *Bioconjugate Chemistry* **28,** 270–277 (2017).

168. Blackburn, G. M. *Nucleic acids in chemistry and biology* 3rd ed. / edited by G. Michael Blackburn ... [et al.] (RSC Pub, Cambridge, 2006).

169. Alonso, F., Moglie, Y. & Radivoy, G. Copper Nanoparticles in Click Chemistry. *Accounts of Chemical Research* **48,** 2516–2528 (2015).

170. Choi, J. *et al.* Telodendrimers for Physical Encapsulation and Covalent Linking of Individual or Combined Therapeutics. *Molecular Pharmaceutics* **14,** 2607–2615 (2017).